Functional Investigations of *Capicua* (*CIC*) and *ATAXIN-1-Like* (*ATXN1L*) in cancer.

by

Derek Wong

A THESIS SUBMITTED IN PARTIAL FULFILLMENT OF

THE REQUIREMENTS FOR THE DEGREE OF

DOCTOR OF PHILOSPHY

in

THE FACULTY OF GRADUATE AND POSTDOCTORAL STUDIES

(Pathology and Laboratory Medicine)

THE UNIVERSITY OF BRITISH COLUMBIA

(Vancouver)

December 2020

The following individuals certify that they have read, and recommend to the Faculty of Graduate and Postdoctoral Studies for acceptance, the dissertation entitled:

Functional Investigations of Capicua (CIC) and ATAXIN-1-Like (ATXN1L) in cancer.

submitted by Derek Wong in partial fulfillment of the requirements for the degree of Doctor of Philosophy in Pathology and Laboratory Medicine

Examining Committee:

Dr. Stephen Yip MD, PhD, FRCPC, Pathology and Laboratory Medicine
Supervisor

Dr. David Huntsman, MD, FRCPC, FCCMG, Pathology and Laboratory Medicine
Co-supervisor

Dr. Poul Sorensen, MD, PhD,FRCPC, Pathology and Laboratory Medicine
University Examiner

Dr. Amina Zoubeidi, PhD, Urologic Sciences
University Examiner

Additional Supervisory Committee Members:

Dr. Marcel Bally, PhD, Experimental Therapeutics
Supervisory Committee Member

Dr. Marco Marra, PhD, FRS(C), FCAHS, OBC, Medical Genetics
Supervisory Committee Member

Abstract

Mutations in the *Capicua* (*CIC*) gene, located on chromosome 19q, were first identified in up to 70% of 1p19q-codeleted, IDH-mutated Oligodendrogliomas (ODGs), a subtype of diffuse low grade glioma (DLGG). Since then, several studies have highlighted that loss or dysregulation of CIC is associated with tumour progression, worse prognosis, and treatment resistance in multiple cancer types. One CIC binding partner, Ataxin-1-Like (ATXN1L), has been implicated as an important regulator of CIC function in murine development, but little is known in the context of cancer. In this thesis, we characterize the functional interaction between CIC and ATXN1L and their relationship in regulating pathways involved in tumourigenesis.

The function of ATXN1L in relation to CIC was investigated by assessing and comparing the transcriptomic consequences of *ATXN1L* knockout (KO) and *CIC* KO using isogenic cell lines. Loss of either CIC or ATXN1L led to concordant dysregulation of gene sets in each context which converged upon several pathways involved in differentiation and activation of the mitogen activated protein kinase (MAPK) pathway as a result of decreased CIC-DNA binding. Further analysis of cancers harboring deletions in *CIC* and *ATXN1L*, namely, stomach adenocarcinoma, prostate adenocarcinoma, and astrocytoma, resulted in convergent dysregulation of several pathways involved in cell proliferation and growth.

In addition to decreased CIC-DNA binding, loss of ATXN1L resulted in increased CIC protein instability as a result of proteasomal degradation which was found to be independent of ERK activity, the canonical CIC degradation pathway. Instead, loss of ATXN1L was found to promote CIC instability through ubiquitination by the E3-ligase TRIM25, a novel CIC interactor. Transcriptomic analyses of breast carcinomas with *TRIM25* amplification and liver hepatocellular carcinomas with high *TRIM25* expression revealed dysregulation of genes and pathways reminiscent of *CIC* loss, supporting its role in the post-translational regulation of CIC.

The results of these studies illuminate our understanding and the intricacy of mechanisms which regulate normal CIC function in cancer; and further supports the role of CIC as a potent tumour suppressor in a multitude of cancer types.

Lay Summary

Brain tumours are generally associated with poor outcomes due to the difficulty in surgical resection and their close proximity to important cognitive structures. Research in the past decade has uncovered several mutations associated with specific subtypes of brain tumours that can be used to predict their clinical outcomes. However, much research is still needed to understand the biology of each mutation. Oligodendrogliomas are a type of brain tumour associated with mutations in *Capicua* (CIC), a gene involved in development. In this thesis, we explore how normal CIC function is regulated by ATXN1L and ways in which cancers can modulate their function in order to promote aggressive behaviors. By understanding the regulators and function of CIC, future research can investigate methods to modulate CIC function to better treat a plethora of tumours which rely on diminished CIC function for metastasis, progression, and treatment resistance.

Preface

This dissertation is original and independent work by the author Derek Wong. The research in this thesis was conducted with ethics approval from the UBC – BC Cancer Research Ethics Board, Certificate Number: H08-02838.

Portions of Chapter 1 have been published as:

- **Derek Wong,** Stephen Yip (2019) Chapter 6 - Pathology of Primary Brain Tumors – Gliomas. In Kaisorn Chaichana and Alfredo Quiñones-Hinojosa, Comprehensive Overview of Modern Surgical Approaches to Intrinsic Brain Tumors. Pages 121-137
- **Derek Wong**, Stephen Yip (2020) Making heads or tails – The emergence of *Capicua* in cancer. *Journal of Pathology.* 250(5):532-540.

I am the first author of these two manuscripts. I wrote and performed the majority of literature research for these manuscripts.

Portions of Chapter 3 and 4 have been published as:

- **Derek Wong**, Kohl Lounsbury, Amy Lum, Jungeun Song, Susanna Chan, Veronique LeBlanc, Suganthi Chittaranjan, Marco Marra, Stephen Yip (2018) Transcriptomic analysis of CIC and ATXN1L reveal a functional relationship exploited by cancer. *Oncogene.* 38(2):273-290.

I am the first author of this manuscript. I wrote, designed and performed the majority of experiments and analyses for this manuscript.

Portions of Chapter 4 have been submitted as:

- **Derek Wong**, Samantha S Lee, Lisa Sogerer, Victor Wong, Amy Lum, Adrian B. Levine, Marco A Marra, Stephen Yip (2020) Loss of ATXN1L promotes ERK independent proteasomal degradation of Capicua through TRIM25 in cancer. *BMC Biology.* 18(154).

I am the first author of this manuscript. I wrote, designed and performed the majority of experiments and analyses for this manuscript.

Table of Contents

List of Tables

List of Figures

List of Abbreviations

5mC	5-methylcytosine
αKG	α-ketoglutarate
2HG	2-Hydroxyglutarate
ABD	Ataxin Binding Domain
ATXN1L	Ataxin-1-Like
ATXN1	Ataxin1
AXH	Ataxin-1 and HMG-box Protein 1
BCCA	British Columbia Cancer Agency
BCCRC	British Columbia Cancer Research Center
BCGSC	British Columbia Genome Sciences Center
BRCA	Breast Carcinoma
ChIP	Chromatin Immunoprecipitation
CIC	Capicua
CNV	Copy Number Variation
CRISPR	Clustered Regularly Interspaced Short Palindromic Repeats
DE	Differentially Expressed
DEA	Differential Expression Analysis
DNA	Deoxyribonucleic Acid
E2F	E2 Transcription Factor
EBD	ERK Binding Domain
ETS	E-Twenty-Six Transcription Factor
FFPE	Formalin Fixed Paraffin Embedded
GBM	Glioblastoma
GEO	Gene Expression Omnibus
GO	Gene Ontology
GSEA	Gene Set Enrichment Analysis
HEK	Human Embryonic Kidney
HMG	High Mobility Group
HOG	Human Oligodendroglial
IDH	Isocitrate Dehydrogenase

IHC	Immunohistochemistry
IP	Immunoprecipitation
LGG	Low Grade Glioma
LIHC	Liver Hepatocellular Carcinoma
MAPK	Mitogen Activated Protein Kinase
mTOR	Mammalian Target of Rapamycin
NHA	Normal Human Astrocyte
ODG	Oligodendroglioma
PBS	Phosphate Buffered Saline
PRAD	Prostate Adenocarcinoma
PTM	Post Translational Modification
Rb	Retinoblastoma Transcriptional Corepressor
RNA	Ribonucleic Acid
RTK	Receptor Tyrosine Kinase
RT-qPCR	Real-Time Quantitative Polymerase Chain Reaction
SCA1	Spinocerebellar Ataxia 1
SD	Standard Deviation
STAD	Stomach Adenocarcinoma
TBS	Tris Buffered Saline
TCGA	The Cancer Genome Atlas
WHO	World Health Organization

Acknowledgements

The completion of this dissertation was achieved through the support and help of a number of people. I would like to thank my supervisor Dr. Stephen Yip who gave me guidance but also the freedom to explore scientifically, my doctoral supervisory committee (Dr. Marco Marra, Dr. David Huntsman, Dr. Marcel Bally, Dr. William Lockwood) for providing their valuable time and advice, and past and present members of the Stephen Yip lab (Amy Lum, Adrian Levine, Tae Hoon Lee, Kohl Lounsbury, Samantha Lee, Lisa Sogerer, and Victor Wong) and Marco Marra lab (Veronique LeBlanc, and Suganthi Chittaranjan) who contributed technically and scientifically to varying degrees.

I would also like to thank members of Dr Gregory Cairncross, Dr Jennifer Chan, Dr Kenneth Aldape, and Dr. David Huntsman laboratories for helpful discussions and advice.

I am thankful to my friends, family, and my partner Philip for their support throughout my studies.

Finally, I would like to acknowledge all the patients who donated samples and that make this research possible.

The research presented in this thesis was funded by the Canadian Cancer Society and the BC Cancer Foundation through BrainCare BC.

Chapter 1: Introductions

1.1 Low Grade Gliomas

1.1.1 Etiology and Epidemiology

Primary brain tumors, by strict definition, arise from the intrinsic non-neoplastic cellular elements of the brain. As postulated initially by Harvey Cushing and Percival Bailey in the 1920s - the normal endogenous cellular constituents of the brain have neoplastic counterparts [1]. This formed the intellectual construct for brain tumor ontogeny which has also influenced the nomenclature of the tumors today. Diffuse and infiltrative growth is a cardinal feature of the vast majority of glioma, especially those with World Health Organization (WHO) grades of II to IV classification. Infiltrating glioma (WHO II-IV), as the name suggests, displays distant spread along vasculature and white matter tracts which contribute to recurrence locally and in distal sites. Scherer first described these histological features in the 1930s, now known as Scherer's secondary structures [2], which are some of the defining histological features of infiltrating glioma.

Low grade gliomas (LGGs) encompass grade II and III tumours with an incidence rate of roughly 1.43/100,000 people [3], are less common than glioblastoma (GBM), the grade IV counterpart. Compared to GBM, LGGs grow slowly and are generally associated with a favorable outcome. However, many LGGs inevitably progress through malignant transformation towards GBM. Although many advances in understanding the molecular landscape of gliomas, in particular LGGs, have been made in the past three decades, the treatment options and survival for these tumours have stagnated. Despite having a generally high 5 year survival rate of between 32-81% (depending on subtype), compared to GBM (8%), LGG patients are often diagnosed at a much younger age (mean = 41 years), compared to GBM patients (mean = 66 years) [3] resulting in a greater loss of productive life in these individuals.

1.1.2 Molecular Alterations and Histopathology

The diagnostic algorithm for LGG in the post WHO 2016 Classification era is much more reliant on the molecular information of *IDH1/2*, *ATRX*, and copy number status of chromosomes 1p/19q and represents a marked departure from the 2007 histology based classification. LGGs

can be separated into three major molecular subtypes which provide superior prognostic information compared to traditional histological classification (Table 1.1) [4-6].

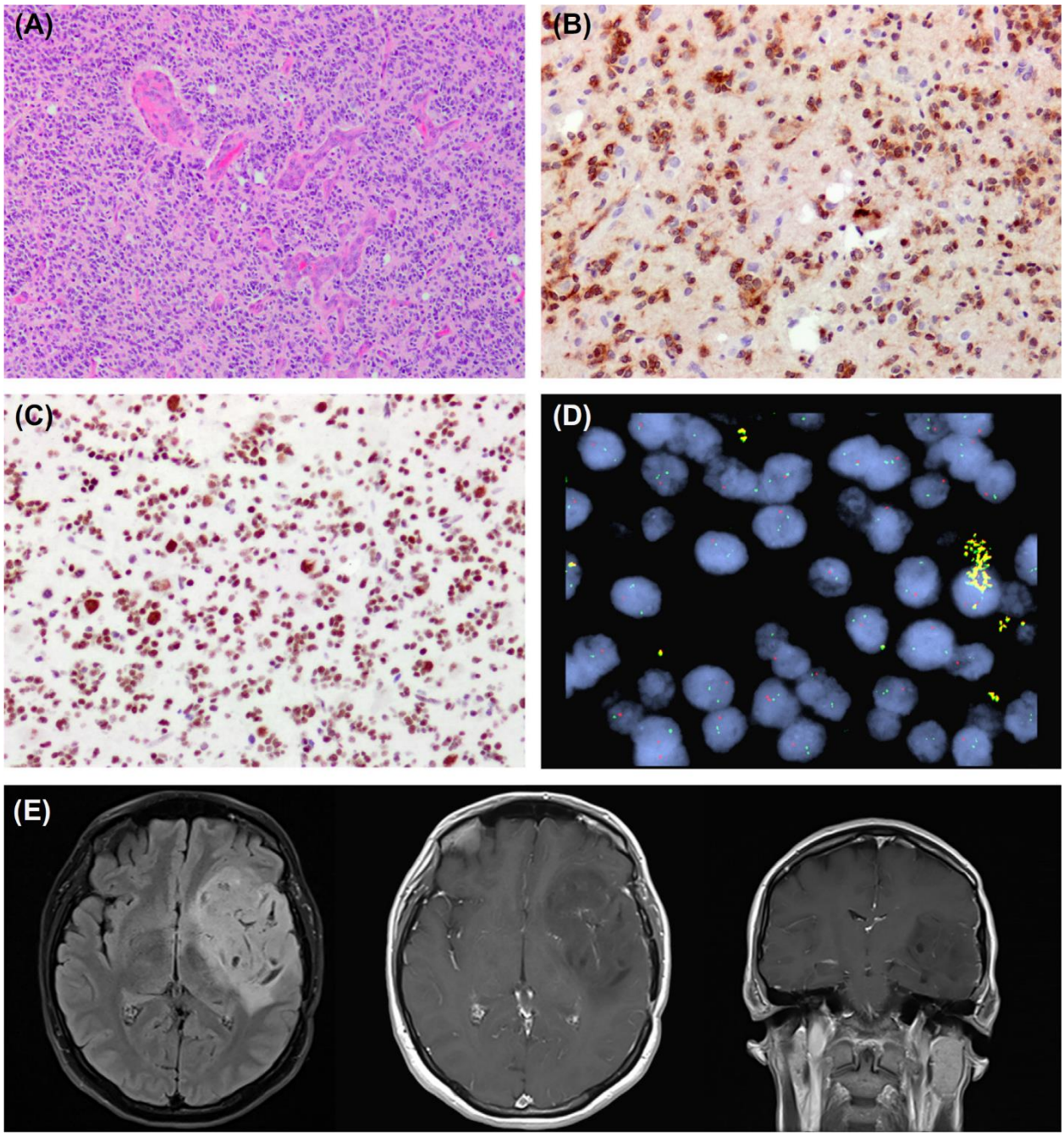

Figure 1.1 – Clinical Presentation of Oligodendroglioma
Anaplastic oligodendroglioma with foci of microvascular proliferation is characterized by tumor cells with round to ovoid nuclei associated with nil to small amount of cytoplasm and perinuclear clearing (A). The tumor cells strongly express the IDH1 R132H mutant protein (B) but retain nuclear expression of ATRX(C). This is confirmed by 1p19q FISH showing co-deletion (D, only 1p FISH shown). (E) MRI imaging of anaplastic oligodendroglioma, IDH mutant, 1p19q co-deleted (WHO III). (Left) Circumscribed T2 FLAIR signal abnormality within the left frontal lobe on the axial plane is indicative of a solid/cystic intra-axial tumor. (Middle) The tumor shows scant intra-lesional contrast enhancement on T1, especially in the anterior aspect on axial plane. (Right) However, the vast majority of the tumor is non-enhancing on coronal plane.

Table 1.1 – Molecular Subtypes of LGG

Type	Histology	IDH Status	1p19q Status
Type I	Oligodendroglioma	Mutated	Co-deleted
Type II	Astrocytoma	Mutated	Retained
Type III	IDH Wildtype Astrocytoma	Wildtype	Retained

In addition to providing superior prognostic data, each molecular subtype can also be generally associated with a histologically defined entity. Type I LGG which harbour concurrent losses of the entire short arm of chromosome 1 (1p) and long arm of chromosome 19 (19q) [1p19q co-deletion], is most often associated with oligodendroglial histology [7, 8]. Virtually all 1p19q co-deleted tumours harbor IDH mutations. The arm-wise losses are the result of unbalanced translocation events and are generally accompanied by a relatively quiet genome [9, 10]. The histological features frequently described in ODG include perinuclear clearing in FFPE tissues and are known to have a "fried-egg" appearance. It is likely the result of "washing out" of cytoplasmic glycogen by organic solvent during tissue processing and is not evident in tissue frozen sections (Figure 1.1). Moreover, tumor cells from ODG tend to display round, regular nuclear features with very little morphological pleomorphism and no associated cytoplasmic content. This is reminiscent of non-neoplastic oligodendrocytes. The presence of delicate branching blood vessels, known colloquially as "chicken-wire" appearance, is also associated with low-grade ODG. These vessels can undergo proliferation in anaplastic ODG, and predominance of this histological finding is one of the diagnostic criteria for WHO III tumor.

Conversely, Type II LGGs are most often associated with Astrocytomas and have a high frequency of *ATRX* immunonegativity by immunohistochemical staining (IHC) as a result of *ATRX* loss of function genomic aberrations. Astrocytoma cells frequently display elongated, hyperchromatic nuclei in association with variable amount of eosinophilic cytoplasm reminiscent of non-neoplastic astrocytes. Astrocytic tumors can display cytological features of astrocytoma, oligodendroglioma, or a combination of the two. However, absence of 1p19q co-deletion itself remains the most important molecular identifier of astrocytomas.

Lastly, Type III tumours are a small percentage of LGGs which do not exhibit IDH mutations or 1p19q co-deletion. These tumours, referred to as "triple negative tumours", carry the worst prognosis and are associated with genomic aberrations reminiscent of GBM such as homozygous loss of *CDKN2A/B* and *PTEN* as well as *EGFR* amplification [11].

1.2 IDH Mutations

There have been many important discoveries on the molecular pathogenesis of infiltrating glioma in the past 10 years. However, the identification and characterization of recurrent mutations in the genes *IDH1/2* remain the most significant with impact on all spheres in the clinical management of patients with infiltrating gliomas. Initially identified in young GBM patients, it was later verified to be arising from preceding LGGs [12]. Follow-up studies confirmed that recurrent heterozygous IDH mutations occur early during gliomagenesis and are found in a large percentage of LGG [11]. A vast majority of IDH mutations occur in codon 132 of *IDH1*, which leads to arginine to histidine amino acid change (IDH1 p.R132H) that accounts for >83% of all mutations in LGG. A minority of *IDH1* mutations in codon 132 lead to other amino acid changes. Mutations affecting codon 172 of *IDH2* are only found in approximately 5% of gliomas with IDH mutations. All IDH mutations result in the aberrant overproduction of the oncometabolite 2-hydroxyglutarate (2HG), which is normally produced in very small amounts in extreme physiological conditions and has profound effects on the epigenome of the cancer cell [13]. Specifically, 2-HG inhibits α-ketoglutarate (αKG)-dependent dioxygenases including TET2 and also lowers the levels of 5-hydroxymethylcytosine (5mC), which lead to alterations of genome-wide histone and DNA methylation [14-16]. Together, these changes have significant impact on the cancer epigenome [17, 18]. 2HG also affects other cellular pathways, including those that regulate the normal physiological degradation of hypoxia inducible factor-1 (HIF1a) [19]. Taken together, overexpression of 2HG as a result of IDH mutations is essential for gliomagenesis.

1.3 Capicua (CIC)

1.3.1 *CIC* Aberrations in Cancer

Capicua (*CIC*), a gene located on human chromosome 19q13.3, encodes for an evolutionarily conserved member of the High Mobility Group (HMG) box protein superfamily involved in DNA binding. CIC was first identified as a transcriptional repressor, with two isoforms (CIC-S and CIC-L), responsible for regulating growth and proliferation of specific tissues during the development of *Drosophila melanogaster* [20-25]. In general, CIC acts as a repressor of receptor tyrosine kinase (RTK) responsive genes and is inactivated through phosphorylation by ERK, a member of the MAPK cascade [21, 24-27]. The most well characterized mammalian CIC target genes are the ETS transcription factor family genes

*ETV1/4/*5 which have been found to be upregulated in multiple cancers with *CIC* aberrations and to drive many oncogenic phenotypes [28-33].

The status of *CIC* has recently become a topic of interest in cancer because *CIC* aberrations have been associated with various cellular processes involved in worse overall patient outcome [29, 31, 34, 35]. Aberrations in *CIC* were first identified in undifferentiated small round cell sarcoma, also referred to as Ewing-like sarcoma (ELS). A subset of these tumours were found to harbor a *CIC-DUX4* translocation event resulting in the fusion of the C-terminal of CIC (exon 20) to the trans-activating domain of DUX4 (exon 1), transforming CIC from a transcriptional repressor to an activator [32, 36]. *CIC* fusion events involving other partners have also been identified in ELS (*CIC-FOXO4*) [37, 38], peripheral neuroectodermal tumours (*CIC-NUTM1*) [39, 40], and angiosarcoma (*CIC-LEUTX*) [41]. One fusion event involving the CIC interactor ATXN1 (*ATXN1-NUTM1*) has also been identified in a primitive brain tumour [42]. Although *CIC-DUX4* fusions are the most prevalent, *CIC* rearrangements have been found to behave promiscuously as many tumours with *CIC* rearrangements do not have known partners [43].

Recurrent mutations in *CIC* were later identified in ODG, or Type I LGG (Figure 1.2) [5, 7, 8]. Subsequent studies have identified *CIC* mutations in stomach adenocarcinoma [28], lung adenocarcinoma [31], breast carcinoma [44], colorectal carcinoma [45], melanoma [46], and multiple myeloma [47]. Interestingly, recurrent missense mutations in the HMG-box DNA binding domain and C1 motif have only been observed in ODG, suggesting that the biology of *CIC* mutation in ODG may be unique. Additionally, clonally distinct *CIC* mutations, in an otherwise low mutation burden tumour, have also been identified in ODG suggesting that there is a high selective pressure towards clones which escape CIC regulatory function [4, 48]. Interestingly, *CIC* mutations have not been identified in other glioma subtypes [5, 7, 8, 49]. In ODG, *CIC* mutations have been associated with a more aggressive phenotype and poorer prognosis [34, 50, 51]; similar outcomes have also been observed in other cancer types harbouring *CIC* aberrations which may be due to upregulation of the MAPK signaling pathway and oncogenic ETS transcription factors *ETV1/4/5* [28-34, 36, 52]. *CIC* mutations have also been found to cooperate with IDH mutation to regulate 2HG levels [53], an oncometabolite produced by mutant IDH that is central to initiation and maintenance of the glioma hypermethylator phenotype [17].

Homozygous and heterozygous deletions of *CIC* have been observed in prostate adenocarcinoma [54], stomach adenocarcinoma [28], neuroblastoma [55], and astrocytoma [54]. Lastly, reduced CIC protein expression has been observed in prostate adenocarcinoma [56], hepatocellular carcinoma [33] and glioblastoma [57]. Altogether, the high prevalence of *CIC* aberrations and CIC dysregulation in a plethora of different cancer types supports CIC's role as a transcription factor with potent pan-cancer tumour suppressor functions [58].

Figure 1.2 – Frequency of *CIC* mutations and copy number loss in cancer

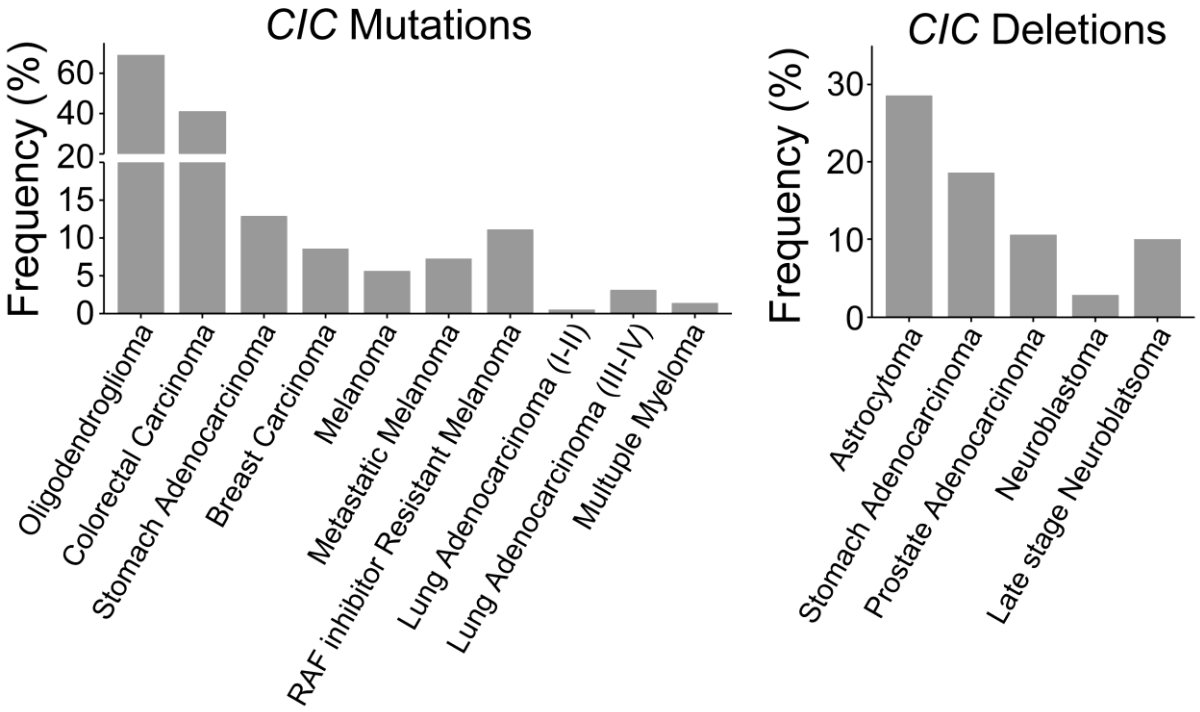

1.3.2 *CIC* in Mammalian Development and Oncogenesis

Following the discovery of recurrent *CIC* mutations in ODG, several mouse models have been used to investigate the role of *CIC* mutation in gliomagenesis. The mouse (*Cic*) and human (*CIC*) orthologs were first identified in developing granule neurons as a transiently expressed factor [20]. Patients which harbor germline heterozygous loss of function *CIC* mutations have presented with several neurodevelopmental disorders [59]. Similarly, homozygous deletion of *Cic* in the developing mouse forebrain (*EMX1-Cre*) or hypothalamus/amygdala (*Otp-Cre*) result in a spectrum of neurodevelopmental disorders [59]. Lineage specific knockout of *Cic* in embryonic neural precursor cells compromised the differentiation of neuroblasts to neurons (*Nes-Cre*) and promoted arrest as *OLIG2* positive oligodendroglial progenitor cell-like state

(*FOXG1-Cre*) [60]. In both studies, loss of *Cic* resulted in reduced cortical thickness, decreased brain size, hyperproliferation of the sub-ventricular zone, and partial post-natal lethality [59-62]. While *Cic* loss was found to result in the onset of cellular behaviors characteristic of gliomas, the spontaneous formation of glioma was not observed; supporting the notion that preceding events such as IDH mutation are required for transformation [4, 17, 63], and that loss of CIC in ODG occurs later [64].

Figure 1.3 – The role of *CIC* in murine development

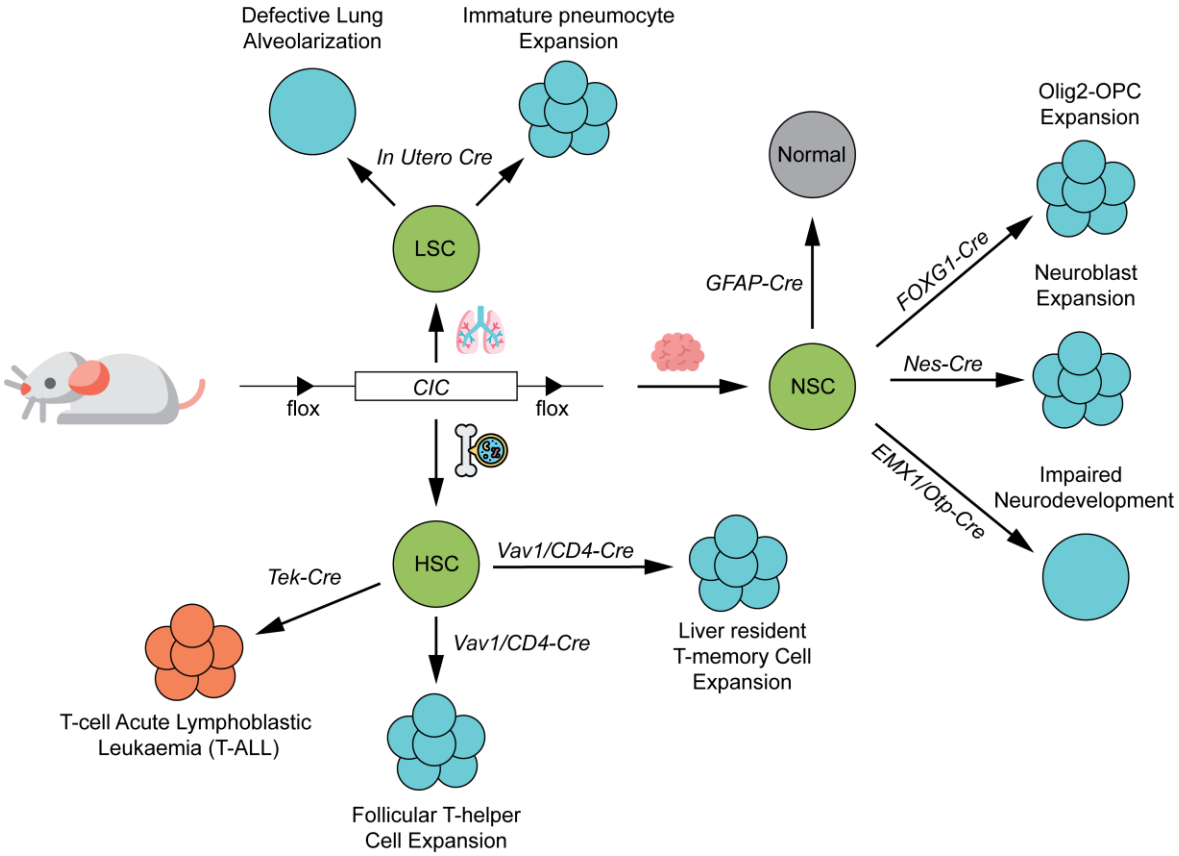

In addition to neurogenesis, CIC has also been identified as an important developmental regulator of other organ systems such as lung, liver, and immune. Homozygous embryonic deletion of *Cic* or destabilization of CIC through homozygous deletion of *ATXN1* and/or *ATXN1L* resulted in defective lung alveolarization, [65] impaired alveolar maturation, and insufficient surfactant production [52]. Lung alveolarization defects were due to the derepression of *ETV4* and *MMP9*, a matrix metallopeptidase responsible for breakdown of extracellular matrix [65]. Homozygous *Cic* knockout mice also displayed impaired bile acid homeostasis and metabolism, which was attributed to the downregulation of several hepatic transcriptional

regulators, upregulation of proinflammatory cytokines [66], and overexpansion of liver-resident memory T-lymphocytes (T-cells) [67]. Spontaneous T-cell activation and enhanced follicular helper T-cell differentiation, mediated by *ETV5* overexpression, was also observed in hematopoietic lineage specific (*Vav1-Cre*) and T-cell specific (*CD4-Cre*) *Cic* knockout mice which establishes CIC as an important factor in lineage specification and maturation of T-cells. Lastly, the only malignant tumour found to be initiated by *Cic* loss in murine models is the induction of T-cell acute lymphoblastic leukemia (T-ALL) (*Tek-Cre*) which was mediated by *ETV4* derepression and activation of an oncogenic *RAS* transcriptomic signature [52, 68]. Together, these studies provide strong evidence of the potent tumour suppressor function of CIC in regulating proliferation and differentiation in various stem and progenitor lineages across all three primary germ layers (Figure 1.3).

1.4 ATXN1L in Development

Dysregulation of CIC target genes has also been implicated in the neuropathology of spinocerebellar ataxia 1 (SCA1) through aberrant binding of CIC to mutant Ataxin1 (ATXN1) [59, 69-71]. The neurotoxicity caused by mutant ATXN1-CIC complexes was later shown to be relieved through competitive binding of CIC to the ATXN1 homologue, Ataxin-1-Like (ATXN1L) [72, 73]. ATXN1 and ATXN1L are members of the Ataxin protein family and share an ataxin-1 and HMG-box protein 1 (AXH) domain required for interaction with CIC [73, 74] and have been reported to interact with CIC in multiple contexts including development and disease state [59, 65, 66, 72]. Previous studies utilizing mouse models to study development and SCA1 pathology have indicated some level of functional redundancy between ATXN1 and ATXN1L, which is also supported by the high degree of protein homology [73]. These studies also highlighted that loss of ATXN1L affected CIC function much more profoundly and robustly compared to loss of ATXN1 in murine models [65, 66]. ATXN1 and ATXN1L have also been reported as regulators of Notch signalling through repression of *HEY1*, a gene downstream of Notch activation [75]. One study has also suggested that ATXN1L may be involved in maintaining hematopoietic stem cell quiescence and renewal through the regulation of *HOXA7* and *HOXA9* [76]. However, additional characterized targets of ATXN1L remain elusive and its role in regulating CIC function in cancer remains unclear.

1.5 Thesis

Although significant progress has been made in the past two decades in understanding the molecular alterations involved in gliomagenesis, treatment options remain limited and rarely involve targeted therapy. In order to develop targeted therapies, a deeper understanding towards the molecular mechanisms and downstream consequences of these alterations is required. Alterations in *CIC* were first discovered in ODGs, however, it is clear now that loss or altered function of this tumour suppressor is a potent driver of pathways associated with poor prognosis such as metastasis, invasion, treatment resistance, and progression in several cancers. One aspect of CIC function is the molecular relationships CIC forms between its interacting partners and how they may modulate CIC function. By studying the regulation of CIC at a post-translational level, we may find targets to potentially re-establish normal CIC function as a therapeutic target.

1.6 Objectives and Hypothesis

The primary objective of this thesis is to investigate the functional relationship between CIC and ATXN1L with the goal of further understanding the role of ATXN1L as a CIC interacting partner and their relationship in cancer.

I hypothesize that the interaction between CIC and ATXN1L is vital to the normal function and stability of CIC and that loss of either proteins can be leveraged by cancers to drive cancer progression.

1.7 Specific Aims and Thesis Outline

To address the objective and hypothesis, the following specific aims were devised:

Aim 1: Comprehensively characterize and compare the transcriptomic effects of *ATXN1L* loss and *CIC* loss in *in vitro* cell lines and patient tumours.

Chapter 3 describes the *in vitro* establishment of the interaction between CIC and ATXN1L, generation of *ATXN1L*^{KO} cell lines, downstream transcriptomic investigations, validation using TCGA patient cohorts, and *in vitro* assessment of the mechanism. Comprehensive and comparative transcriptomic analysis of *CIC*^{KO} and *ATXN1L*^{KO} cell lines revealed for the first time, the extent that *CIC* loss and *ATXN1L* loss converge transcriptomically both at the gene and pathway level which were also validated in three TCGA cohorts. This data

suggests that the loss of *ATXN1L* may be a mechanism of modulating CIC function in several cancer types in addition to the *CIC* aberrations already reported in the literature.

Aim 2: Investigate the post-translational regulation of CIC by ATXN1L and vice versa.

Chapter 4 describes *in vitro* experiments that establish a reciprocal functional relationship between CIC and ATXN1L whereby loss of one interacting partner results in the post-translational dysregulation of the other partner. CIC and ATXN1L were found to promote each other's protein stability and cellular localization. Loss of ATXN1L promoted ERK independent proteasomal degradation of CIC through ubiquitination by the E3-ligase TRIM25. These observations were further validated using transcriptomic analyses of the TCGA breast carcinoma and liver hepatocellular carcinoma cohorts. This study establishes the mechanism of CIC dysregulation through ATXN1L loss as well as reveal a novel CIC degradation pathway independent of canonical ERK mediated CIC degradation.

Aim 3: Investigate the role and effects of IDH mutation on the functional relationship between CIC and ATXN1L.

Chapter 5 describes and explores the effects of *IDH1-R132H* mutation on the transcriptomic relationship between *CIC* and *ATXN1L*. Comparative transcriptomic analysis of CIC^{KO} and $ATXN1L^{KO}$ cell lines in *IDH1* wildtype and *IDH1-R132H* mutant backgrounds was performed. IDH was found to "dampen" the effects of *CIC* or *ATXN1L* loss on the global transcriptome, though did not affect the dysregulation of pathways related to MAPK and cellular growth.

Chapter 2: Materials and Methods

2.1 Immunoprecipitation

For each cell line and replicate, one to two 15cm plate at roughly 70-80% confluency were harvested and lysed using Pierce™ IP Lysis Buffer (Thermofisher Scientific, Waltham, MA, USA [ThermoSci]) supplemented with Halt™ Protease and Phosphatase Inhibitor Cocktail (ThermoSci). Lysates were incubated on ice for 30 minutes and homogenized by passing through a 25 gauge needle 15-20 times followed by incubation on ice for 30 minutes. Insoluble cell debris was pelleted down by centrifugation at 13000 rpm for 15 minutes at 4ºC. 1mg of protein for each replicate was blocked using 40µL of Sepharose® 4B beads (Sigma Aldrich, St. Louis, MO, USA [Sigma]). Pierce™ Protein A/G Plus Agarose Beads or Dynabeads™ (ThermoSci) were preblocked using 1% BSA, rotating for 1 hour at 4ºC. Conjugation of anti-CIC, anti-ATXN1L, anti-FLAG or control IgG antibody to agarose/Dynabeads (ThermoSci) beads was performed by adding 1-7.5 µg of antibody to the preblocked beads in 1mL of 1% BSA. Conjugated beads were pelleted down. Blocked lysate was added to conjugated beads and incubated, rotating for 3 hours at 4ºC. Beads were pelleted down and washed 3x in IP lysis buffer followed by suspension in 4x loading buffer and 10x reducing agent. Beads were boiled at 95ºC for 8 minutes to release captured protein.

2.2 Cell Lysate Preparation

Whole cell lysate was prepared by resuspending cell pellets with 3-5x ice cold RIPA buffer (Santa Cruz Biotechnology, Dallas, TX, USA [SantaCruz]) according to manufacturer's protocol with fresh supplemented Halt™ Protease and Phosphatase Inhibitor Cocktail (ThermoSci). Lysates were incubated on ice for 1 hour and insoluble cell debris was pelleted at 13000rpm for 15 minutes at 4ºC. Protein was quantified using BCA assay (ThermoSci) and normalized samples were prepared with 4x loading buffer (ThermoSci) and 10x reducing agent (ThermoSci).

2.3 Western Blot

Samples were separated using gel electrophoresis on NuPage 3-8% Tris-Acetate gels run (Life Technologies, Carlsbad, CA, USA [Life Tech]) in 1x Tris-Acetate running buffer (Life Tech) or NuPage 10% Bis-Tris gels (Life Tech) run in 1x MOPS running buffer (Life Tech).

Running buffers were supplemented with oxidizing agent (Life Tech). Electrophoresis was run at 100V for 25minutes followed by 150V for 1-2.5 hours. Separated proteins were transferred onto methanol activated PVDF membrane (Millipore, Burlington, MA, USA) for 70-120 minutes at 100V in 1x transfer buffer (Life Tech) with 20% methanol. Membranes were blocked with 5% skim milk in TBS with 0.01% Tween (TBS-T) for one hour at room temperature followed by overnight incubation in primary antibody. Membranes were incubated with HRP conjugated secondary antibody (SantaCruz) for 1 hour at room temperature and washed 3x 30 minutes in TBS-T before and after secondary antibody incubation. Protein signal detection was performed using either ECL substrate (Bio-Rad, Hercules, CA, USA [BioRad]) or SuperSignal West Femto substrate (ThermoSci). Antibody information can be found in Supplemental Materials 1. Images were captured using a ChemiDoc MP Imager (BioRad) or ImageQuant LAS4000 (GE Healthcare, Chicago, IL, USA) and protein quantifications were performed using ImageJ software.

2.4 Real-Time quantitative PCR (RT-qPCR)

RNA extraction was performed using the RNeasy Mini Kit (74104, Qiagen, Hilden, Germany) according to manufacturer's protocol. 1µg of template RNA was used for cDNA conversion using SuperScript™ III First-Strand Synthesis System (Invitrogen, Carlsbad, CA, USA) according to manufacturer's protocol. RT-qPCR was performed using 4-12.5ng of template cDNA with PowerUp™ SYBR™ Green Master Mix (Applied Biosystems, Beverly Hills, CA, USA) according to manufacturer's recommended reaction component amounts and cycling conditions. RT-qPCR reactions were run on a QuantStudio 6 Flex Real-Time PCR System using QuantStudio™ Real-Time PCR Software to generate CT values. Analysis of relative mRNA expression was performed using the 2-ΔΔCT method with TATA-box binding protein (TBP) expression as an endogenous control. Sequences of the RT-qPCR primers used are provided in Supplemental Materials 2.

2.5 Cell Culture Conditions

The HEK293a cell line was obtained from Dr Gregg Morin (Canada's Michael Smith Genome Sciences Centre, Vancouver, BC, Canada) and authenticated by Genetica DNA Laboratories (Cincinnati, Ohio, USA). Wildtype IDH1-stable NHA cell line [77] was purchased from Applied Biological Materials (ABM) Inc. (T3022, Richmond, BC, Canada). U251 and U343 glioblastoma cells were obtained from Dr Shoukat Dedhar (BC Cancer Research Center,

Vancouver, BC, Canada) and LN18, LN229, and U87-MG glioblastoma cells were obtained from Dr Kevin Bennewith (BC Cancer Research Center, Vancouver, BC, Canada). The *CIC-DUX4* sarcoma line (NCC-CDS-X1-C1) [78] was obtained from Dr Tadashi Kondo (National Cancer Center, Tokyo, Japan). HEK293a, NHA, HOG, U87-MG, U251, and U343 cell lines were cultured in Dulbeccos modified Eagle's medium (DMEM; Life Technologies) supplemented with 10% fetal bovine serum (FBS) (Life Technologies) and 5% FBS for LN18 and LN229 cell lines. NCC-CDS-X1-C1 cell line was cultured in RPMI (Life Technologies) supplemented with 10% FBS. BTIC cell lines MGG119 [79], BT54, and BT88 [80] were cultured in serum free Neural Basal Media (Life Technologies) supplemented with N2/B27 (Gibco) and EGF/FGF (20ng/mL; Peprotech). All cultures were maintained in a 37ºC, 5% CO_2 incubator. Cells were tested and verified to be mycoplasma free using MycoFluor™ Mycoplasma Detection Kit (Invitrogen). Unless otherwise stated, cells were washed once with PBS and harvested via scraping or centrifugation at 70-90% confluency. *ATXN1*L^{KO} cell lines were generated using the CRISPR/Cas9 genome editing technology as previously described [54]. A table of cell lines used and their genetic background can be found in Supplemental Materials 4 and 5.

2.6 ATXN1L CRISPR Knockout

HEK derived *ATXN1L*^{WT} (N4 and N8), *ATXN1L*^{KO} (A10, A30 and B21) and NHA derived *ATXN1L*^{KO} (B82, B16, and B21) cell lines were generated using CRISPR/Cas9 genome editing technology. CRISPR guide sequences against exon 1 of *ATXN1L* were designed using the online CRISPR Design tool (http://crispr.mit.edu). CRISPR/Cas9 guide sequences were cloned into the construct pSpCas9(BB)-2A-Puro (PX459) V2.0 (Addgene, Watertown, MA, USA) following the Zhang protocol (http://www.genome-engineering.org/crispr/wpcontent/uploads/2014/05/ CRISPR-Reagent-Description-Rev20140509.pdf). *ATXN1L* target sequences are as follows: ATXN1L_Exon1_A (5'-CACCGACCTGTTCATGAAAGGAGTC-3') and ATXN1L_Exon1_B (5'-CACCGCAGCCGCTGGACCTTGCTCC-3'). HEK cells were transfected with the CRISPR/Cas9 construct targeted against *ATXN1L* using TurboFect™ Transfection Reagent (ThermoSci) and selected in media containing Puromycin. NHA cells were transfected with the CRISPR/Cas9 construct targeted against ATXN1L using TransIT-X2® Dynamic Delivery System (Mirus Bio LLC, Madison, WI, USA) and selected in media containing puromycin. Cells

were selected for 72 hours and then seeded at 200 cells/15cm dish. Single colonies were selected using cloning cylinders 7-14 days post seeding and transferred into 96 well plates. Each clone was screened for ATXN1L expression using Western Blot. Clones without detectable ATXN1L protein expression were further Sanger sequenced to confirm genome editing at the targeted site.

2.7 siRNA Transfection

Cells were transfected at 70% confluency with Silencer Select (Life Tech) and Stealth RNAi (Invitrogen) targeted at *ATXN1L*, *ATXN1*, or *TRIM25*. Targeted siRNA information can be found in Supplemental Materials 3. Each siRNA was tested independently prior to pooled siRNA experiments (data not shown). Control transfections were performed with Stealth RNAi™ siRNA Negative Control, Med GC (12935300, ThermoSci) or BLOCK-iT Fluorescent Oligo (13750062, Invitrogen). Transfections were performed using Lipofectamine® RNAiMAX Transfection Reagent (Life Tech) for HEK cells or TransIT-X2® Dynamic Delivery System (Mirus Bio LLC, Madison, WI, USA) for all other adherent cell lines. Neurosphere cell lines (MGG119, BT054, BT088) were transfected using nucleofection (Mouse Neural Stem Cell Nucleofector Kit: VPG-1004, Lonza, Basel, Switzerland) according to manufacturer's protocol. FLAG-tagged ATXN1L construct was purchased from Addgene (#33242) [72]. Cells were harvested 24-72 hours post transfection for experiments.

2.8 Microarray Expression Profiling

The following cell lines were subjected to microarray expression profiling using GeneChip Human Gene 2.0 ST array (Affymetrix, Santa Clara, CA, USA) at the Centre for Applied Genomics (The Hospital for Sick Children, Toronto, Canada) in triplicate (three separate passages): three HEK derived *ATXN1L*^{WT} cell lines (parental HEK, and two scramble treated CRISPR controls N4 and N8), three HEK derived *ATXN1L*^{KO} cell lines (A10, A30 and B21), the parental *CIC*^{WT}/*ATXN1L*^{WT} NHA cell line, two NHA derived *CIC*^{KO} cell lines (A2 and H9), and one NHA derived *ATXN1L*^{KO} cell line (B82). Total RNA was extracted using the RNeasy Mini Kit (Qiagen, Halden, Germany) according to manufacturer's protocol. Gene annotation was performed with the R/Bioconductor package hugene20sttranscriptcluster.db (version 8.5.0), and only transcript clusters that mapped to single genes were retained for further analyses. Multiple transcript clusters that mapped to identical genes were aggregated using mean expression values. Expression values for each gene were averaged across all HEK or NHA *ATXN1L*^{WT}/*CIC*^{WT} cell lines and replicates, respective to the analysis. Differentially expressed genes were identified

using fold-change (FC) differences in gene expression between each individual *ATXN1L*^{KO}/*CIC*^{KO} replicate and the average *ATXN1L*^{WT}/*CIC*^{WT} expression. Genes with an FC value of >1.5 in at least 4/9 (HEK *ATXN1L*^{KO}), 3/6 (NHA *CIC*^{KO}), and 2/3 (NHA *ATXN1L*^{KO}) comparisons were considered to be differentially expressed [28, 81]. The data are accessible through the Gene Expression Omnibus (dataset GSE103515).

2.9 TCGA Expression Analyses

RNA-sequencing results were obtained from The Cancer Genome Atlas (TCGA) using http://firebrowse.org/ (doi:10.7908/C11G0KM9) and mutation and copy number data were obtained from TCGA using http://www.cbioportal.org/ [82, 83]. Differential expression analysis of Lower Grade Gliomas (LGG), Prostate Adenocarcinoma (PRAD), Stomach Adenocarcinoma (STAD), and Breast Carcinoma (BRCA) TCGA cohorts was performed using the R package DEseq2 [84]. The LGG cohort was stratified into three subgroups based on IDH mutation and 1p19q-codeletion status [4]. Tumours harbouring IDH mutation and 1p19q-codeletion were grouped as Type I tumours and differential expression analysis was performed between *CIC* mutated (Type I LGG$^{CIC\text{-Mut}}$) (Truncating and Nonsense mutations, n=39) and Type I LGG$^{CIC\text{-WT}}$ (n=68) samples. IDH mutated, 1p19q retained tumours were grouped as Type II tumours and differential expression analysis was performed comparing samples with heterozygous/homozygous deletions in *ATXN1* or *ATXN1L* without *CIC* copy number variations (deletions and amplifications) (CNVs) (Type II-LGG$^{ATXN1/ATXN1L\text{-}Del}$, n=9), or samples with heterozygous/homozygous deletions in *CIC* without *ATXN1* or *ATXN1L* CNVs (Type II-LGG$^{CIC\text{-}Del}$) (n=30), with samples harbouring no CNVs in *ATXN1L*, *ATXN1* or *CIC* (Type II-LGG^{WT}) (n=66). Type III tumours, defined as IDH wildtype, were not analyzed in this study. In the PRAD cohort, Differential expression analysis was performed comparing samples with homozygous/heterozygous deletions in *CIC* without *ATXN1L* CNVs (PRAD$^{CIC\text{-}Del}$) (n=18), or samples with homozygous/heterozygous deletions in *ATXN1L* without *CIC* CNVs (PRAD$^{ATXN1L\text{-}Del}$) (n=80), with samples harbouring no *CIC*, *ATXN1* or *ATXN1L* CNVs (PRAD^{WT}) (n=143). In the STAD cohort, differential expression analysis was performed using samples with homozygous/heterozygous deletions in *CIC* (STAD$^{CIC\text{-}Del}$) (n=10), *ATXN1L* (STAD$^{ATXN1L\text{-}Del}$) (n=23), *ATXN1* (STAD$^{ATXN1\text{-}Del}$) (n=20), or deletions in at least 2/4 alleles of *ATXN1L*/*ATXN1* (PRAD$^{ATXN1/ATXN1L\text{-}Del}$) (n=14), with samples harbouring no CNVs in *CIC*, *ATXN1L* or *ATXN1* (STAD^{WT}) (n=95). In the LGG, PRAD, and STAD cohorts, only wildtype samples with *ATXN1*,

ATXN1L or *CIC* expression, respective to the analysis, above the first quartile were used to reduce the possibility of secondary mechanisms other than CNVs affecting transcriptional regulation of *ATXN1*, *ATXN1L* and *CIC* [85]. Lastly, for the BRCA cohort, differential expression analysis was performed comparing samples with *TRIM25* amplification (n=73) with samples with copy neutral *TRIM25* (n=449). A table of all TCGA Samples used for analyses can be found in Supplemental Table 1.

2.10 Gene Set Enrichment Analysis

The Metascape software (http:/metascape.org) was used to perform functional enrichments using the multiple gene lists mode [86]. Gene ontology (GO) Biological Processes, Hallmark Gene Sets and Oncogenic Signatures were used for enrichment analyses of all DE genes, with a p-value cut-off of 0.05, and a minimum enrichment of 1.5. Only terms with a BH-adjusted p-value < 0.05 were retained.

2.11 Targeted Chromatin Immunoprecipitation-PCR

For each cell line (HEK, D10, A30) and replicate, two ~70-80% confluent 15cm plates were treated with 1% formaldehyde (Sigma Aldrich, St. Louis, MO, USA) in PBS for 12 minutes with gentle rocking, followed by treatment with 0.125M glycine (Sigma) for five minutes. Crosslinked cells were combined and pelleted using centrifugation at 1200rpm for 5 minutes at room temperature, resuspended in 450µL ChIP lysis buffer (50mM Tris-HCl pH 8.0, 1% SDS, 10mM EDTA, 1X Phosphatase and Protease Inhibitor cocktail (PIC) [ThermoSci]), and lysed on ice for 30 minutes. Cells were homogenized by 6 passages through a 20-gauge needle, and nuclei were pelleted by centrifugation at 5000rpm for 10 minutes at 4ºC. The pellet was resuspended in 900µL shearing buffer (10mM Tris-HCl pH 8.0, 0.1% SDS, 1mM EDTA, 1X PIC) and transferred to a 1mL milliTUBE with AFA fiber (D-Mark Biosciences, Toronto, ON, Canada) using a 30-gauge needle. Chromatin was sonicated using a Covaris S2 sonicator using the following settings: 10% duty cycle, 6 intensity, 500 burst, 16 cycles (20s on, 40s off) at 4-6ºC. Insoluble debris and unfragmented chromatin were removed by centrifugation at 14000rpm for 12 minutes at 4ºC. An aliquot of chromatin was de-crosslinked overnight at 68ºC (0.2M NaCl, 0.05mg/mL RNase), treated with proteinase K for 30 min at 42ºC, and purified using the MinElute PCR Purification Kit (28006, Qiagen, Halden, Germany) to allow determination of chromatin concentration using the Qubit dsDNA high sensitivity assay (Life Tech) and confirmation of sufficient DNA fragmentation to a 150-300 bp size range on a bioanalyzer using

High Sensitivity DNA Chips (Agilent Technologies, Santa Clara, CA, USA). Protein A Dynabeads (Life Tech) blocked with bovine serum albumin and salmon sperm DNA for 3h were used to pre-clear chromatin for 2h. For the immunoprecipitation, three volumes of IP buffer (10mM Tris-HCl pH 8.0, 1% Triton X-100, 0.1% deoxycholate, 0.1% SDS, 90mM NaCl, 2mM EDTA, 1x PIC) were added to 22.5µg of chromatin, which was then incubated with 2.5µg of anti-CIC antibody for 1h at 4ºC. Blocked Protein A Dynabeads (25µL) were then added to the chromatin and antibody and incubated overnight at 4ºC. The samples were then washed twice in low salt buffer (20mM Tris-HCl pH 8.0, 0.1% SDS, 1% Triton X-100, 2mM EDTA, 150mM NaCl) and twice in high salt buffer (same as low salt buffer except 300mM NaCl). DNA was eluted in 100mM sodium bicarbonate with 1% SDS and 0.05mg/mL RNase at 68ºC for 6 hours, followed by treatment with proteinase K for 30 min at 42ºC. For each IP, 100ng of chromatin was subject to the same treatment to serve as input controls. Eluted DNA was purified using the MinElute PCR. Purification Kit, and qPCR analysis was performed as described above using the PowerUp SYBR® Green PCR Master Mix (Life Tech) according to the manufacturer's recommended reaction component amounts and cycling conditions. Percent input values were calculated for each site, and reported as fold-change differences compared to NCR1. Two-sided Student's t-tests were used to assess differential expression. Sequences of the qPCR primers used are provided in Supplemental Materials 6.

2.12 Proximity Ligation Assay

Cells were seeded and cultured on glass coverslips for 24-72 hours and fixed directly to the coverslip by adding equal volume of 4% PFA to media and incubating for 20 minutes at room temperature followed by fresh 4% PFA and incubated at room temperature for a further 20 minutes. Fixed cells were washed in PBS and permeabilized using 0.2% Triton X-100 at room temperature for 20 minutes. Proximity ligation assay was performed according to protocol using Duolink® PLA Technology (Sigma Aldrich, St. Louis, MO, USA).

2.13 Site Directed Mutagenesis

FLAG-tagged CIC-S (V41G) and ATXN1L (V485A) construct was generated using the QuikChange Lightning Site-Directed Mutagenesis Kit (210518, Agilent Technologies, Santa Clara, California, USA) according to manufacturer's protocol. The primer sequence was targeted at residue 41 of CIC-S (5'- CCTTGGCACTCCTTAGGCCCCTTCCTGGCACCC - 3'). The

wildtype FLAG-tagged CIC-S used was previously described [53]. The primer sequence was targeted at residue 485 of ATXN1L (5' – GAGCTGAAGCGGGCGGAGGACCTCCAG – 3').

2.14 Antibody Generation

ATNX1L custom antibody was generated in Rabbit against residues 275-295 and 619-636 of ATXN1L by ProSci – Custom Antibodies (Poway, CA, USA). Antibodies were affinity purified from the rabbit serum and validated using siRNA knockdown controls.

2.15 Immunofluorescence

Cells were seeded and cultured on glass coverslips for 24-72 hours and fixed directly to the coverslip by adding equal volume of 4% PFA to media and incubating for 20 minutes at room temperature followed by fresh 4% PFA and incubated at room temperature for a further 20 minutes. Fixed cells were washed in PBS and permeabilized using 0.2% Triton X-100 at room temperature for 20 minutes. Fixed cells were blocked in 2.5% BSA for one hour followed by overnight incubation at 4ºC in primary antibody diluted in blocking solution. Fixed cells were washed 3x with PBS and incubated at room temperature with Alexa Fluor 488 or Alexa Fluor 546 conjugated secondary antibody (Invitrogen), diluted in blocking solution for one hour. Stained cells were washed in PBS and incubated in DAPI (Invitrogen), diluted in PBS for 5 minutes. Stained cells were mounted onto a slide using ProLong™ Gold Antifade Mountant (Invitrogen). Images were captured on Zeiss LSM800 confocal microscope using Airyscan or Colibri Upright LED based microscope using ZEN microscope software. Antibody information can be found in Supplemental Materials 1.

2.16 Cellular Fractionation

Nuclear and cytoplasmic fractionations were performed using the NE-PER™ Nuclear and Cytoplasmic Extraction kit (ThermoSci) according to manufacturer's protocol. 20 µg of cytoplasmic protein and 5µg of nuclear protein were prepared for western blot.

2.17 Fractionation Immunoprecipitation

For each cell line, two 15cm plates at roughly 70-80% confluency were harvested and lysed using Cytoplasmic Lysis Buffer (10mM Tris-HCl, 10mM NaCl, 2mM $MgCl_2$, 1mM EDTA, 0.05% NP-40, and 1X Phosphatase and Protease Inhibitor cocktail (PIC) [ThermoSci])

on ice for 10 minutes with agitation every 2 minutes. Nuclei were pelleted at 500rpm for 5 minutes and washed 3x with Wash Buffer (10mM Tris-HCl, 10mM NaCl, 2mM $MgCl_2$, 1mM EDTA, and 1X Phosphatase and Protease Inhibitor cocktail (PIC) [ThermoSci]). Nuclei were lysed using Nuclear Lysis Buffer (250mM NaCl, 20mM Na_3PO_4, 30mM $Na_4P_2O_7$, 5mM EDTA, 10mM NaF, 10% Glycerol, 1% NP-40, 1mM DTT, and 1X Phosphatase and Protease Inhibitor cocktail (PIC) [ThermoSci]) on ice. Nuclei were passed through a 25 gage needle 20 times and incubated on ice for 30 minutes with agitation every 5 minutes. Lysates were cleared by centrifugation at 13000rpm for 15 minutes and immunoprecipitation was performed as described above.

2.18 Phosphatase Treatment

40µg of protein lysate prepared using NP40 lysis buffer (150mM NaCl, 1.0% NP-40, 50mM Tris-HCl, pH 8.0) was treated with 1µL (400U) of Lambda Protein Phosphatase (New England BioLabs, Ipswich, MA, USA) at 30ºC for 2 hours using manufacturer's recommended reagent quantities. Treated lysates were suspended in loading buffer and reducing agent and denatured at 95ºC for 8 minutes.

2.19 Drug treatments

The HEK and NHA cell lines were treated with 25µg/mL and 100µg/mL of Cycloheximide, respectively. Cells were harvested at the specified time points. Both HEK and NHA cell lines were treated overnight for 16 hours with 10µM of MG132 prior to harvesting. Cell lines were treated with 20ng/mL of recombinant EGF/FGF (Peprotech, Rocky Hill, New Jersey, United States) following >16 hours of serum starvation. Samples were harvested at specified times. LY3214996 was used for ERK inhibition at a concentration of 10nM. Trametinib was used for MEK inhibition at a concentration of 5nM. Both drugs were dissolved in DMSO. Cell lines were treated for the specified amount of time, or 16 hours.

2.20 *In Silico* Protein Analysis

ATXN1L nuclear localization signal prediction was performed using http://nls-mapper.iab.keio.ac.jp with a cut-off score of 3.0 across the whole amino acid sequence [87]. ATXN1L Phosphorylation site prediction was performed using http://scansite3.mit.edu/. CIC-S ubiquitination site prediction was performed using HCKSAAP-UbSite [88].

2.22 mRNA sequencing

Total RNA was extracted using the RNeasy Mini Kit (Qiagen, Halden, Germany) according to manufacturer's protocol. Sample quality control was performed using the Agilent 2100 Bioanalyzer. Samples were then prepped following the standard protocol for the NEBnext Ultra ii Stranded mRNA (New England Biolabs). Sequencing was performed on the Illumina NextSeq 500 with Paired End 42bp × 42bp reads. De-multiplexed read sequences were then aligned to the reference sequence using STAR aligners [89]. Assembly was estimated using Cufflinks (http://cole-trapnelllab.github.io/cufflinks/) [90] through bioinformatics apps available on Illumina Sequence Hub. Two independent monoclonal knockouts with 3 biological replicates from different passages were sequenced for each knockout condition. NHA *CIC*^{KO} cell lines were generated as per LeBlanc *et al.* [28], and NHA *ATXN1L*^{KO} cell lines were generated per above from Wong *et al.* Raw mRNA sequencing files are also available in the Gene Expression Omnibus (GEO) repository (accession number: GSE140471).

2.23 Immunoprecipitation Mass Spectrometry

IP-MS of *ATXN1L*^{KO} NHA cell line B82 was performed using an endogenous CIC antibody. 3 replicates were performed and run alongside IgG negative control IPs. Following IP, proteins were purified and digested using the SP3 method [91]. Replicates and controls were tandem mass tag labeled using a TMT 11-plex reagent set and run through a liquid chromatography/mass spectrometry protocol on an Orbitrap Fusion Tribrid MS platform (Thermo Scientific). Data from the Orbitrap Fusion were processed using the Proteome Discoverer Software. MS2 spectra were searched using Sequest HT [92] against a combined UniProt human proteome database appended to a list of common contaminants. Data were filtered at the peptide spectral match-level to control for false discoveries using a q-value cut off of 0.01 as determined by Percolator [93]. Contaminants were removed prior to downstream analysis. Perseus [94] was used to perform two-sided t-tests to identify proteins that were significantly enriched in each IP experiment compared to their respective IgG controls (FDR < 0.05).

2.24 *TRIM25* gene expression analyses

si*TRIM25* RNA Sequencing data was obtained from Walsh *et al.* (https://doi.org/10.1016/j.celrep.2017.07.052) [95] and only genes with FDR < 0.05 and

directional concordance in both cell lines (BT549 and MDA-MB-231) were considered differentially expressed and used for downstream analyses.

2.25 Immunohistochemistry

Slides were deparaffinised using xylene and a decreasing ethanol gradient. Slides were stained using the Ventana BenchMark automated stainer (Roche, Basel, Switzerland). Normal brain and a normal tissue TMA were used as controls. Stained slides were blind scored by two independent neuropathologists.

Chapter 3: CIC and ATXN1L Regulate the Cell Cycle

3.1 Introduction

CIC has recently been shown have potent tumour suppressor function through the inhibition of several target genes, mainly *ETV1/4/5* which are heavily involved in oncogenic and tumour progression processes. Deficiency or dysregulation of CIC has been shown to promote the development of T-cell acute lymphoblastic leukemia [68], Ewing sarcoma [36] and primitive neuroectodermal tumours [39]; lead to increased metastatic potential or progression in hepatocellular carcinoma [33], lung cancer [31], glioblastoma (GBM) [57], prostate cancer [96], neuroblastoma [55]; and treatment resistance in pancreatic adenocarcinoma [29], multiple myeloma [47], and melanoma [46].

The interaction between CIC and ATXN1L has previously been reported in the context of murine lung development which suggested that loss of ATXN1L result in defective lung development through dysregulation of CIC and its downstream target gene ETV4 [65]. However, the interaction and role of ATXN1L in regard to CIC function has not been well characterized nor investigated at a global transcriptomic level. Furthermore, genomic aberrations in ATXN1L have not been previously reported nor investigated in any cancer contexts.

In this chapter, we explore the physical and functional association between CIC and ATXN1L using novel isogenic cell line models and bioinformatic analyses of patient data from The Cancer Genome Atlas (TCGA) consortium. ATXN1L loss was found to negatively affect the transcriptional repression of known CIC target genes through dysfunctional CIC promoter binding *in vitro*. Transcriptome analyses of $ATXN1L^{KO}$ and CIC^{KO} cell lines demonstrated upregulation of the MAPK signalling cascade. Transcriptome analyses of TCGA low grade glioma, prostate adenocarcinoma, and stomach adenocarcinoma cohorts with loss of *CIC* or *ATXN1/ATXN1L* converged towards upregulation of the mitotic cell cycle through the myc and E2F pathways. This study establishes the CIC-ATXN1-ATXN1L axis as an important regulator of a broad array of pathways that converge upon regulation of the cell cycle.

3.2 Results

3.2.1 ATXN1L is a functional interacting partner of CIC

To validate the CIC-ATXN1L interaction, we performed immunoprecipitation (IP) of endogenous CIC and ATXN1L human embryonic kidney (HEK), human oligodendroglial (HOG) [97], and normal human astrocytes (NHAs) stably expressing IDH1^{WT} [17] (Figure 3.1A-B and Supplemental Figure 1A-D). Proximity ligation assay was also performed using *CIC*^{KO} NHA cells stably expressing FLAG tagged CIC-S. Interactions between FLAG tagged CIC-S and ATXN1L were found to be present in both the cytoplasm and the nucleus (Figure 3.1C). To investigate the functional redundancy of ATXN1 and ATXN1L in relation to their interactions with CIC, *ATXN1* and *ATXN1L* were independently knocked down in HEK and NHA cell lines using pooled targeted siRNAs (Supplemental Materials 3). Following knockdown of *ATXN1L*, the relative expression of CIC target genes (*ETV1/4/5*, *DUSP6*, and *SPRY4*) [28] was found to be affected at a greater frequency and to a greater degree compared to *ATXN1* knockdown, suggesting that the interaction of CIC and ATXN1L may be more relevant for the repression of CIC target genes (Figure 3.1D-E and Supplemental Figure 1E-F).

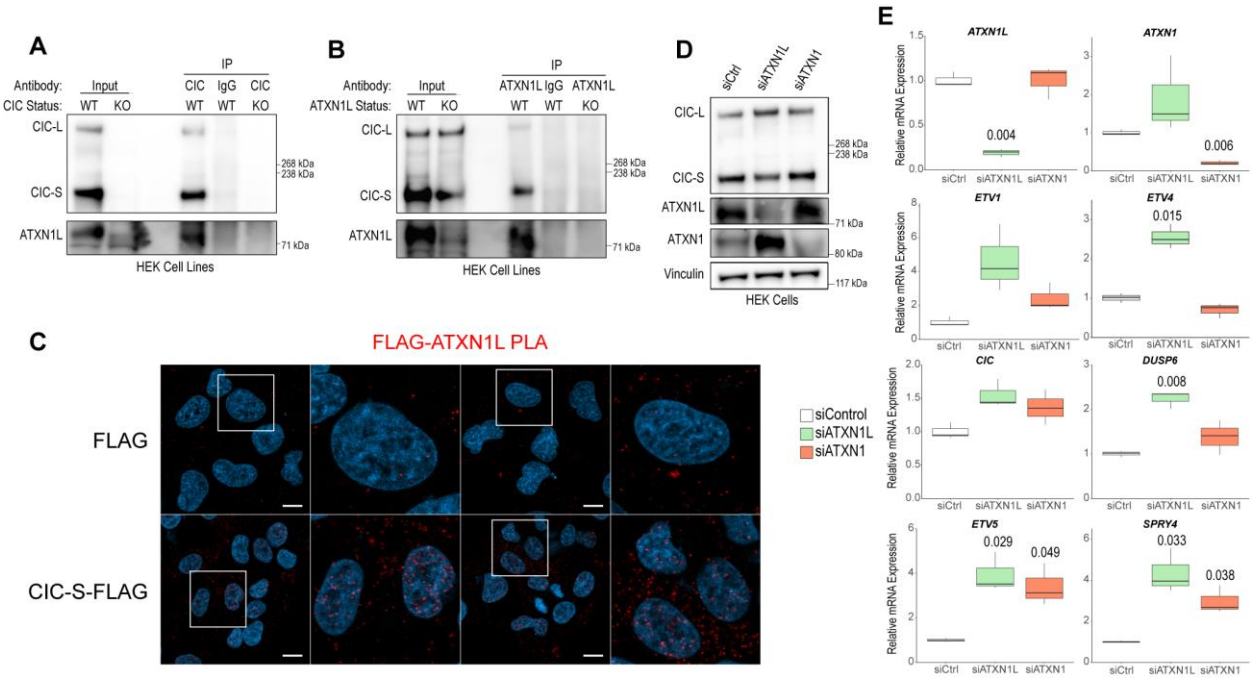

Figure 3.1 – CIC and ATXN1L physically and functionally interact.
(A) Representative western blot of endogenous CIC IP showing co-IP of ATXN1L in HEK cells. A CIC IP in a *CIC*^{KO} cell line (D10) and an IgG IP in the parental HEK were performed as negative controls. (B) Representative western blot of endogenous ATXN1L IP showing co-IP of CIC in HEK cells. An ATXN1L IP in our *ATXN1L*^{KO} cell line (A30) and IgG IP in the parental HEK were performed as negative controls. (C) Immunofluorescence images of FLAG-ATXN1L PLA in *CIC*^{KO} cell lines stably expressing FLAG or FLAG-tagged CIC-S. White bars denote 10µm. (D) Representative western blot of *ATXN1L* and *ATXN1* knockdown using targeted siRNA in HEK cells. A

scrambled siRNA (siCtrl) was used as a negative control and vinculin was used as a loading control. (E) Tukey boxplots showing relative mRNA transcript levels of *ATXN1L*, *ATXN1*, *CIC*, and CIC target genes *ETV1/4/5*, *DUSP6* and *SPRY4* measured by RT-qPCR following independent siRNA knockdown of ATXN1L or ATXN1 for 48 hours in HEK cells. Data were collected from 3 independent experiments and p-values were calculated using the two-tailed independent Student's t-test comparing siATXN1L and siATXN1 to siCtrl.

3.2.3 Generation of ATXN1L CRISPR Knockout Cell Lines

Based on our above observations, we sought to further characterize the transcriptional network of ATXN1L. Using CRISPR/Cas9 genome editing technology [98, 99] targeted at exon 1 of *ATXN1L*, three *ATXN1L*^{KO} HEK-derived (A10, A30, B21) and one *ATXN1L*^{KO} NHA-derived (B82) cell lines were generated that showed no detectable ATXN1L protein expression (Figure 3.2A-B). Genome editing at the CRISPR target site were confirmed by Sanger sequencing (data not shown). CIC target genes *ETV1/4/5* in HEK *ATXN1L*^{KO} (Figure 3C) and *ETV1* in NHA *ATXN1L*^{KO} cells (Figure 3.2D) were found to be derepressed, consistent with our *ATXN1L* siRNA observations. Further, siRNA knockdown of *ATXN1* in *ATXN1L*^{KO} NHA cells did not result in derepression of *ETV4/5* (Supplemental Figure 2) which suggests that regulation of *ETV4/5* in NHA cells by CIC may be independent of ATXN1/ATXN1L or under additional compensatory regulatory networks. CIC-S protein expression was also found to be reduced in *ATXN1L*^{KO} lines (Supplemental Figure 3) despite observing no significant decrease in *CIC* mRNA expression (Figure 3.2C-D). These findings were consistent with previously published data [29, 59, 65]. Reintroduction of ATXN1L-FLAG resulted in slight repression of *ETV4* and *DUSP6* in HEK cells (Supplemental Figure 4).

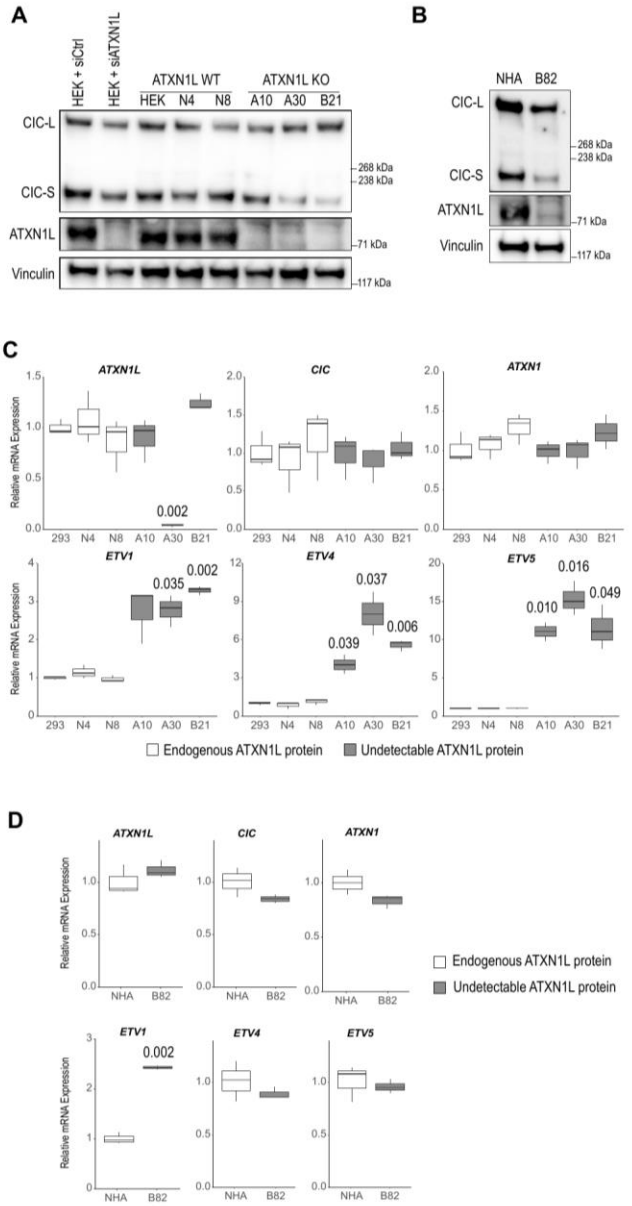

Figure 3.2 – *ATXN1L*^{KO} cell lines show derepression of CIC target genes.

(A) Representative western blots of CIC and ATXN1L expression in three *ATXN1L*^{WT} (HEK, N4, N8) and three *ATXN1L*^{KO} (A10, A30, B21) HEK-derived cell lines generated using CRISPR/Cas9. HEK cells were also treated with a "scrambled" non-targeting siRNA (siCtrl) and an ATXN1L siRNA (siATXN1L) to confirm antibody specificity. Vinculin was used as a loading control. (B) Representative western blots showing CIC and ATXN1L expression in the parental NHA and one *ATXN1L*^{KO} (B82) NHA-derived cell line using CRISPR/Cas9. Vinculin was used as a loading control. (C) Tukey boxplots showing relative mRNA expression levels of *ATXN1L, CIC, ATXN1* and the known CIC target genes *ETV1/4/5* in HEK *ATXN1L*^{WT} (HEK, N4, N8) and *ATXN1L*^{KO} (A10, A30, B21) cell lines. Data were collected from 3 independent experiments and p-values were calculated using the two-tailed independent Student's t-test. (D) Tukey boxplots showing relative mRNA expression levels of *ATXN1L, CIC, ATXN1* and the known CIC target genes *ETV1/4/5* in parental NHA and *ATXN1L*^{KO} (B82) NHA cell lines. Data were collected from 3 independent experiments and p-values were calculated using the two-tailed independent Student's t-test.

3.2.3 Transcriptomic analysis of *ATXN1L*^{KO} and *CIC*^{KO} isogenic cell lines result in convergence on activation of the MAPK pathway

To further investigate the reciprocal relationship between CIC and ATXN1L on a transcriptomic level, differential expression analysis (DEA) comparing *CIC*^{KO} or *ATXN1L*^{KO} cell lines with *CIC*^{WT}/*ATXN1L*^{WT} cell lines was performed using Affymetrix gene expression microarray data. Genes that were identified to be differentially expressed (DE) in *ATXN1L*^{KO} HEK (n=619) (Supplemental Table 2A) were compared to DE genes previously identified in *CIC*^{KO} HEK cell lines (n=583) (Supplemental Table 2B) [28]. A total of 110 genes were found to be DE in both contexts (Figure 3.3A and Supplemental Table 2C) including confirmed (*ETV1/4/5, DUSP6, SPRY4*) and putative (*SCN9A, LPAR6, ENPP2, EDIL3, COL2A1*) targets of CIC transcriptional regulation [28]. Similarly, comparison of DE genes identified in *ATXN1L*^{KO} NHA cells (n=914) (Supplemental Table 3A) and *CIC*^{KO} NHA cell lines (n=1163) (Supplemental Table 3B) yielded 299 shared DE genes (Figure 3.3B and Supplemental Table 3C). *SHC3* was the only confirmed CIC target gene found to be DE in both NHA *CIC*^{KO} and *ATXN1L*^{KO} cell lines[28]. Surprisingly, several previously described CIC target genes that were found to be DE in *CIC*^{KO} NHA cells (*ETV1/4/5, DUSP6, SPRY4, GPR3*) were not found to be DE in NHA *ATXN1L*^{KO} cells which may be due to compensation by ATXN1 [28, 30, 100], or to regulation by additional regulatory networks independent of ATXN1/ATXN1L. Regardless, the large number of shared DE genes identified in our *ATXN1L*^{KO} and *CIC*^{KO} NHA cell lines suggests that the relationship between CIC and ATXN1L, in this cellular context, may still be important on a global transcriptomic level.

Lastly, DE genes identified in our HEK and NHA *ATXN1L*^{KO} cell lines were compared to DE genes identified in Type I LGGs (IDH mutated, 1p19q-codeleted) [28] with truncating or nonsense *CIC* mutations (Type I LGG$^{CIC\text{-}Mut}$) (n=703, Supplemental Table 4A, FDR < 5%), a relevant tumour context. 27 DE genes (p = 0.32) were shared with the HEK dataset, including multiple confirmed and putative CIC target genes (*ETV1/4/5*, *DUSP6*, *SPRY4*, *EDIL3*, *ENPP2*, *SCN9A*) [28] (Supplemental Table 4B), and 32 DE genes (p = 0.79) were shared with the NHA dataset, of which, *SHC3* was the only confirmed CIC target gene[28] (Supplemental Table 4C). Gene set enrichment analysis (GSEA) of genes identified as upregulated upon loss of *CIC* or *ATXN1L* in all three contexts (HEK, NHA, LGG) converged upon gene signatures indicative of MAPK pathway activation (Figure 3.3C-D, and Supplemental Table 5C). Relative mRNA transcript levels of CIC target genes downstream of MAPK activation showed significant upregulation in our HEK (*DUSP6*, *SPRY4*, *SPRED2*, *PTPN9*, *SHC3*) and NHA (*SPRY4*, *SHC3*, *SPRED1*) *ATXN1L*^{KO} cell lines, while protein expression (ETV4, DUSP6, SPRY4, PTPN9, pMEK, pERK) was variable (Supplemental Figure 5).

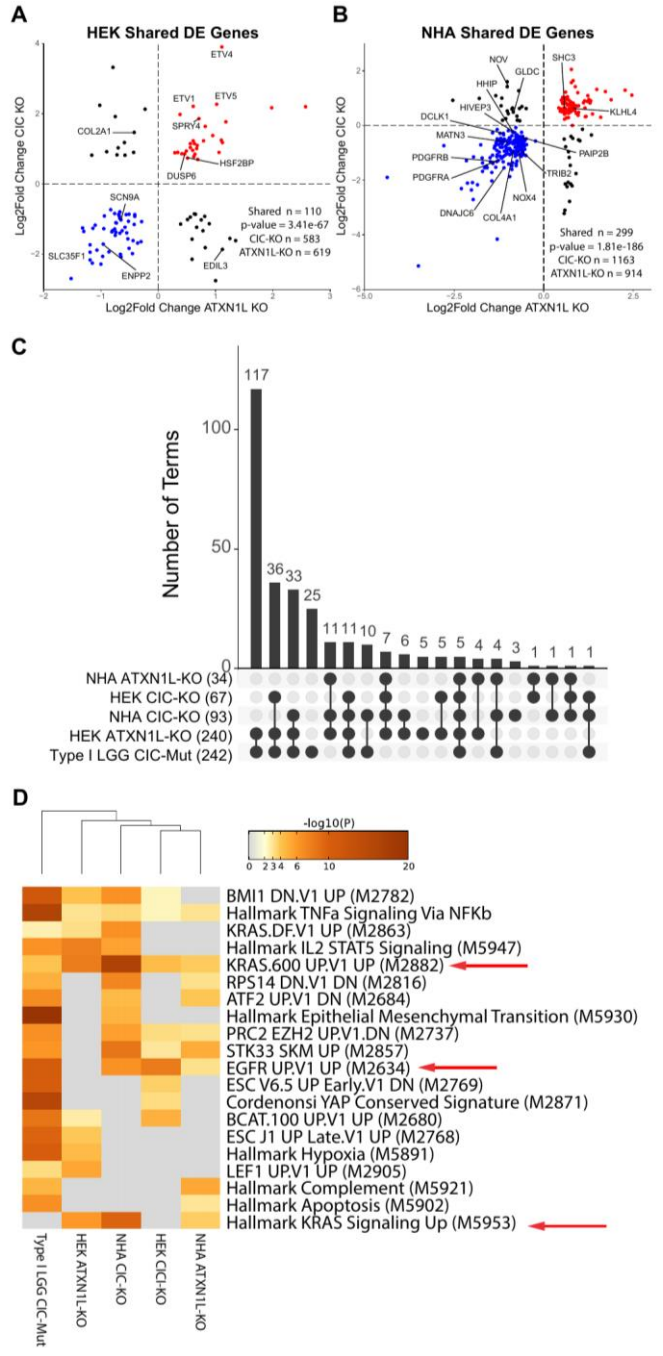

Figure 3.3 – Loss of CIC or ATXN1L dysregulate similar genes and gene sets *in vitro*.
(A) Scatter plot of shared DE genes identified in HEK *ATXN1L*^{KO} (x-axis) and HEK *CIC*^{KO} (y-axis) (Supplemental Table 2C). Labeled genes are genes also found to be DE in TCGA Type I LGGs harbouring CIC truncating mutations. (B) Scatter plot of shared DE genes identified in NHA *ATXN1L*^{KO} (x-axis) and NHA *CIC*^{KO} (y-axis) (Supplemental Table 3C). Labeled genes are genes also found to be DE in TCGA Type I LGGs harbouring CIC truncating mutations. p-values (A/B) were calculated using Fisher's exact test. (C) UpSet plot showing intersections of terms enriched for in upregulated DE genes identified in NHA *CIC*^{KO}, NHA *ATXN1L*^{KO}, HEK *CIC*^{KO}, HEK *ATXN1L*^{KO} and TCGA Type I LGGs with *CIC* truncating mutations (Supplemental Table 5C). Analysis was performed using GO biological

processes terms, Hallmark Gene Sets, and Oncogenic signatures. (D) Heat map showing the top 20 enriched terms for upregulated DE genes identified in NHA *CIC*^{KO}, NHA *ATXN1L*^{KO}, HEK *CIC*^{KO}, HEK *ATXN1L*^{KO} and TCGA LGG Type I with *CIC* truncating mutations using Hallmark gene sets and Oncogenic signatures. Term IDs from MSigDB are shown. Terms related to a MAPK activation signature are denoted with a red arrow.

3.2.4 Deletions in *ATXN1/ATXN1L* or *CIC* lead to convergent transcriptomic changes.

CIC aberrations have recently been associated with poor prognosis in multiple cancer types such as Type I LGG [28, 30], pancreatic [29], lung [31], sarcoma [32, 36], hepatocellular carcinoma [33], prostate adenocarcinoma (PRAD) [96, 100], and stomach adenocarcinoma (STAD) [101]. *CIC* alterations in these cancers have been correlated with increased metastatic potential, treatment resistance, and invasiveness. Based on our *in vitro* CIC-ATXN1L observations, we hypothesized that aberrations in *ATXN1L* may be exploited by multiple cancer types resulting in biological consequences similar to aberrations in *CIC*. Analysis of TCGA identified a high frequency of *ATXN1L* copy number variations (CNVs) including heterozygous and homozygous deletions observed in the PRAD (173/492), LGG (12/283), and STAD (69/287) cohorts.

To explore the relationship between CIC and ATXN1L alterations in primary cancer settings, copy number and gene expression data were obtained from TCGA and differential expression analyses between samples with copy number loss of *CIC* or *ATXN1/ATXN1L* and samples with intact *CIC* and *ATXN1L* were performed. Table 3.1 describes the *CIC*, *ATXN1*, and *ATXN1L* status of each cohort used for DEA.

Table 3.1 – TCGA analysis cohorts

Label	Cohort	*ATXN1* Status	*ATXN1L* Status	*CIC* Status	
Type I LGG$^{CIC\text{-Mut}}$	Low Grade Glioma	Wildtype	Wildtype	Truncating and Nonsense Mutations	*
Type I LGG$^{CIC\text{-WT}}$	Low Grade Glioma	Wildtype	Wildtype	Wildtype	*
Type II LGG$^{CIC\text{-Del}}$	Low Grade Glioma	Wildtype	Wildtype	Homozygous and Heterozygous Deletions	
Type II LGG$^{ATXN1/ATXN1L\text{-Del}}$	Low Grade Glioma	Homozygous and Heterozygous Deletions	Homozygous and Heterozygous Deletions	Wildtype	**
Type II LGG^{WT}	Low Grade Glioma	Wildtype	Wildtype	Wildtype	
PRAD$^{CIC\text{-Del}}$	Prostate Adenocarcinoma	Wildtype	Wildtype	Homozygous and Heterozygous Deletions	
PRAD$^{ATXN1L\text{-Del}}$	Prostate Adenocarcinoma	Wildtype	Homozygous and Heterozygous Deletions	Wildtype	

PRAD^{WT}	Prostate Adenocarcinoma	Wildtype	Wildtype	Wildtype	
STAD$^{CIC\text{-Del}}$	Stomach Adenocarcinoma	Wildtype	Wildtype	Homozygous and Heterozygous Deletions	
STAD$^{ATXN1\text{-Del}}$	Stomach Adenocarcinoma	Homozygous and Heterozygous Deletions	Wildtype	Wildtype	
STAD$^{ATXN1L\text{-Del}}$	Stomach Adenocarcinoma	Wildtype	Homozygous and Heterozygous Deletions	Wildtype	
STAD$^{ATXN1/ATXN1L\text{-Del}}$	Stomach Adenocarcinoma	Homozygous and Heterozygous Deletions	Homozygous and Heterozygous Deletions	Wildtype	***
STAD^{WT}	Stomach Adenocarcinoma	Wildtype	Wildtype	Wildtype	
*CIC Status is for the remaining allele and exists in a hemizygous state due to the 1p19q co-deletion					
**Homozygous/Heterozygous deletions in *ATXN1* or *ATXN1L*					
***Homozygous deletions in *ATXN1* or *ATXN1L*,or Heterozygous deletions in *ATXN1* and *ATXN1L*					

DEA comparing PRAD$^{CIC\text{-}Del}$ (n=34) and PRAD^{WT} (n=190) identified 842 DE genes (Supplemental Table 6A, FDR < 5%, fold change > 1.5). Samples with homozygous deletions of *CIC* were included in this analysis regardless of *ATXN1L* status due to the complete loss of *CIC*. Similarly, DEA comparing PRAD$^{ATXN1L\text{-}Del}$ (n=90) and PRAD^{WT} samples identified 811 DE genes (Supplemental Table 6B, FDR < 5%, fold change > 1.5). A total of 232 genes were shared between the two analyses (Figure 3.4A/Supplemental Table 6C).

Prior to DEA of the LGG cohort, tumours were stratified into Type I (IDH mutated, 1p19q-codeleted), Type II (IDH mutated, 1p19q-retained), and Type III (IDH wildtype) tumours based on canonical genomic signatures [4, 11]. DEA investigating samples with *ATXN1L* deletions was not performed in Type I LGGs due to the lack of a normal comparator caused by 1p19q co-deletion (loss or aberration in at least one allele of *CIC* in every sample). However, *ATXN1* (n=7) and *ATXN1L* (n=4) deletions were identified at similar rates and found to be mutually exclusive in Type II LGG, suggesting that, in this context, loss of either gene may result in CIC instability. Therefore, DEA was performed comparing Type II-LGG$^{ATXN1/ATXN1L\text{-}Del}$ (n=11) and Type II LGG^{WT} (n=88) samples which identified 611 DE genes (Supplemental Table 7A, FDR < 5%). Similarly, DEA was performed comparing Type II-LGG$^{CIC\text{-}Del}$ (n=30) and Type II LGG^{WT} samples which identified 1538 DE genes (Supplemental Table 7B, FDR < 5%). A total of 132 genes were shared between the two analyses (Figure 3.4B/Supplemental Table 7C).

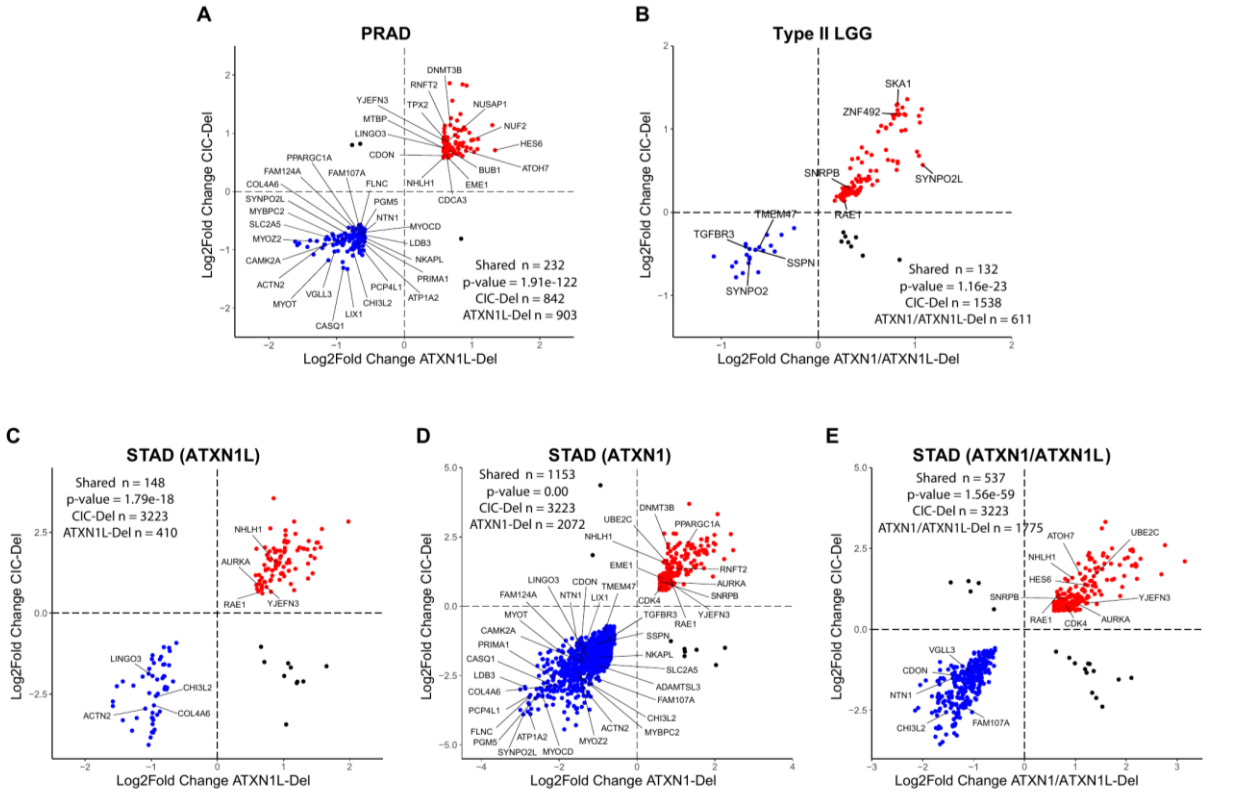

Figure 3.4 – Differentially expressed genes identified in tumours with *ATXN1* and/or *ATXN1L* aberrations and *CIC* aberrations show overlap and directional concordance.
(A) Scatter plot of shared DE genes identified in PRAD$^{\text{ATXN1L-Del}}$ (x-axis) and PRAD$^{\text{CIC-Del}}$ samples (y-axis) (Supplemental Table 6C). (B) Scatter plot of shared DE genes identified in Type II-LGG$^{\text{ATXN1/ATXN1L-Del}}$ (x-axis) and Type II-LGG$^{\text{CIC-Del}}$ (y-axis) (Supplemental Table 7C). (C) Scatter plot of shared DE genes identified in STAD$^{\text{ATXN1L-Del}}$ (x-axis) and STAD$^{\text{CIC-Del}}$ (y-axis) (Supplemental Table 8E). (D) Scatter plot of shared DE genes identified in STADA$^{\text{TXN1-Del}}$ (x-axis) and STAD$^{\text{CIC-Del}}$ (y-axis) (Supplemental Table 8F). (E) Scatter plot of shared DE genes identified in STAD$^{\text{ATXN1/ATXN1L-Del}}$ (x-axis) and STAD$^{\text{CIC-Del}}$ (y-axis) (Supplemental Table 8G). *Labeled genes in each scatter plot (A-E), were found to be DE and shared in at least 2/3 cancer contexts. (Table 3.2). p-values were calculated using Fisher's exact test.

Lastly, deletions in *ATXN1* and *ATXN1*L were identified in 118/287 samples in the TCGA STAD cohort but were not found to be mutually exclusive with *CIC* deletions (49/287). DEA comparing STAD$^{\textit{CIC-Del}}$ (n=10) and STAD$^{\text{WT}}$ (n=126) identified 3223 DE genes, including the canonical CIC target genes *ETV4/5* (Supplemental Table 8A, FDR < 5% and fold change > 1.5). Due to the comparable frequency and large number of *ATXN1* (n=49/287) and *ATXN1L* (n=69/287) deletions in the STAD cohort, three independent DEAs were performed comparing STAD$^{\textit{ATXN1-Del}}$ (n=20), STAD$^{\textit{ATXN1L-Del}}$ (n=22), or STAD$^{\textit{ATXN1/ATXN1L-Del}}$ (n=15) and STAD$^{\text{WT}}$ to investigate the differences and similarities between ATXN1 and ATXN1L function within the context of STADs. DEA of STAD$^{\textit{ATXN1-Del}}$, STAD$^{\textit{ATXN1L-Del}}$, and STAD$^{\textit{ATXN1/ATXN1L-Del}}$ identified 2072, 410, and 1557 DE genes, respectively (Supplemental Tables 8B, 8C, 8D, FDR < 5%, fold change > 1.5). Surprisingly, differential expression of CIC target genes (*ETV1/4/5*) was not

identified in these analyses. Comparisons between $STAD^{CIC\text{-}Del}$ versus $STAD^{ATXN1\text{-}Del}$, $STAD^{ATXN1L\text{-}Del}$, and $STAD^{ATXN1/ATXN1L\text{-}Del}$ yielded 1153, 148, and 537 shared DE genes, respectively (Figure 3.4C-E/Supplemental Tables 8E, 8F, 8G). Shared DE genes identified in all three cohorts (PRAD, LGG, STAD) displayed a high degree of directional concordance.

3.2.5 Deletions in ATXN1/ATXN1L or CIC lead to convergent dysregulation of cellular processes and gene set

Using multi-list GSEAs, we observed a high degree of intersection for terms enriched in genes found to be upregulated in tumours with *CIC* loss and tumours with *ATXN1/ATXN1L* loss (Figure 3.5A-C). In the PRAD and Type II LGG cohorts, these terms converged upon processes associated with nuclear division, DNA replication, and progression through the mitotic cycle (Supplemental Figure 6A, 6B/Supplemental Table 9A, 9B). Similarly, terms enriched for genes identified as upregulated in the STAD cohort related to upregulation of myc and mTOR (Supplemental Figure 6C/Supplemental Table 9C). GSEA of upregulated DE genes identified in all three cohorts (in conjunction), yielded terms related to cellular mitosis, DNA replication, and activation of E2F, myc and mTOR (Figure 3.5D-E/Supplemental Table 9D). Upregulation of polycomb repressive complex (PRC2) targets and terms related to DNA conformation were also enriched.

Across the three TCGA cohorts investigated, 49 shared DE genes were seen in at least two of the three cohorts analysed (Table 3.2). Amongst these 49 genes, we observed upregulation in several genes related to nuclear division and cytokinesis including *AURKA, CDK4, NUSAP1, BUB1, TPX2, NUF2* and *CDCA3*. Of these 49 shared genes, the majority (45, 92%) also showed directional concordance between cohorts. Gene enrichment analysis of upregulated shared DE genes once again revealed terms related to mitotic cell cycle progression/nuclear division, hallmark E2F targets and regulation of chromatin conformation (Figure 3.5F/Supplemental Table 10).

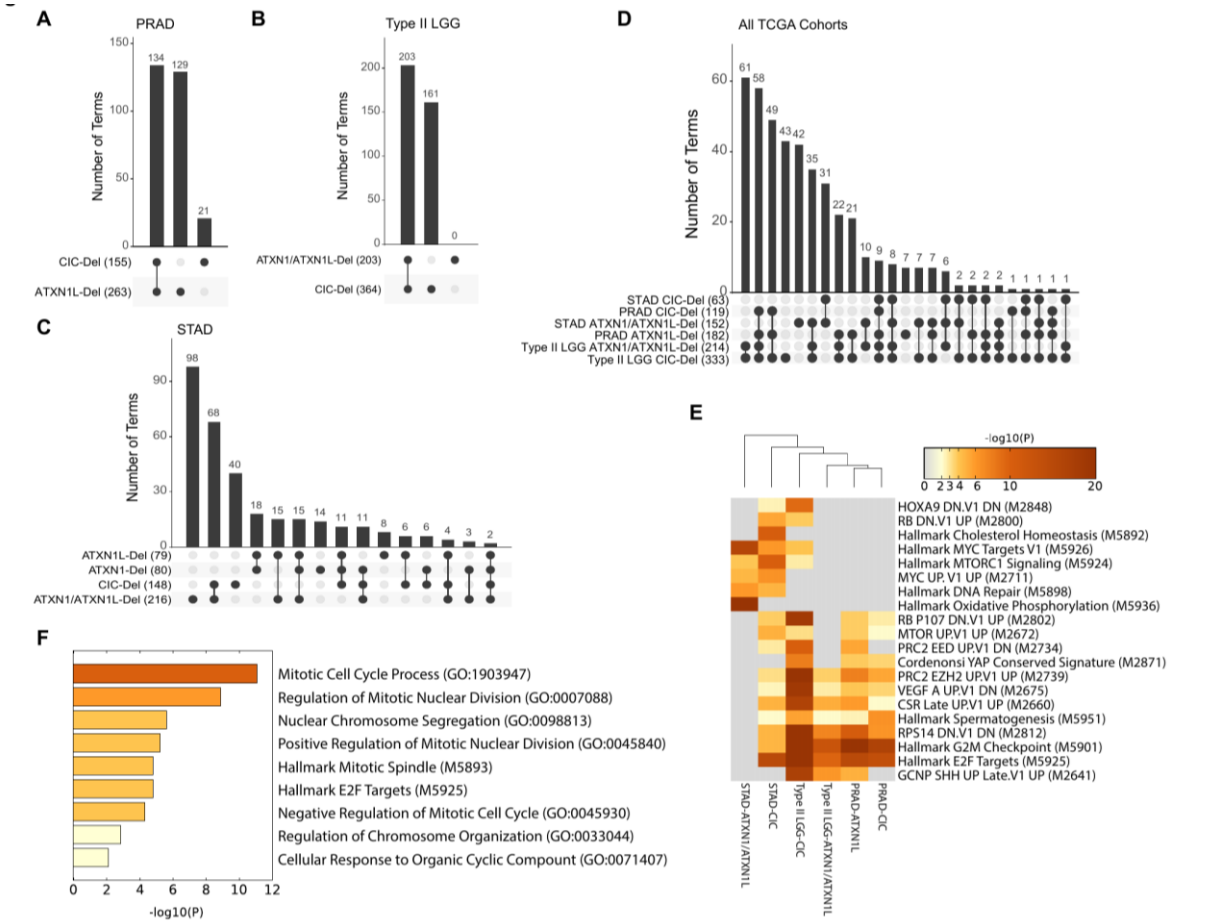

Figure 3.5 –Tumours with *ATXN1* and/or *ATXN1L* aberrations and *CIC* aberrations display overlap in gene enrichment signatures.
(A) UpSet plot showing intersections of terms enriched in upregulated DE genes identified in Type II-LGG$^{ATXN1/ATXN1L\text{-}Del}$ and Type II-LGG$^{CIC\text{-}Del}$ (Supplemental Table 9A). (B) UpSet plot showing intersections of terms enriched in upregulated genes identified in PRAD$^{ATXN1L\text{-}Del}$ and PRAD$^{CIC\text{-}Del}$ (Supplemental Table 9B). (C) UpSet plot showing intersections of terms enriched in upregulated genes identified in STAD$^{ATXN1L\text{-}Del}$, STAD$^{ATXN1\text{-}Del}$, STAD$^{ATXN1/ATXN1L\text{-}Del}$, and STAD$^{CIC\text{-}Del}$ (Supplemental Table 9C). *Gene set enrichment analyses for (A), (B), and (C) were performed using GO biological processes terms, hallmark gene sets, and oncogenic signatures. (D) UpSet plot showing intersections of GO biological processes terms enriched in upregulated genes identified in all three TCGA cohorts analyzed with *ATXN1* and/or *ATXN1L*, or *CIC* loss (Supplemental Table 9D). (E) Heat map showing the top 20 enriched terms for upregulated DE genes identified in all three TCGA cohorts analyzed with *ATXN1* and/or *ATXN1L*, or *CIC* loss using only hallmark gene sets and oncogenic signatures. Term IDs from MSigDB are shown. (F) Terms enriched for upregulated shared genes that were identified in at least 2/3 cohorts analyzed (Supplemental Table 10). Terms from GO Biological Process terms, Hallmark gene sets and Oncogenic signatures were used.

Table 3.2 – Shared DE Genes across TCGA cohorts analysed

		Log2Fold Change									
		Type II LGG		PRAD		STAD				Cohort Frequency	
Gene	Entrez.ID	CIC-Del	ATXN1/ATXN1L-Del	CIC-Del	ATXN1L-Del	CIC-Del	ATXN1-Del	ATXN1L-Del	ATXN1/ATXN1L-Del	Up	Down
ACTN2	88	-	-	-0.91	-1.18	-2.95	-1.38	-1.09	-	0	2
ADAMTSL3	57188	-0.78	-0.85	-	-	-2.13	-1	-	-	0	2
ATOH7	220202	-	-	0.7	0.91	1.72	-	-	1.09	2	0
ATP1A2	477	-	-	-0.83	-0.64	-3.8	-2.81	-	-	0	2
AURKA	6790	1.04	0.65	-	-	0.87	0.75	0.67	1.07	2	0
BUB1	699	1.17	0.83	0.71	0.66	-	-	-	-	2	0
CAMK2A	815	-	-	-0.8	-0.86	-2.05	-1.33	-	-	0	2
CASQ1	844	-	-	-1.31	-0.9	-2.76	-2.3	-	-	0	2
CDCA3	83461	0.59	0.82	0.63	0.6	-	-	-	-	2	0
CDK4	1019	0.61	0.82	-	-	0.73	0.64	-	0.82	2	0
CDON	50937	-	-	0.65	0.6	-1.42	-1.55	-	-1.39	1	1
CHI3L2	1117	-	-	-0.99	-0.76	-2.56	-1.47	-0.93	-1.39	0	2
COL4A6	1288	-0.65	-0.89	-0.68	-0.76	-2.85	-2.11	-0.96	-	0	3
DNMT3B	1789	-	-	1.14	0.68	2.11	0.8	-	-	2	0
EME1	146956	-	-	0.58	0.65	1.14	0.69	-	-	2	0
FAM107A	11170	-	-	-0.58	-0.67	-2.41	-1.4		-1.16	0	2
FAM124A	220108	-	-	-0.71	-0.66	-1.92	-1.36	-	-	0	2
FLNC	2318	-	-	-0.66	-0.66	-3.28	-2.77	-	-	0	2
HES6	55502	-	-	0.71	1.34	1.36			1.24	2	0
LDB3	11155	-	-	-0.73	-0.64	-2.91	-2.88	-	-	0	2
LINGO3	645191	-	-	0.75	0.59	-1.94	-1.24	-0.98	-	1	1
LIX1	167410	-	-	-1.33	-0.84	-1.99	-1.5	-	-	0	2
MTBP	27085	0.63	0.72	0.74	0.59	-	-	-	-	2	0
MYBPC2	4606	-	-	-0.77	-0.97	-2.51	-1.47	-	-	0	2
MYOCD	93649	-	-	-0.7	-0.61	-3.21	-2.43	-	-	0	2
MYOT	9499	-	-	-1.18	-1.12	-1.59	-2.02	-	-	0	2
MYOZ2	51778	-	-	-0.85	-1.29	-2.33	-1.5	-	-	0	2
NHLH1	4807	-	-	0.58	0.58	1.59	0.68	0.88	0.94	2	0
NKAPL	222698	-	-	-0.77	-0.62	-1.97	-1.02	-	-	0	2
NTN1	9423	-	-	-0.65	-0.58	-1.51	-1.51	-	-1.41	0	2
NUF2	83540	1.17	0.77	0.89	1.02	-	-	-	-	2	0
NUSAP1	51203	1.17	0.9	0.85	0.63	-	-	-	-	2	0
PCP4L1	654790	-	-	-0.86	-0.7	-3.2	-2.74	-	-	0	2
PGM5	5239	-	-	-0.74	-0.65	-3.19	-2.54	-	-	0	2
PPARGC1A	10891	-	-	-0.64	-0.7	2.28	1.32	-	-	1	1

PRIMA1	145270	-	-	-0.84	-0.59	-2.71	-2.29	-	-	0	2
RAE1	8480	0.14	0.27	-	-	1.00	0.72	0.34	0.86	2	0
RNFT2	84900	-	-	1.13	0.6	1.37	0.85	-	-	2	0
SLC2A5	6518	-	-	-0.78	-1.14	-2.1	-0.77	-	-	0	2
SNRPB	6628	0.32	0.21	-	-	0.82	0.56	-	0.88	2	0
SSPN	8082	-0.45	-0.65	-	-	-1.47	-0.92	-	-	0	2
SYNPO2	171024	-0.56	-0.71	-0.60	-0.54	-3.90	-2.92	-	-	1	2
SYNPO2L	79933	0.57	1.08	-0.72	-0.87	-	-	-	-	1	1
TGFBR3	7049	-0.44	-0.71	-	-	-1.14	-1.13	-	-	0	2
TMEM47	83604	-0.42	-0.61	-	-	-1.37	-1.09	-	-	0	2
TPX2	22974	1.29	0.81	0.87	0.62	-	-	-	-	2	0
UBE2C	11065	1.23	0.82	-	-	1.5	0.82	-	1.32	2	0
VGLL3	389136	-	-	-1.03	-1.03	-1.34	-	-	-1.05	0	2
YJEFN3	374887	-	-	0.87	0.6	0.81	0.88	0.74	1.23	2	0

3.2.6 CIC-ATXN1L interaction facilitates CIC-DNA binding

In addition to promoting CIC protein stability, ATXN1L may also facilitate the promoter binding efficiency of CIC. To assess this, targeted chromatin immunoprecipitation followed by quantitative polymerase chain reaction (ChIP-qPCR) was performed in parental HEK, *CIC*^{KO} (D10) and *ATXN1L*^{KO} (A30) cells. Enrichment of CIC binding to several sites within the promoter regions of *ETV4*, *DUSP6* and *SPRY4* were found to be significantly reduced in *ATXN1L*^{KO} (HEK-A30) cells compared to the parental HEK cell line (Supplemental Figure 7). ChIP-PCR was also performed using a FLAG-tagged, V41G CIC-S mutant (CIC-S^{V41G}) which lacks the ability to interact with ATXN1L (Figure 3.6A) [102]. Enrichment of CIC-S^{V41G} binding to the promoter regions of CIC target genes (*ETV4*, *DUSP6*, *SPRY4*) was comparable to the enrichment observed in the *ATXN1L*^{KO} cell line A30 (Figure 3.6B), further indicating that interaction with ATXN1L contributes to CIC's binding to the promoter regions of target genes. Therefore, de-repression of CIC target genes observed in *ATXN1L*^{KO} cells, described above, may be attributed to a decrease in CIC binding to the promoter regions of these genes.

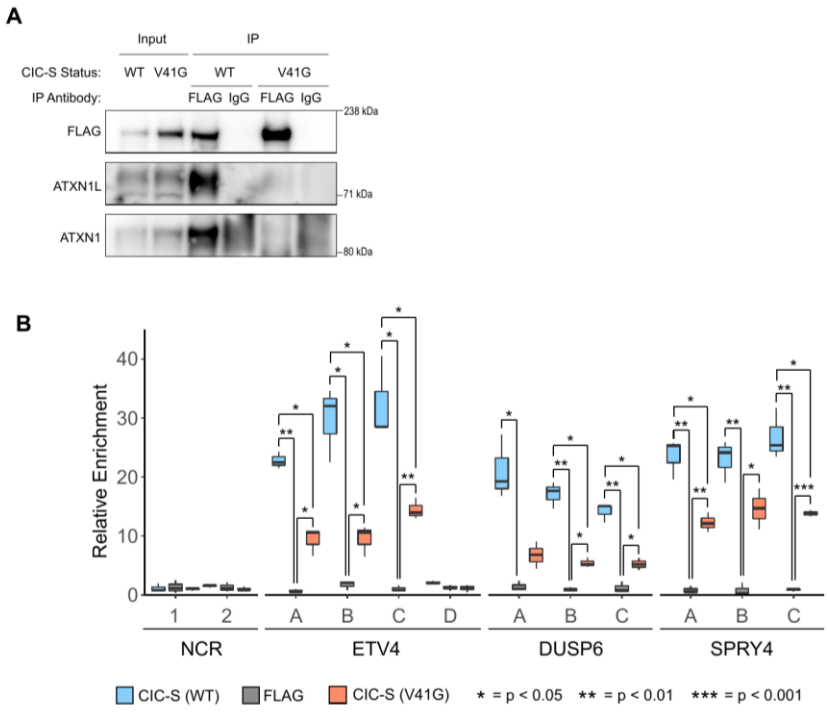

Gene	Site	P-value WT	FLAG	V41G
ETV4	A	0.001		0.025
	B	0.014		
	C	0.017		0.037
	D	0.039		
DUSP6	A	0.016		0.006
	B	0.049		
	C	N.S		N.S
SPRY4	A	N.S		
	B	0.025		N.S
	C	N.S		
NCR1		0.006		0.013
NCR2		0.013		
		0.007		0.038
		0.015		
		0.008		0.036
		0.008		
		0.009		0.022
		N.S		
		0.009		< 0.001
		0.036		
		N.S		N.S
		N.S		
		N.S		N.S
		N.S		

Figure 3.6 – ATXN1L interaction with CIC facilitates CIC binding to promoter regions of CIC target genes. (A) FLAG-tagged Immunoprecipitation of wildtype CIC-S (WT) and V41G mutant CIC-S (V41G) showing lack of both ATXN1L and ATXN1 co-IP with the mutant form of CIC. An IgG IP was used as a control. (B) Tukey boxplots showing enrichment of FLAG-tagged wildtype CIC (WT) and V41G mutant CIC (V41G) binding to promoter regions of CIC target genes (*ETV4*, *DUSP6*, *SPRY4*) relative to a negative control region (NCR1)

following FLAG-tagged CIC ChIP-qPCR in *CIC*^{KO} HEK cells stably expressing wildtype CIC-S (WT), FLAG (FLAG), and V41G mutant CIC-S (V41G). Data were collected over 3 independent experiments and p-values were calculated using the two-tailed independent Student's t-test. p-values are displayed in the table to the right.

3.3 Discussion

This study is the first to have explored, in depth, the functional relationship between ATXN1L and CIC at the proteomic and transcriptomic level in isogenic cell lines and several distinct primary cancer settings. Functional *in vitro* studies and transcriptomic profiling of *CIC*^{KO} and *ATXN1L*^{KO} isogenic cell lines show that the post-translational stability and transcriptionally repressive activity of CIC relies heavily on its physical interaction with ATXN1L. Upregulation of multiple CIC target genes downstream of the MAPK signaling cascade were observed in our *ATXN1L*^{KO} transcriptomic analyses, indicating that ATXN1L may be an important mediator of CIC in feedback loops responsible for regulating MAPK signalling [28, 29]. The importance of the CIC-ATXN1-ATXN1L axis in cancer is becoming increasingly evident as one that can be exploited by RTK-driven cancers to subvert inhibition of upstream druggable targets such as EGFR and MEK, as already seen in pancreatic cancer [29, 35]. Establishing the status of this axis may become a powerful prognostic indicator in a multitude of RTK driven cancers. Although the exact mechanism through which ATXN1L stabilizes CIC is unknown, our results indicate that proteasomal degradation of CIC, in the absence of ATXN1L, may be a potential candidate of targeted therapies aimed at increasing CIC stability and repressive function.

Further highlighting the context-dependent relationship and interplay between CIC, ATXN1, and ATXN1L, DEA and GSEA of three TCGA cohorts (PRAD, Type II LGG, and STAD) also showed that tumours with loss of *ATXN1* and/or *ATXN1L* demonstrated transcriptomic changes similar to those found in tumours with *CIC* loss. In the PRAD cohort, *ATXN1L* deletions were observed at a much higher frequency compared to *ATXN1* deletions, indicating the possibility that, in this context, ATXN1L may be the primary interactor of CIC. Conversely, *ATXN1* and *ATXN1L* deletions were seen at similar frequencies in both Type II LGG and STAD suggesting that, in these contexts, both proteins may play equally important roles in regulating CIC function. Notably, hemizygous loss of *ATXN1* or *ATXN1L* in STAD did not appear sufficient to dysregulate CIC function, while homozygous loss of *ATXN1* or *ATXN1L*, or hemizygous loss of both *ATXN1* and *ATXN1L* did have more important effects, which may indicate that in the context of STAD, a higher threshold of *ATXN1/ATXN1L* loss is required for CIC dysfunction. The distinct differences in the relationship between CIC and ATXN1/ATXN1L

between these three cohorts may indicate that the CIC-ATXN1-ATXN1L axis may be more complex than previously appreciated and greatly dependent on cellular context.

Although our TCGA analyses of Type II LGGs, PRAD and STAD samples did not yield gene signatures indicative of MAPK activation as expected [28, 29, 35, 52], our data instead suggests that aberrations in the CIC-ATXN1-ATXN1L axis may contribute to cellular growth and proliferation through the upregulation of myc and E2F targets. The E2F transcription factor family has been implicated in promoting cell cycle transitions and driving aberrant cellular proliferation in multiple contexts including prostate cancer and gliomas [103-107]. Aberrant activation of myc has also been described in up to 40% of gastric cancers and is associated with poor prognosis due to promotion of a cancer stem like state [101, 108, 109]. GSEA also identified many terms related to cellular division; including chromosome condensation and segregation, DNA replication, and G2/S phase transitions. Together, these gene signatures suggest that aberrations in the CIC-ATXN1-ATXN1L axis may highlight a subpopulation of E2F-dependent tumours that may be candidates for targeted treatment through the cyclin/Rb/E2F pathway [110, 111]. Terms related to upregulation of polycomb group (PRC1/PRC2) targets were also found to be enriched in all three cohorts. The polycomb group complexes are chromatin modifying complexes essential for embryonic development and stem cell self-renewal and thus are frequently dysregulated in multiple cancers [112, 113]. Several polycomb group target genes were found to be dysregulated in our differential expression analyses including several members of the HOX family (*HOXA3, HOXA4, HOXB3, HOXB9, HOXD10*) and the MT1 family (*MT1A, MT1E, MT1G, MT1H*) and members of the polycomb group complexes (*EZH2, CBX8*) [114].

Here, we have shown aberrations in *ATXN1/ATXN1L* or *CIC* in three distinct contexts are associated with gene signatures indicative of cellular growth and proliferation independent of the MAPK activation previously identified in many *CIC* inactivated contexts [28, 29, 31, 35, 52], which may indicate that CIC and ATXN1L act as regulators of cell cycle in a much broader context than previously appreciated. This study has expanded on the current knowledge of CIC and ATXN1/ATXN1L in cancer biology and highlighted the unique, context-specific, reciprocal relationship between CIC and ATXN1/ATXN1L. Further study into this interaction may provide insight into the mechanisms responsible for mediating the functional relationship between CIC and ATXN1/ATXN1L and further our understanding of the prognostic and therapeutic value of the CIC-ATXN1/ATXN1L axis.

Chapter 4: CIC and ATXN1L Interaction Forms a Post-Translational Functional and Reciprocal Relationship

4.1 Introduction

In the previous chapter, chapter 3, we revealed a reciprocal functional transcriptomic relationship between CIC and ATXN1L frequently exploited by cancer to dysregulate the cell cycle. In addition to these transcriptomic changes, we also observed a decrease in CIC protein which was not reflective of *CIC* mRNA expression in our *ATXN1L*^{KO} cell lines. While many studies have investigated the role of *CIC* loss of function mutations in cancer, far fewer studies have investigated the role that post-translational CIC dysregulation plays in promoting oncogenesis or cancer progression. In glioblastoma, post-translational CIC inactivation has been observed as a result of ERK phosphorylation and subsequent degradation through interaction with the E3-ligase PJA1 [57]. Conversely, post-translational dysregulation of CIC through loss of ATXN1L has been observed in pancreatic cancer and melanoma resulting in a treatment resistant phenotype [29].

ATXN1L is a member of the Ataxin protein family which has been shown to be a potent regulator of CIC function in both murine development and cancer [29, 54, 65]. Previous studies investigating murine development have indicated some level of functional redundancy between ATXN1L and its homologue ATXN1. However, these studies have also highlighted that loss of ATXN1L affected CIC function much more profoundly and robustly compared to loss of ATXN1, which is also consistent in cancer [65, 66]. Although several studies have consistently reported that the loss of ATXN1L results in the post-translational dysregulation of CIC stability and function, the exact mechanism responsible for this phenomenon remains unknown.

In this chapter, we explore the physical relationship between CIC and ATXN1L, and interrogate the mechanism responsible for CIC instability following the loss of ATXN1L. We uncover a reciprocal physical relationship between CIC and ATXN1L; and an ERK independent mechanism whereby the interaction between CIC and ATXN1L protects CIC from degradation by the E3-ligase TRIM25. Utilising both *in vitro* gene expression data from genetically modified cell lines and patient derived gene expression data from The Cancer Genome Atlas (TCGA), TRIM25 and CIC-ATXN1L were found to antagonistically regulate similar gene sets related to the cell cycle.

4.2 Results

4.2.1 Loss of ATXN1L promotes the proteasomal degradation of CIC

Several studies in human cell lines and mouse studies have reported decreased CIC protein expression following loss of ATXN1L [29, 54, 65]. In concordance with these studies, decreased CIC protein expression was observed in our *ATXN1L*^{KO} cell lines [54] which could be partially rescued to levels similar to the untreated parental cell line following treatment with MG132, an inhibitor of the 20S subunit of the proteasome (Figure 4.1A), or ectopic expression of a FLAG-tagged ATXN1L construct (Figure 4.1B). Inhibition of translation using cycloheximide also revealed a decrease in CIC protein half-life in *ATXN1L*^{KO} cells compared to *ATXN1L*^{WT} cells (Supplemental Figure 8). This decrease in CIC protein expression was found to be exclusive to ATXN1L loss and was not observed following siRNA knockdown of *ATXN1*, a homologue of *ATXN1L* (Figure 4.1C). Additionally, introduction of mutant FLAG-tagged *ATXN1L*-V485A, which is unable to interact with CIC [102] (Supplemental Figure 9A), also did not rescue CIC protein expression (Figure 4.1D). Density gradient fractionation of *ATXN1L*^{WT} and *ATXN1L*^{KO} cell lysates revealed an increase of CIC in higher molecular weight fractions that also contain SUG1, a proteasome subunit (Supplemental Figure 9B). Using immunoprecipitation, an increased accumulation of ubiquitin associated with CIC was also observed in *ATXN1L*^{KO} cells which have decreased CIC expression levels (Figure 4.1E, F). Similarly, using proximity ligation assay (PLA), interaction between CIC and ubiquitin was observed to increase following treatment with MG132 in *ATXN1L*^{KO} (Supplemental Figure 9C, D) or siRNA knockdown of *ATXN1L* in *ATXN1L*^{WT} cells (Figure 4.1G, H).

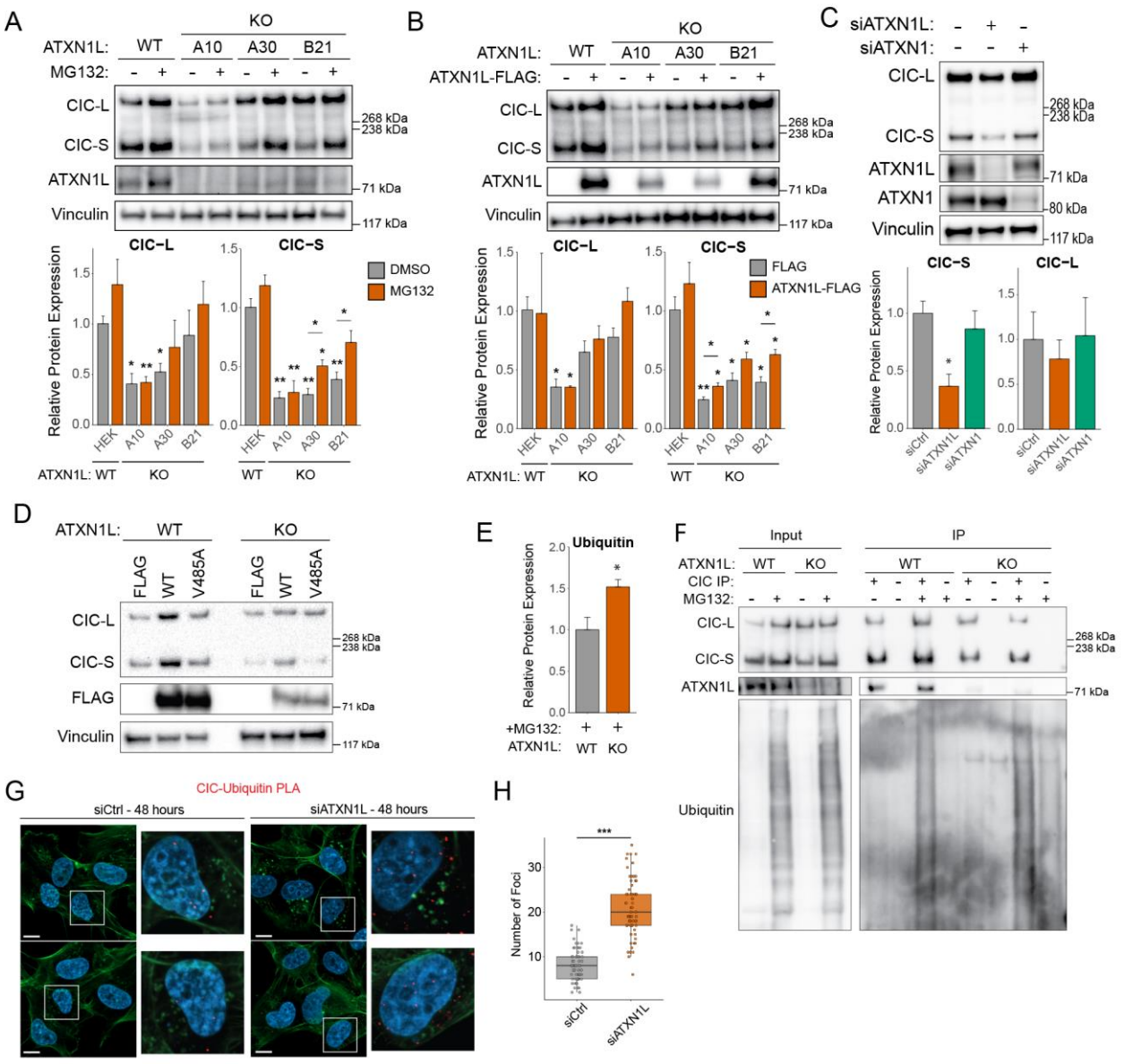

Figure 4.1 – Loss of ATXN1L results in CIC instability
(A) Representative Western blot of *ATXN1L*^{WT} (HEK) and *ATXN1L*^{KO} cell lines (A10, A30, B21) treated with MG132. DMSO used as negative control. Below: barplots showing quantification of CIC expression. (B) Representative Western blot of *ATXN1L*^{WT} (HEK) and *ATXN1L*^{KO} cell lines (A10, A30, B21) cell lines ectopically over-expressing FLAG-tagged ATXN1L. Below: barplots showing quantification of CIC expression. (C) Representative Western blot of siRNA knockdown of *ATXN1* and *ATXN1L* in NHA. Scrambled siRNA used as negative control. Below: barplots showing quantification of CIC expression. (D) Representative Western blot of *ATXN1L*^{WT} (HEK) and *ATXN1L*^{KO} cell lines (A30) ectopically over-expressing FLAG-tagged WT ATXN1L or mutant ATXN1L-V485A. (E) Barplots showing quantification of Ubiquitin Western blots normalized to CIC Western blots. (F) Representative Western blot of CIC immunoprecipitation in *ATXN1L*^{WT} (NHA) and *ATXN1L*^{KO} (B82) cell lines treated with MG132. DMSO used as negative control. (G) Immunofluorescence images of proximity ligation assay showing CIC-Ubiquitin interaction in *ATXN1L*^{WT} (NHA) and *ATXN1L*^{KO} (B82) cell lines treated with MG132. DMSO used as negative control. White bars denote 10µm. (H) Tukey boxplots showing quantification of number of foci/cell. (*) Western blot quantifications were collected from three independent experiments and were normalized to vinculin unless specified otherwise. Error bars represent one standard deviation. PLA quantifications were collected from 65 individual cells. p-values were calculated using the two-tailed independent Student's t-test. Statistically significant values are denoted (* = $p < 0.05$, ** = $p < 0.01$, *** = $p < 0.001$).

4.2.3 Loss of CIC leads to dysregulation of ATXN1L

Previous studies have investigated the effects of ATXN1/ATXN1L loss on CIC function without further probing the potential reciprocal effects of CIC loss on ATXN1/ATXN1L. Western blots of previously generated *CIC*^{KO} cell lines (HEK-D10, HOG-F11, NHA-A2) [28], revealed a decrease in the apparent molecular weight of ATXN1L compared to their respective *CIC*^{WT} parental cell lines (Figure 4.2A). *In silico* analysis of ATXN1L peptide sequence (Supplemental Figure 10) suggested that this decrease may be attributed to the loss of post-translational modification(s) (PTMs) such as phosphorylation [115]. Treatment of *CIC*^{WT} (HEK, NHA) cell lysates with lambda protein phosphatase (LPP), an indiscriminate phosphatase, resulted in a reduction of ATXN1L apparent molecular weight consistent with that observed in *CIC*^{KO} cell lines, suggesting that the absence of CIC results in loss or lack of ATXN1L phosphorylation (Figure 4.2B). Cellular fractionation also revealed that ATXN1L exhibited cytoplasmic localization in *CIC*^{KO} cells (HEK-D10, NHA-A2, HOG-F11) compared to their respective parental cell lines where ATXN1L was mostly localized to the nucleus (Figure 4.2C). This was also confirmed through immunofluorescence of endogenous ATXN1L (Figure 4.2D and Supplemental Figure 11A-B).

To further investigate the relationship between CIC loss and ATXN1L phosphorylation/localization, endogenous ATXN1L IP was performed following cellular fractionation of *CIC*^{WT} (HEK and NHA) and *CIC*^{KO} (HEK-D10 and NHA-A2) cells. Surprisingly, phosphorylated (Serine/Threonine) ATXN1L appeared to localize primarily to the cytoplasm (Figure 4.2E and Supplemental Figure 11C). Higher molecular weight ATXN1L was still detected in the nuclear fraction of *CIC*^{WT} cells which may indicate that the nuclear localization of ATXN1L is regulated by an alternative, unknown PTM. In addition to decreased molecular weight, CIC loss also appeared to affect the protein stability of ATXN1L. *CIC*^{KO} cells (HEK-D10 and NHA-A2) treated with the protein synthesis inhibitor cycloheximide (CHX) resulted in decreased ATXN1L protein expression at 24 hours post treatment, compared to the treated *CIC*^{WT} parental cell lines (Figure 4.2F and Supplemental Figure 11D).

Lastly, to investigate the potential downstream consequences of ATXN1L dysregulation resulting from CIC loss, the relative expression of the known ATXN1L target gene, HEY1 [75], was assessed and found to be derepressed in the NHA CICKO cell line A2, but significantly repressed in the HEK CICKO cell line D10 (Figure 4.2G). In contrast, HEY1 was derepressed in the *ATXN1L*^{KO} cell lines HEK-A30 and NHA-B82 (Supplemental Figure 11E). Reintroduction of

a FLAG-tagged short isoform of CIC (CIC-S) into *CIC*^{KO} cells (HEK-D10) rescued the decrease in ATXN1L molecular weight, restored some nuclear ATXN1L localization (Figure 4.2H), and returned *HEY1* expression to levels comparable to that observed in the parental HEK cell line (Figure 4.2I). Although the role of ATXN1L phosphorylation remains enigmatic, these results indicate that loss of CIC leads to the dysregulation of ATXN1L localization, phosphorylation/PTM status, and protein stability.

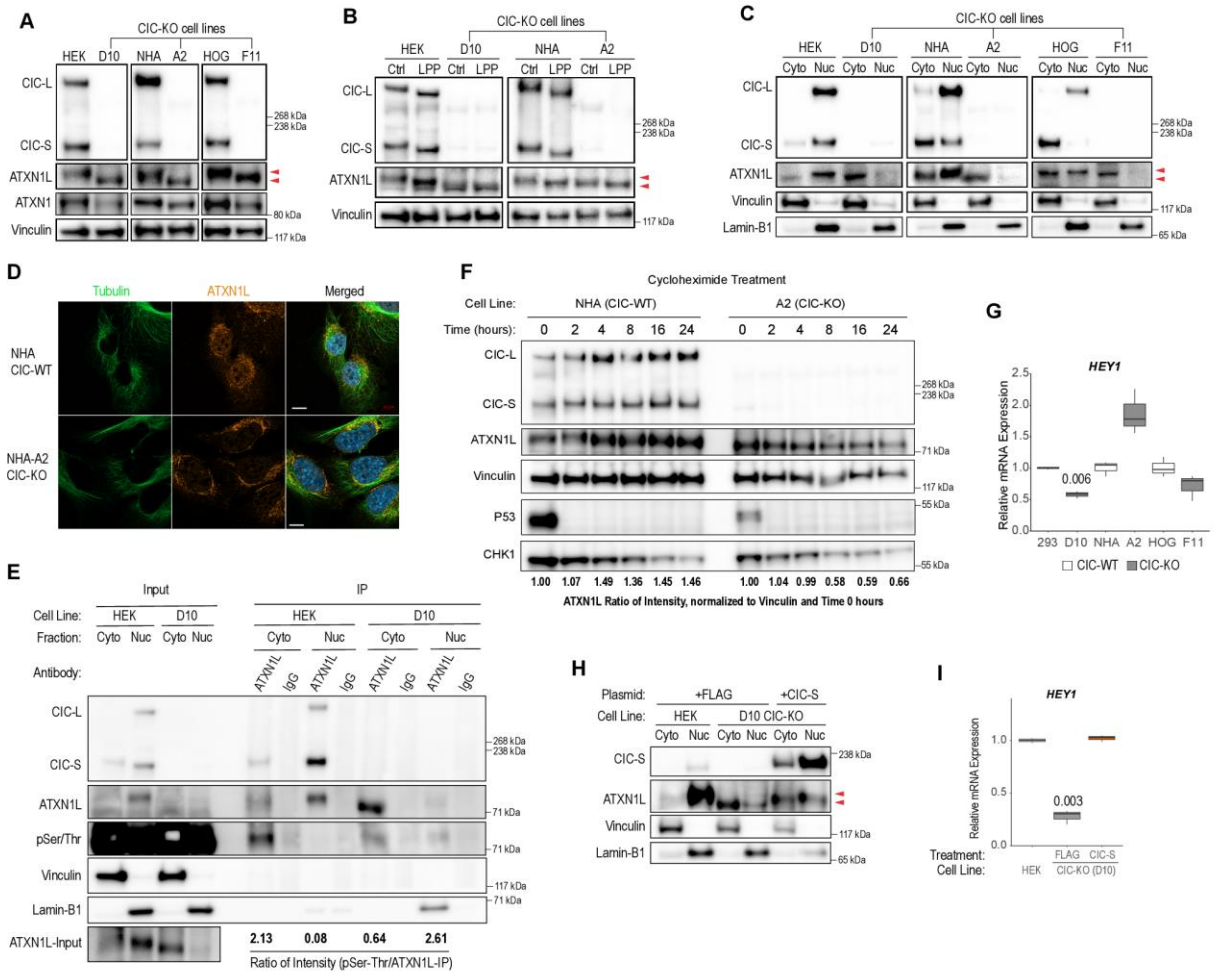

Figure 4.2 – Loss of CIC is associated with ATXN1L dysregulation
(A) Representative western blots of parental (HEK, NHA, HOG) and *CIC*^{KO} (HEK-D10, NHA-A2, HOG-F11) cell lines showing a reduction in apparent molecular weight of ATXN1L in CICKO cell lines. Vinculin was used as a loading control. (B) Representative western blot of parental (HEK, NHA) and *CIC*^{KO} (HEK-D10, NHA-A2) cell lines showing the apparent molecular weight of ATXN1L following control or phosphatase treatment (+LPP). Vinculin was used as a loading control. (C) Representative western blots of parental (HEK, NHA, HOG) and *CIC*^{KO} (HEK-D10, NHA-A2, HOG-F11) cell lines following fractionation showing differences in the apparent molecular weight and localization of ATXN1L in the cytoplasmic (Cyto) and nuclear (Nuc) fractions. Vinculin was used as a cytoplasmic control and Lamin-B1 was used as a nuclear control. (D) Immunofluorescent imaging of endogenous ATXN1L (orange) in *CIC*^{WT} (NHA) and *CIC*^{KO} (NHA-A2) cell lines showing ATXN1L localization. Tubulin (green) was stained to show cell morphology and nuclei were stained with DAPI (blue). White bars seen on the merged image represent 10µm. (E) Western blot of endogenous ATXN1L IP following cellular fractionation (Cytoplasm and Nuclear) of *CIC*^{WT} (HEK) and *CIC*^{KO} (D10) cells. Phosphorylated Serine/Threonine (pSer/Thr) was blotted to show the localization of phosphorylated ATXN1L in the presence or absence of CIC. An IgG IP was

performed as a negative control. Vinculin was blotted as a cytoplasmic control and Lamin-B1 was blotted as a nuclear control. (F) Representative Western blot of *CIC*^{WT} (NHA) and *CIC*^{KO} (A2) cells treated with 100μM of cycloheximide over a 24 hour time course showing ATXN1L stability in the presence and absence of CIC. Vinculin was blotted as a loading control and P53 and CHK1 were blotted as protein synthesis inhibition controls. (G) Tukey boxplots showing relative mRNA transcript levels of *HEY1* in parental (HEK, NHA, HOG) and *CIC*^{KO} (HEK-D10, NHA-A2, HOG-F11) cell lines. Data were collected from 3 independent experiments (passages) and p-values were calculated using the two tailed independent Student's t-test comparing *CIC*^{KO} cell lines to their respective parental cell line. (H) Representative western blot of ATXN1L showing apparent molecular weight and cellular localization following reintroduction of CIC-S-FLAG into HEK-D10 (*CIC*^{KO}) cells. Vinculin was used as a cytoplasmic control and Lamin-B1 was used as a nuclear control. (I) Tukey boxplots showing relative mRNA transcript levels of *HEY1* following reintroduction of CIC-S-FLAG into HEK-D10 (*CIC*^{KO}) cells. Data were collected from 3 independent experiments and p-values were calculated using the two tailed independent Student's t-test comparing FLAG and CIC-S-FLAG treated cells to the parental HEK cells.

4.2.3 ATXN1L mediated CIC instability is independent of ERK activity

Previous studies have established ERK as a downstream component of the mitogen activated protein kinase (MAPK) pathway important for regulating the protein expression, localization, and function of CIC through phosphorylation [21, 25-27, 57, 116]. Additionally, transcriptomic analyses of *ATXN1L*^{KO} cell lines and The Cancer Genome Atlas (TCGA) patient samples have shown upregulation of gene signatures related to MAPK signaling (Figure 4.3A) [54]. To further interrogate the mechanism of CIC degradation following *ATXN1L* loss, we investigated whether ERK activity contributes to the regulation of CIC function in relation to *ATXN1L* status. Phosphorylated ERK (pThr202/Tyr204) was found to be decreased in our *ATXN1L*^{KO} cell lines compared to the *ATXN1L*^{WT} cell lines, detected using ELISA (Figure 4.3B) and Western Blot (Figure 4.3C). Despite the lack of increased ERK activity, *ATXN1L*^{KO} cell lines displayed mRNA upregulation of the many CIC target genes (*ETV1/4/5, DUSP6, SPRY4*) which are downstream of ERK signaling (Figure 4.3D), consistent with previously published data [54]. Further, dual inhibition of MEK and ERK using small the molecule inhibitors trametinib and LY3214996, respectively; did not rescue CIC protein expression in *ATXN1L*^{KO} cell lines (Figure 4.3E) or following siRNA knockdown of *ATXN1L* in *ATXN1L*^{WT} cell lines (Figure 4.3F).

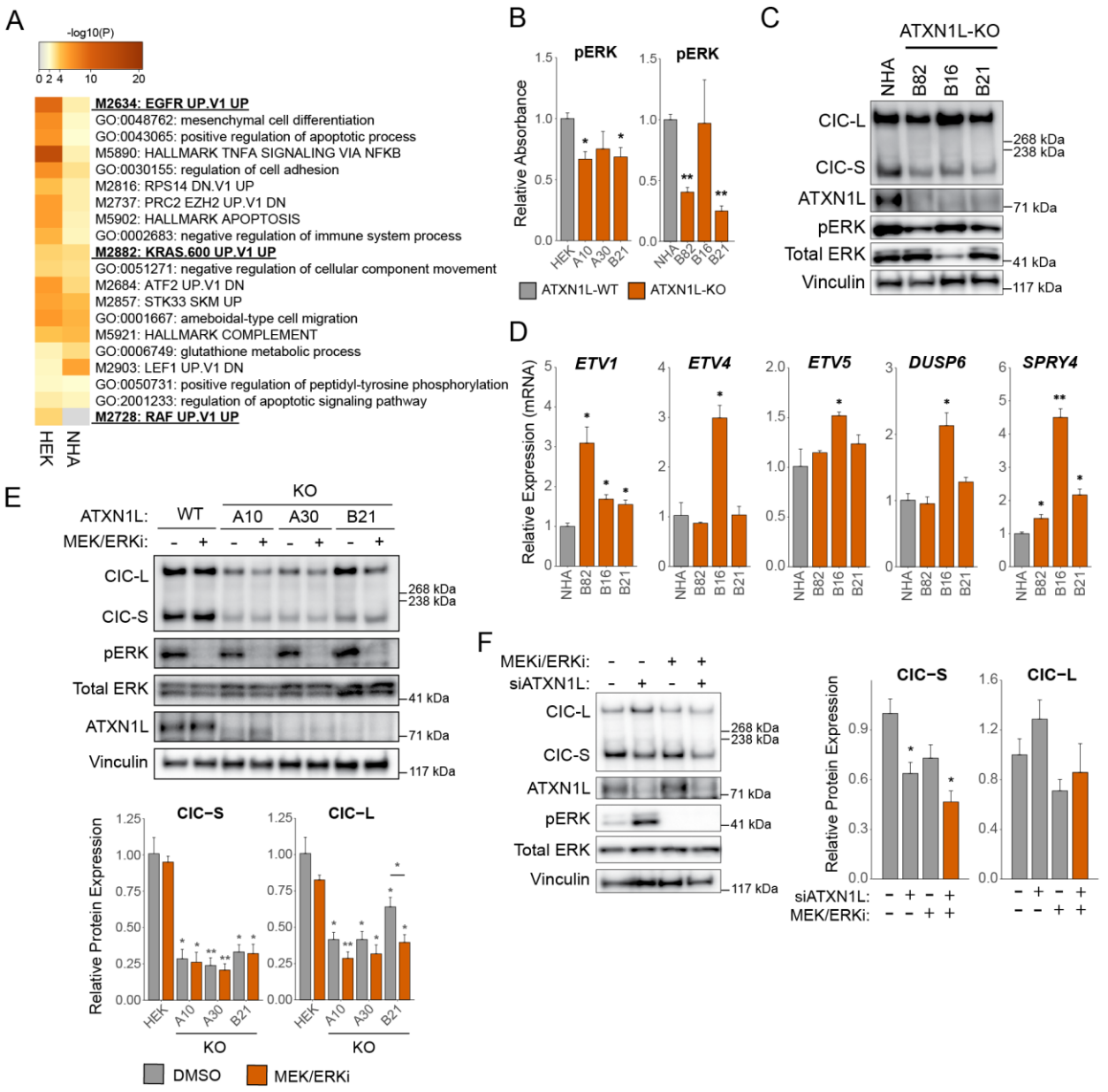

Figure 4.3 – ATXN1L mediated CIC instability is independent of ERK activity
(A) Heatmap showing the top 20 upregulated gene sets in *ATXN1L*^{KO} NHA and HEK cell lines. Terms related to the MAPK pathway are bolded. (B) ELISA quantification of phosphorylated ERK (pThr202/Tyr204) in *ATXN1L*^{WT} and *ATXN1L*^{KO} NHA and HEK cell lines. Quantifications were normalized to total ERK. (C) Representative Western blot of phosphorylated ERK (pThr202/Tyr204) in *ATXN1L*^{WT} (NHA) and *ATXN1L*^{KO} (B82, B16, B21) cell lines. (D) Relative mRNA expression of CIC target genes *ETV1/4/5*, *DUSP6*, *SPRY4* in *ATXN1L*^{WT} (NHA) and *ATXN1L*^{KO} (B82, B16, B21) cell lines. Gene expression was normalized to TBP and the parental *ATXN1L*^{WT} (NHA) cell line was used as a relative control. (E) Representative Western blot of *ATXN1L*^{WT} (HEK) and *ATXN1L*^{KO} (A10, A30, B21) cell lines treated with MEK/ERK inhibitors trametinib/LY3214996. DMSO was used as a negative control. Below: barplot quantifications of CIC expression. Quantifications were normalized to Vinculin. (F) Representative Western blot of *ATXN1L*^{WT} (HEK) cells treated with MEK/ERK inhibitor and *ATXN1L* siRNA. DMSO and scrambled siRNA used as negative controls. Right: barplot quantification of CIC expression. Quantifications were normalized to Vinculin. *Western blot, ELISA, and RT-qPCR quantifications were collected from three independent experiments. Error bars represent one standard deviation. p-values were calculated using the two-tailed independent Student's t-test. Statistically significant values are denoted (* = $p < 0.05$, ** = $p < 0.01$).

4.2.4 Inactivation of CIC by ERK remains intact and independent of ATXN1L

Despite observing no involvement of ERK in the reduction of CIC protein expression in *ATXN1L*^{KO} cells, we were interested to determine if ERK mediated CIC dysregulation remained intact in our cell system. Treatment of *ATXN1L*^{WT} and *ATXN1L*^{KO} cells with epidermal growth factor (EGF)/fibroblast growth factor (FGF) following serum starvation resulted in an increase of CIC protein expression in both *ATXN1L*^{WT} and *ATXN1L*^{KO} cells (Figure 4.4A, Supplemental Figure 12A, B), which could be rescued with dual MEK/ERK inhibition (Figure 4.4B, Supplemental Figure 12C). CIC localization was also not affected by EGF/FGF treatment as observed using immunofluorescence (Figure 4.4C). Although CIC protein expression was observed to increase in our cell systems, derepression of several CIC target genes (*ETV1/4/5, DUSP6, SPRY4*; Figure 4.4D and Supplemental Figure 12D, E) and decreased CIC binding to the promoter region of target genes (*ETV4, DUSP6, SPRY4*; Figure 3E) was observed following EGF/FGF treatment. The increase in CIC protein expression in our cell systems following EGF/FGF treatment was unexpected and thus were further validated in glioblastoma (GBM) cell lines (Supplemental Figure 13A, B) and primary brain tumour initiating cells (BTIC; Supplemental Figure 13C). All cell systems exhibited behavior consistent with our previous observations.

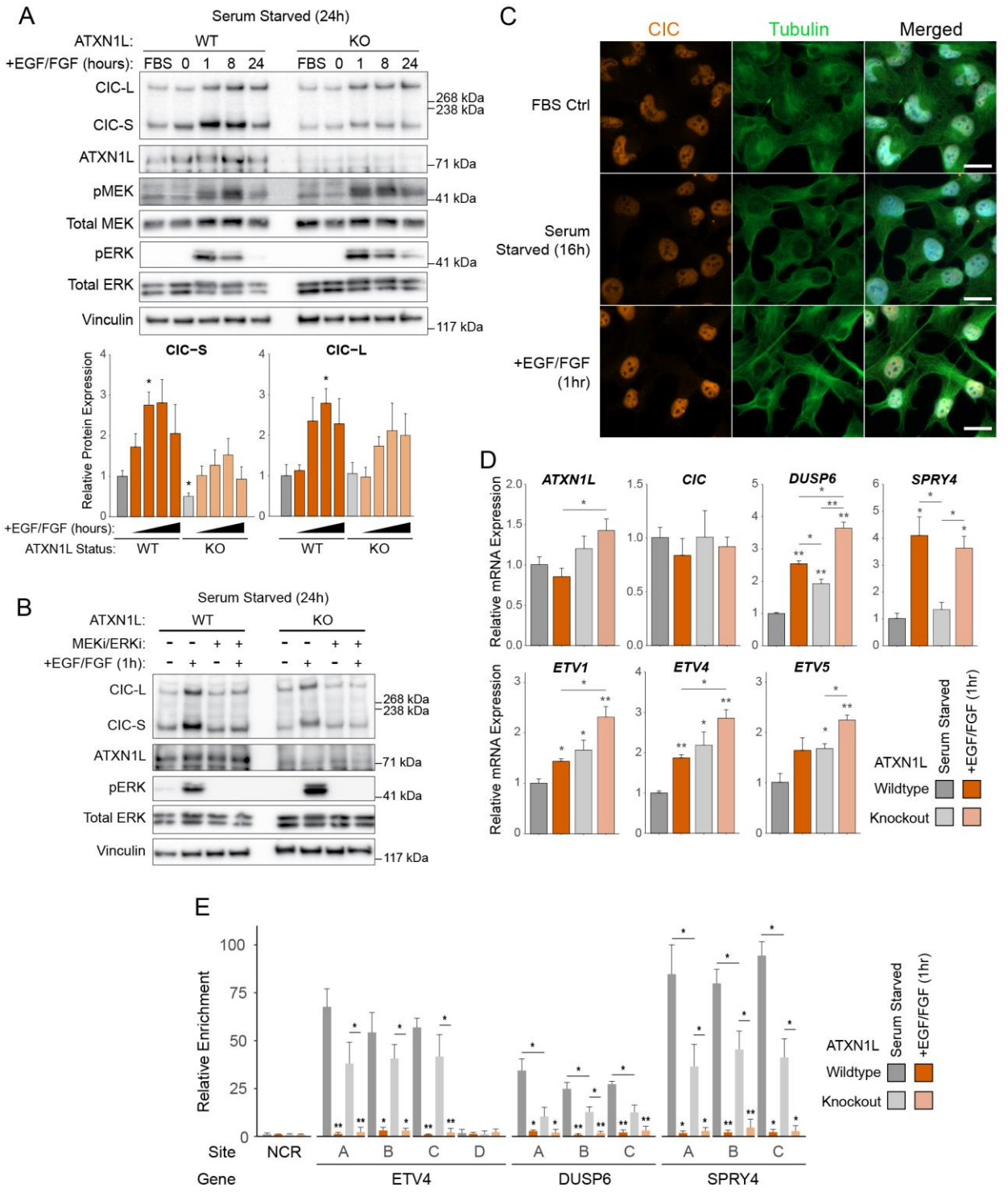

Figure 4.4 – ERK activity relieves CIC repressive function
(A) Representative Western blot of *ATXN1L*^{WT} (HEK) and *ATXN1L*^{KO} (A30) cell lines treated with FGF/EGF over 0-24 hours following serum starvation. FBS control was cultured in FBS for the duration of the timecourse. Below: barplot quantifications of CIC expression. Quantifications were normalized to Vinculin. (B) Representative Western blot of *ATXN1L*^{WT} (HEK) and *ATXN1L*^{KO} (A30) cell lines treated with FGF/EGF and MEK/ERK inhibitors trametinib/LY3214996. (C) Immunofluorescence images of NHA cells cultured in FBS, serum starvation, and EGF/FGF. White bars denote 10µm. (D) Relative mRNA expression of *ATXN1L*, *CIC*, and CIC target genes *DUSP6*, *SPRY4*, and *ETV1/4/5* in *ATXN1L*^{WT} (NHA) and *ATXN1L*^{KO} (B82) cell lines treated with FGF/EGF for 8

hours following serum starvation. Gene expression was normalized to TBP and serum starved parental *ATXN1L*^{WT} (NHA) cell line was used as a relative control. (E) ChIP-PCR showing relative enrichment of CIC-DNA interaction following serum starvation or treatment with EGF/FGF (1 hour) in *ATXN1L*^{WT} (HEK) and *ATXN1L*^{KO} (A30) cell lines. Relative enrichment was normalized to a control region. (*) Western blot, RT-qPCR, and ChIP-PCR quantifications were collected from three independent experiments. Error bars represent one standard deviation. p-values were calculated using the two-tailed independent Student's t-test. Statistically significant values are denoted (* = $p < 0.05$, ** = $p < 0.01$).

4.2.5 CIC degradation is mediated by the E3-ligase TRIM25

To further investigate CIC interactors which may be responsible for mediating the degradation of CIC protein following ATXN1L loss, CIC immunoprecipitation was performed in *ATXN1L*^{KO} cell lines treated with MG132 and interacting proteins were identified using mass spectrometry. Previously identified CIC interactors such as 14-3-3 regulatory proteins and the ATXN1L homologue ATXN1 were highly enriched (Figure 4.5A and Supplemental Table S11). Using *CIC*^{KO} cell lines with stably expressing FLAG-tagged CIC-S [117], CIC interaction with 14-3-3 regulatory proteins and the nuclear pore protein TPR were observed to increase following siRNA knockdown of *ATXN1L* using PLA (Supplemental Figure 14A, B, C). CIC was not found to interact with many previously identified proteins involved in transcriptional regulation such as SIN3A, HDAC1/2, and members of the SWI/SNF complex in our *ATXN1L*^{KO} background [117-119]. Amongst the most highly enriched CIC interactors was the RING-finger E3-ligase TRIM25. CIC interaction with TRIM25 was validated using immunoprecipitation (Figure 4.5B and Supplemental Figure 14D) and PLA (Figure 4.5C) and was found to be elevated in both *ATXN1L*^{KO} and *ATXN1L* knockdown cell systems. Knockdown of *TRIM25* using siRNA was able to induce increased protein expression of both CIC isoforms in *ATXN1L*^{WT} and *ATXN1L*^{KO} cells (Figure 4.5D); and decrease mRNA expression of CIC target genes *ETV1/4/5* (Figure 4.5E). Ectopic overexpression of FLAG-tagged TRIM25 resulted in a further decrease in CIC protein expression in *ATXN1L*^{KO} cells (Figure 4.5F). TRIM25 was observed to localize to both the cytoplasm and nucleus (Supplemental Figure 14F).

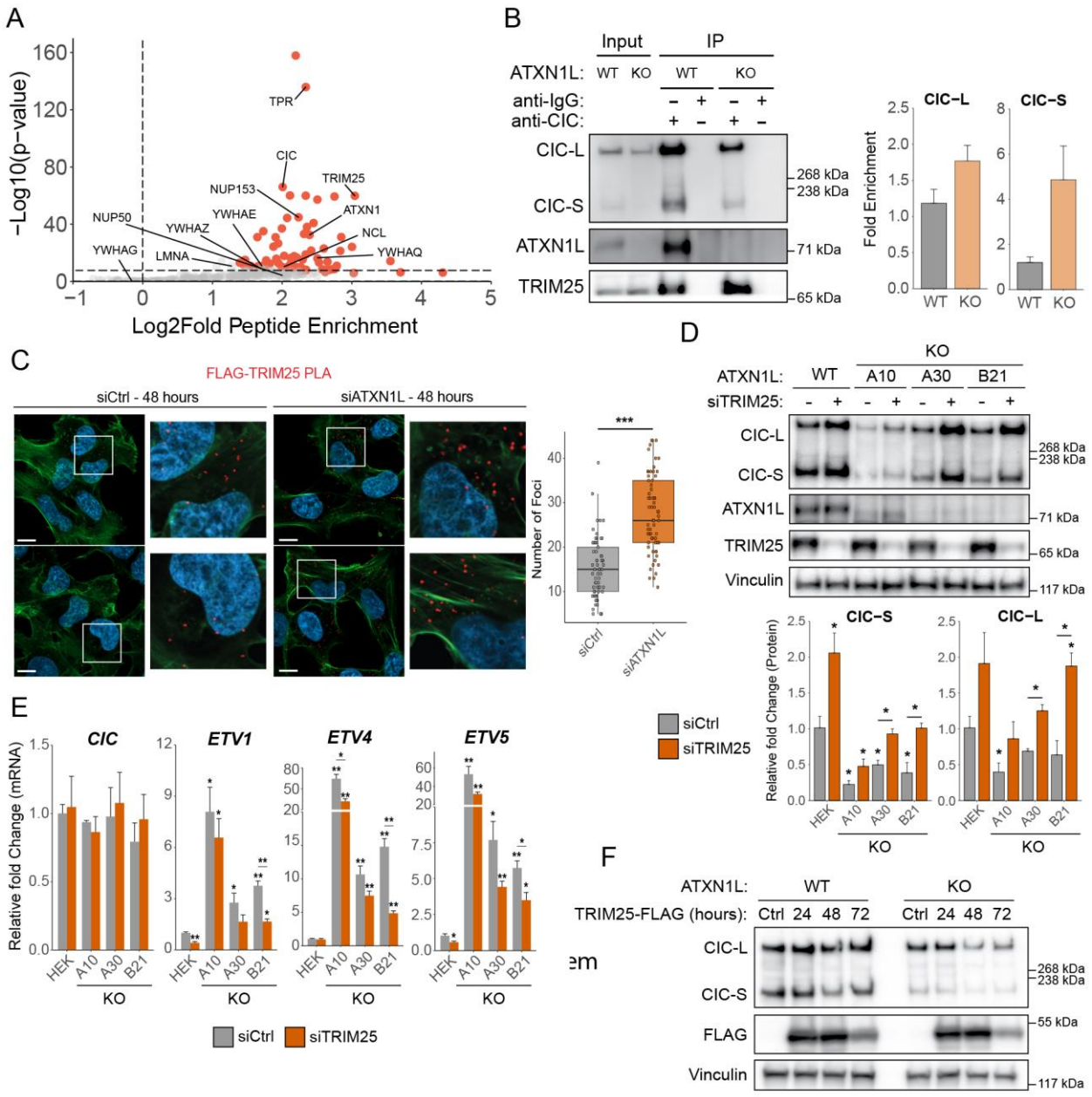

Figure 4.5 – CIC Interacts with the E3-Ligase TRIM25

(A) Volcano plot showing CIC interacting proteins identified using CIC immunoprecipitation followed by mass spectrometry in *ATXN1L*^{KO} NHA cells. Red data points are high confidence interactors. (B) Representative Western blot of CIC immunoprecipitation showing interaction with TRIM25 in *ATXN1L*^{WT} (NHA) and *ATXN1L*^{KO} (B82) cell lines. Right: barplot showing quantifications of TRIM25 Western blots. Quantifications were normalized to CIC Western blots. (C) Immunofluorescence images of proximity ligation assay showing CIC-S-FLAG-TRIM25 interaction in *ATXN1L*^{WT} cells treated with *ATXN1L* siRNA. Scrambled siRNA was used as a negative control. White bars denote 10µm. Right: Tukey boxplots showing quantification of number of foci/cell. (D) Representative Western blot of *ATXN1L*^{WT} (HEK) and *ATXN1L*^{KO} (A10, A30, B21) cell lines treated with *TRIM25* siRNA. Scrambled siRNA was used as a negative control. Below: barplot quantifications of CIC expression. Quantifications were normalized to Vinculin. (E) Relative mRNA expression of *CIC* and CIC target genes *ETV1/4/5* following treatment with *TRIM25* siRNA for 48 hours. Scrambled siRNA was used as a negative control. Gene expression was normalized to TBP. (F) Representative Western blot of *ATXN1L*^{WT} (NHA) and *ATXN1L*^{KO} (B82) cell lines ectopically overexpressing FLAG-tagged TRIM25. Empty FLAG vector was used as a negative control. *Western blot and RT-qPCR quantifications were collected from three independent experiments. PLA quantifications were collected from 65 individual cells. Error bars represent one standard deviation. p-values were calculated using the

two-tailed independent Student's t-test. Statistically significant values are denoted (* = $p < 0.05$, ** = $p < 0.01$, *** = $p < 0.001$).

4.2.6 Glioblastoma cell lines exhibit ATXN1L mediated CIC instability and TRIM25 mediated degradation

To further validate our observations, we investigated the relationship between ERK, CIC, ATXN1L, and TRIM25 in additional cellular and biological systems. CIC was found to be expressed in several GBM and primary brain tumour initiating cell (BTIC) lines (Figure 4.6A, B) despite exhibiting increased expression of CIC target genes downstream of MAPK (*ETV1/4/5*, *DUSP6*, *SPRY4*: Supplemental Figure 15A, B), compared to NHA cells. Strong expression of CIC was not expected in GBM cell lines [57]. Therefore, CIC expression was verified in both low and high- grade patient glioma samples using IHC (n=17) and found to be expressed across all subtypes, with lower expression in oligodendroglioma (Figure 4.6C, D). To determine the role of ERK and ATXN1L in regulating CIC protein expression, GBM and BTIC cell lines were treated with dual MEK and ERK inhibition which did not increase CIC expression, consistent with our previous observations (Figure 4.6E, Supplemental Figure 16A). Similarly, knockdown of *ATXN1L* did result in decreased CIC protein expression in both GBM (Supplemental Figure 16B) and BTIC (Figure 4.6F) cell lines. Derepression of CIC target genes (*ETV1/4/5*, *DUSP6*, *SPRY4*) was also observed following siRNA knockdown of *ATXN1L* in GBM (Figure 4.6G, Supplemental Figure 16C) and BTIC (Supplemental Figure 16D) cell lines; while siRNA knockdown of *TRIM25* resulted in further repression. Dual inhibition of MEK and ERK were not sufficient to rescue decreases in CIC protein expression following siRNA knockdown of *ATXN1L* (Figure 4.6H, Supplemental Figure 16E), whereas, concurrent knockdown of *ATXN1L* and *TRIM25* was able to rescue decreased CIC protein (Figure 4.6I, Supplemental Figure 16F).

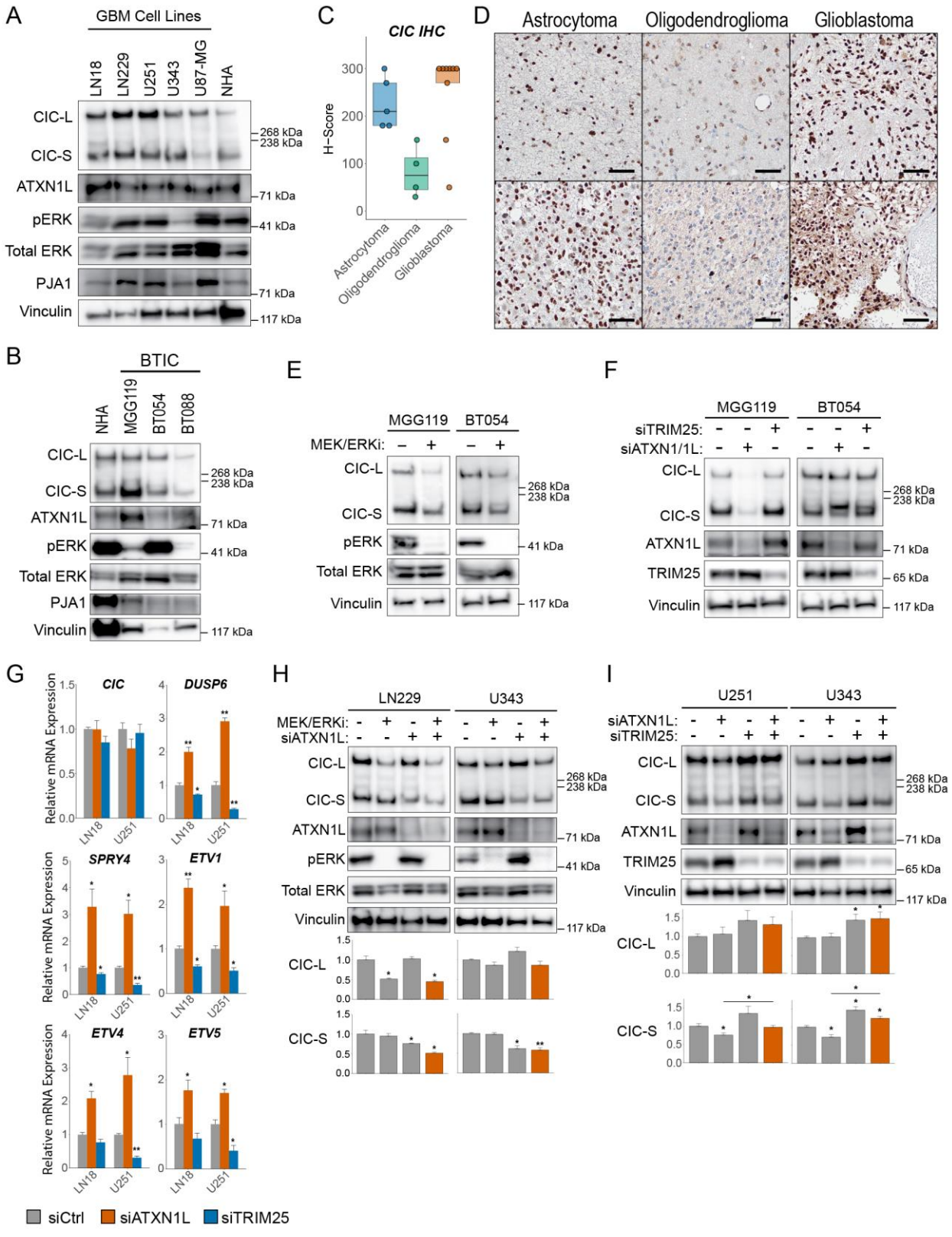

Figure 4.6 – TRIM25 and ATXN1L mediated CIC stability in GBM cell lines
(A) Representative Western blot of CIC, ATXN1L, and phosphorylated ERK (pThr202/Tyr204) expression in GBM cell lines. (B) Representative Western blot of CIC, ATXN1L, and phosphorylated ERK (pThr202/Tyr204) expression in BTIC cell lines. (C) Tukey boxplots showing H-scores of CIC immunohistochemistry staining on

glioma samples. (D) Immunohistochemistry images of CIC staining on glioma samples. Black bars denote 200μm. (E) Representative Western blot of BTIC cell lines in standard EGF/FGF culture conditions and following 16 hours of MEK/ERK inhibition. (F) Representative Western blot of BTIC cell lines following siRNA knockdown of ATXN1L or TRIM25. Fluorescent RNA was used as a negative control. (G) Relative mRNA expression of CIC and CIC target genes (DUSP6, SPRY4, ETV1/4/5) following treatment with ATXN1L or TRIM25 siRNA for 48 hours in LN18 and U251 cell lines. Scrambled siRNA was used as a negative control. Gene expression was normalized to TBP. (H) Representative Western blot of LN229 and U343 cell lines treated with MEK/ERK inhibitors trametinib/LY3214996 and/or ATXN1L siRNA. DMSO and scrambled siRNA were used as negative control. Below: barplot quantifications of CIC protein expression. (I) Representative Western blot of U251 and U343 cell lines treated with ATXN1L and/or TRIM25 siRNA. Scrambled siRNA were used as negative control. Below: barplot quantifications of CIC protein expression. *Western blot and RT-qPCR quantifications were collected from three independent experiments. Error bars represent one standard deviation. p-values were calculated using the two-tailed independent Student's t-test. Statistically significant values are denoted (* = $p < 0.05$, ** = $p < 0.01$).

4.2.7 *TRIM25* amplification and *CIC* deletion dysregulate similar gene sets

Probing the TCGA database, alterations in *TRIM25* were observed in several cancer types, most notably, amplifications in the invasive breast carcinoma (BRCA) and mesothelioma data sets (Figure 4.7A). To determine if TRIM25 may regulate the transcription factor functions of CIC, differentially expressed (DE) genes using published gene expression data of TRIM25 knockdown in breast cancer cell lines (BT549 and MDA-MB-231, Supplemental Table 12) from Walsh *et al*. (https://doi.org/10.1016/j.celrep.2017.07.052) [95] were compared to DE genes identified in CIC^{KO} and $ATXN1L^{KO}$ NHA cell lines (Supplemental Table 13A, B). As *TRIM25* was knocked down, we expected directional discordance between DE genes identified in *TRIM25* knockdown versus CIC^{KO}/$ATXN1L^{KO}$. Of the 1531 DE genes identified in the *TRIM25* knockdown cell lines (FDR < 0.05, concordant direction), 161 (131 discordant) were shared with CIC^{KO} and 122 (104 discordant) were shared with $ATXN1L^{KO}$ DE genes (Figure 4.7B and Supplemental Tables 14A, B). Gene set enrichment analysis of discordant genes identified several terms related to cell growth/proliferation, and cell attachment/organization which is consistent with CIC/ATXN1L's function as regulators of the cell cycle and metastasis (Supplemental Figure 17 and Supplemental Table 15A, B).

To further validate the relationship between TRIM25 and CIC, differential expression analysis was performed using the TCGA BRCA cohort comparing samples with *TRIM25* amplification versus samples with copy number neutral *TRIM25*. A total of 2789 DE genes were identified (FDR < 0.01, Fold change > 1.5; Supplemental Table 16A) which were then compared to previously identified DE genes in TCGA type II low grade glioma (Type II LGG, n=1538), prostate adenocarcinoma (PRAD, n=842), and stomach adenocarcinoma (STAD, n=3223) with *CIC* copy number loss (Supplemental Tables 6, 7, 8), expecting directional concordance. 347 genes (321 concordant), 290 (221 concordant), and 682 (553 concordant) DE genes were shared

between BRCA and Type II LGG, PRAD, and STAD, respectively (Figure 4.7C, Supplemental Table 16B, C, D). Gene set enrichment analysis of upregulated and directionally concordant DE genes shared between BRCA and Type II LGG/PRAD/STAD identified several terms related to cell cycle, consistent with previously published work and our cell line analyses (Figure 4.7D, Supplemental Table 17). BRCA patients which expressed high *TRIM25* expression (top 25%) also showed decreased overall survival (Figure 4.7E).

In addition to the TCGA BRCA cohort, *TRIM25* was further investigated in the TCGA liver hepatocellular carcinoma (LIHC) cohort in which CIC dysregulation, at the proteomic level, has been described as a negative prognostic factor [33, 120]. Patients with high *TRIM25* expression (top 25%) were found to have higher expression of the CIC target genes *ETV1/4/5* (Figure 4.7F) as well as decreased overall survival (Figure 4.7G).

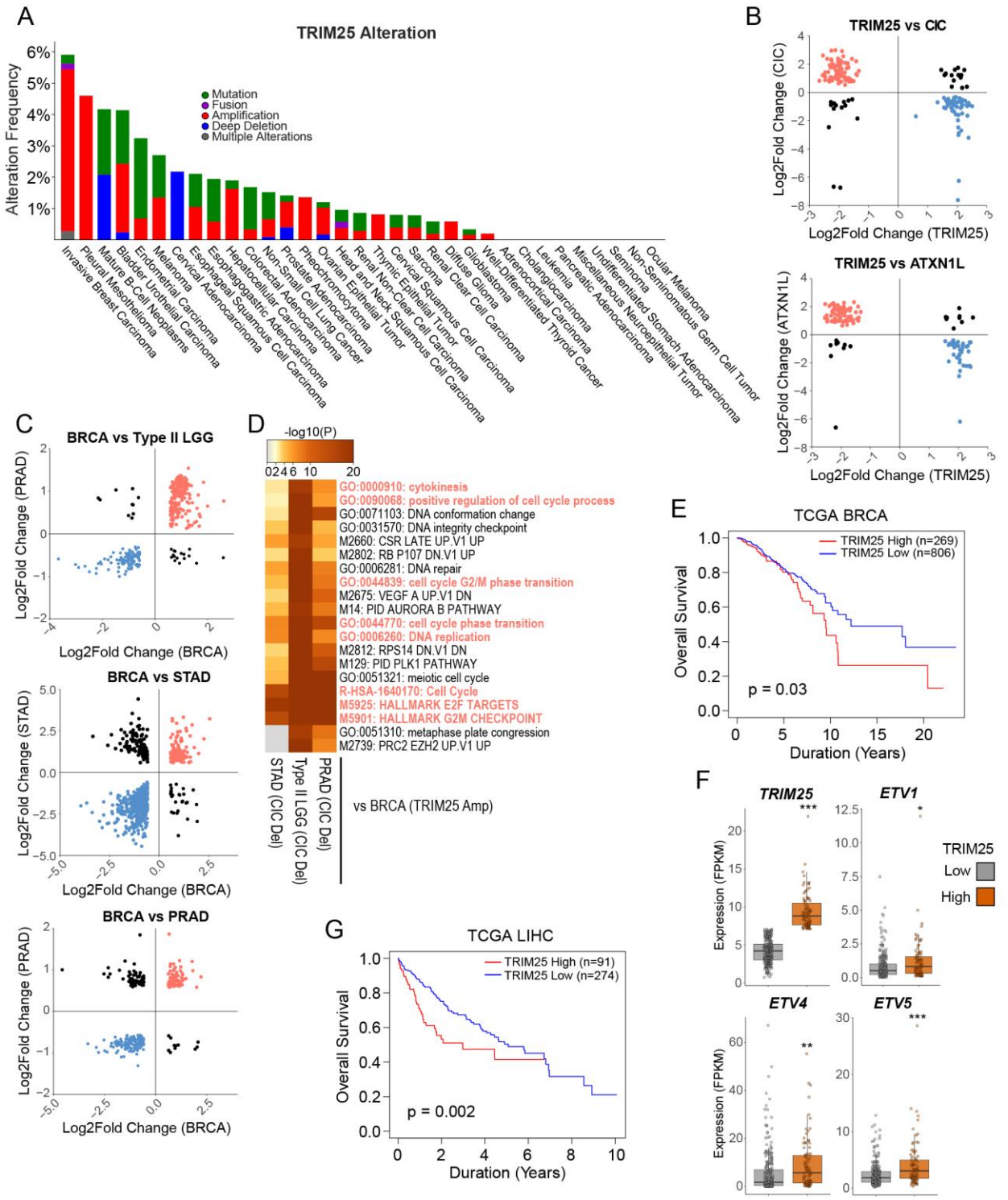

Figure 4.7 – CIC, ATXN1L, and TRIM25 regulate cell cycle *in vitro* and in TCGA patient data
(A) Barplot displaying frequency of *TRIM25* alterations in the TCGA pan-cancer study. Bars are based upon cancer subtype and split based on alteration type. (B) Scatter plot showing Log2Fold change of differentially expressed genes shared between *TRIM25* siRNA in BT549 and MDA-MB-231 breast cancer cell lines and *CIC/ATXN1L* knockout in NHA cell lines. Differentially expressed genes with directionally discordant change are colored (red/blue). (C) Scatter plot showing Log2Fold change of differentially expressed genes shared between TCGA BRCA samples with *TRIM25* amplification and TCGA Type II LGG, PRAD, and STAD samples with *CIC* deletions. Differentially expressed genes with directionally concordant change are colored. Red terms relate to cell cycle, growth, and proliferation. Blue terms relate to cell structure, organization, and adhesion. (D) Heatmap

showing the top 20 enriched gene sets for directionally concordant upregulated differentially expressed genes shared between TCGA BRCA samples with *TRIM25* amplification and TCGA Type II LGG, PRAD, and STAD samples with *CIC* deletions. Highlighted terms are color coded respective to the cluster used for gene set enrichment analysis in panel D. Red terms are related to cell cycle, growth, and proliferation. (E) Kaplan-Meier curve showing overall survival of TCGA BRCA patients with high (top 25%) and low (bottom 75%) *TRIM25* expression. (F) Tukey barplots showing expression of *TRIM25, ETV1, ETV4,* and *ETV5* in TCGA LIHC samples with high (top 25%) and low (bottom 75%) *TRIM25* expression. (G) Kaplan-Meier curve showing overall survival of TCGA LIHC patients with high (top 25%) and low (bottom 75%) *TRIM25* expression. (*) Statistically significant values are denoted (* = $p < 0.05$, ** = $p < 0.01$, *** = $p < 0.001$).

4.3 Discussion

In this study we explore the post-translational regulation of CIC in the context of ATXN1L loss and uncover a novel mechanism of CIC protein regulation independent of ERK activity in several cellular systems and contexts (Figure 4.8). The role of ATXN1L as a mediator of CIC repressor function has been well established through several functional studies, both *in vitro* and *in vivo* [29, 54, 65]; though little has been explored in regards to the mechanisms of ATXN1L mediated post-translational stability of CIC. Using isogenic *ATXN1L*^{KO} cell lines, CIC instability was observed to be a downstream consequence of increased ubiquitin accumulation and that inhibition of ERK did not affect this CIC instability. Studies investigating the regulation of CIC protein expression in *Drosophila melanogaster* have established ERK as an important mediator of CIC stability through phosphorylation [21, 24-27]. However, unlike mammalian cells, *Drosophila melanogaster* lack an orthologue of *ATXN1L* suggesting that mammalian cells may have evolved several independent pathways to intricately regulate the post-translational function and stability of CIC. This can be evidenced by the temporal differences in CIC inactivation following loss of ATXN1L (hours) [54] versus phosphorylation by ERK (minutes) [31], which may suggest that CIC instability resulting from loss of ATXN1L may be due to an increased rate of normal CIC turnover.

In this study, ERK activity was observed to alleviate CIC repressive function; but, contrary to several studies, CIC protein expression increased or remained constant. This discrepancy may be due to context specific and complex regulatory networks involving CIC in mammalian cells that have not been fully explored. As most mammalian studies investigating the role of ERK in regulating CIC stability have been performed in the context of cancers driven heavily by MAPK activation (melanoma, lung adenocarcinoma, glioblastoma), our observations may be due to post-translational feedback loops that are protective against cytotoxic ERK hyperactivation [121] in cell systems that are not heavily driven by or adapted to high levels of

MAPK activation. This study also establishes that the regulation of CIC function and protein stability is regulated by independent pathways, dependent on the cellular context.

Figure 4.8 – Proposed mechanistic model of CIC-ATXN1L-TRIM25 interaction

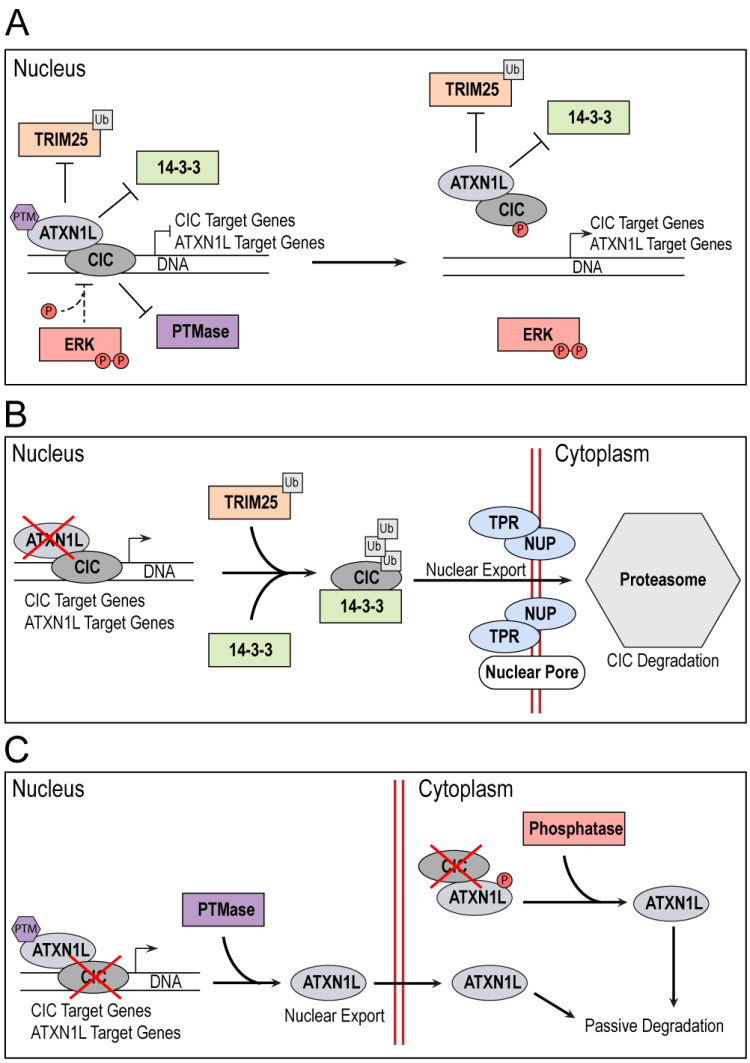

(A) CIC-ATXN1L form a repressive complex which stabilizes CIC from degradation by TRIM25 and protects ATXN1L from loss of an unknown post-translational modification. (B) In the absence of ATXN1L, CIC is targeted by TRIM25 for degradation by ubiquitination and transported for degradation through the nuclear pore by 14-3-3 chaperones. (C) In the absence of CIC, ATXN1L undergoes loss of an unknown post-translational modification and exclusion from the nucleus. In the cytoplasm, phosphorylated ATXN1L is targeted by an unknown phosphatase resulting in degradation and instability.

In addition, this study identified the RING-finger E3-ligase TRIM25, an important mediator of anti-viral activity [122, 123], as a mediator of CIC post-translational stability. Interestingly, PJA1, another E3-ligase involved in the post-translational regulation of CIC also contains a RING-finger domain and has been implicated in the innate immune system. Overexpression of *TRIM25* was able to reduce CIC protein expression while siRNA knockdown of *TRIM25* was able to stabilize CIC and promote its tumour suppressor function. Utilising previously published gene expression data and TCGA cohorts, *TRIM25* amplification in breast carcinoma was found to dysregulate several shared gene sets, related to cell growth and proliferation, with CIC loss. Interestingly, CIC loss has been linked to increased cancer stem cell-like properties in breast cancer cells [124]. Decreased overall survival was also observed in patients with higher *TRIM25* expression in both the BRCA and LIHC TCGA cohorts further supporting the status of CIC function as a prognostic indicator. Although the majority of TRIM25 studies have been focussed on its role as a negative regulator of viral replication, several studies have also suggested that overexpression of TRIM25 may promote tumour

progression in hepatocellular carcinoma [125] and lung cancer [126], cell growth and proliferation in prostate adenocarcinoma [127] and breast cancer [128], and metastasis in breast cancer [95], supporting the role of TRIM25 as an oncogene. CIC, which has now been established as a potent tumour suppressor gene, has also been identified as a positive regulator of viral replication [129] which suggests that the CIC-ATXN1L-TRIM25 axis may be relevant in several different cellular and pathological contexts.

Chapter 5: The Effects of IDH mutation on *CIC* and *ATXN1L* loss

5.1 Introduction

One of the defining molecular features of LGG are the recurrent R132 and R172 missense mutations of *IDH1* and *IDH2*, respectively [130]. The most common mutation being the *IDH1* R132H mutation. Under normal physiological conditions, IDH enzymes, which are involved in the citric acid cycle, are responsible for the enzymatic conversion of isocitrate to α-ketoglutarate, a co-factor important for the normal function of dioxygenase dependent enzymes such as the DNA demethylases *TET1/2* and several histone demethylases. The recurrent R132 and R172 missense mutations produce a neomorphic IDH enzyme which can further reduce α-ketoglutarate into 2-hydroxyglutarate (2HG) [131], an oncometabolite which is a competitive inhibitor of dioxygenase dependent demethylases [15, 16] resulting in DNA and histone hypermethylation termed the "hypermethylator phenotype" [17, 18].

In LGG, *CIC* mutations occur exclusively in *IDH* mutated, 1p19q co-deleted tumours suggesting that there may be a functional relationship between *CIC* and *IDH* mutations [11]. One study found that the recurrent missense mutations in the HMG box and C1 motifs co-operatively regulate 2HG levels in cell lines [53]. Interestingly, multiple distinct *CIC* mutations have been found in recurrent IDH mutated LGG samples suggesting there is a strong selective pressure for clones to abrogate *CIC* function [132]. Contrastingly, loss of the mutant IDH allele has also been observed in recurrent LGG samples which may suggest that IDH mutations are dispensable post initiation and co-operation with *CIC* mutations is non-essential [133].

In this chapter, we explore the effects of IDH mutation on the transcriptional network of *CIC* and *ATXN1L*.

5.2 Results

5.2.1 ATXN1L loss in *IDH1-R132H* mutant cells leads to derepression of *CIC* target genes

To establish the functional interaction between CIC and ATXN1L in *IDH* mutant cell lines, NHA cells overexpressing mutant *IDH1-R132H* were treated with siRNA targeted at *ATXN1* or *ATXN1L*. Similar to in our *IDH* wildtype cell lines, knockdown of *ATXN1L* led to a greater and more consistent reduction in CIC protein and derepression of *CIC* target genes (Figure 5.1A/B). Of note, knockdown of *ATXN1L* in this cell system also resulted in *CIC* downregulation which was not seen in our *IDH* wildtype cells. *ATXN1* knockdown did not affect *CIC* expression.

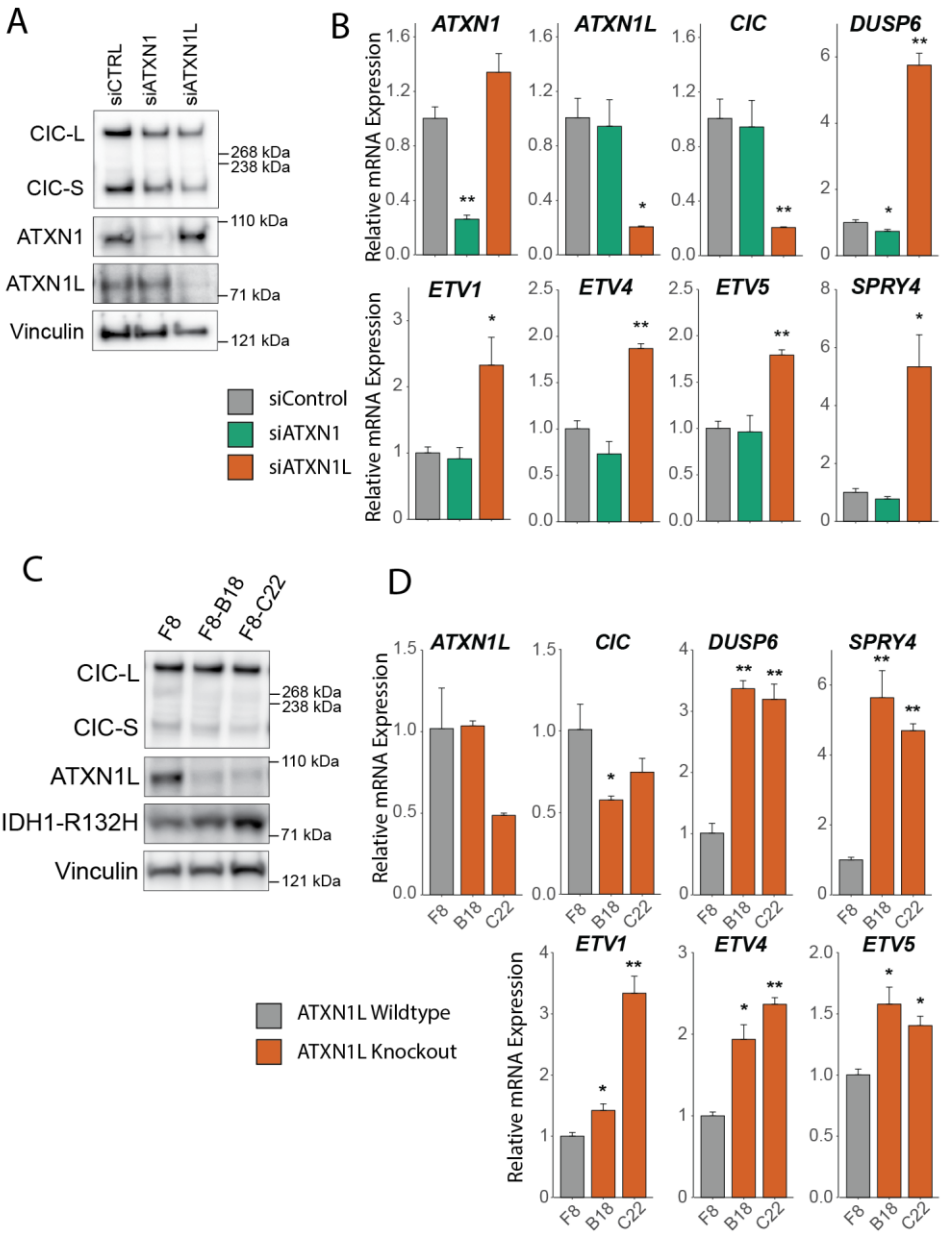

Figure 5.1 – Loss of *ATXN1L* in IDH mutant cells dysregulate CIC function
(A) Representative Western blot IDH-R132H mutant cell line (F8) treated with *ATXN1* or *ATXN1L* siRNA. Scrambled siRNA was used as a negative control. Vinculin was used as a loading control (B) Relative mRNA expression of *CIC, ATXN1, ATXN1L*, and CIC target genes (*ETV1/4/5, DUSP6, SPRY4*) following siRNA knockdown of *ATXN1* or *ATXN1L* in IDH-R132H mutant cells (F8). Expression was normalized to TBP and Scrambled siRNA control was used as a relative control. (C) Representative Western blot of IDH1-R132H mutant *ATXN1L*^{KO} cell lines (B18, C22). Vinculin used as a loading control. (D) Relative mRNA expression of *ATXN1L, CIC,* and CIC target genes (*DUSP6, SPRY4, ETV1/4/5*) in IDH1-R132H mutant *ATXN1L*^{KO} cell lines. Expression was normalized to TBP and the parental cell line (F8) was used as a relative control.

5.2.2 IDH mutation dampens the transcriptomic effects of *ATXN1L* and *CIC* loss

To investigate the effects of IDH mutation on the functional transcriptomic relationship between CIC and ATXN1L, differential expression analysis (DEA) was performed comparing IDH mutant *CIC*^{KO} or *ATXN1L*^{KO} cell lines with IDH wildtype cell lines using RNA sequencing data. In the *CIC*^{KO} cell lines, 1258 (724 up, 534 down) DE genes were identified in IDH wildtype cell lines, while 265 (170 up, 94 down) were identified in IDH-R132H mutant cell lines (Figure 5.2A, Supplemental Table 18). Similarly, in the *ATXN1L*^{KO} cell lines, 957 (648 up, 309 down) DE genes were identified in IDH wildtype cell lines, while 251 (106 up, 145 down) were identified in IDH-R132H mutant cell lines (Figure 5.2B, Supplemental Table 19). In both knockout systems, the presence of IDH mutation reduced the number of DE genes, however, the difference in magnitude of differential expression was found to be variable. Comparison of the DE genes identified in *CIC*^{KO} and *ATXN1L*^{KO} cell lines, in both IDH contexts, identified 223 shared DE genes in IDH wildtype (Figure 5.2C and Supplemental Table 20A) and 46 shared DE genes in IDH-R132H mutant cell lines (Figure 5.2C, Supplemental Table 20B). Directional changes in expression in both IDH wildtype and IDH mutant cell lines were highly concordant between *CIC*^{KO} and *ATXN1L*^{KO} cell lines. Interestingly, in the IDH mutant contexts, the canonical CIC target genes *ETV1, ETV4,* and *CCND1* were DE in both *CIC*^{KO} and *ATXN1L*^{KO} cell lines, but in IDH wildtype contexts, these genes were only identified in *CIC*^{KO} cell lines. Gene set enrichment analysis of shared upregulated DE genes between IDH-R132H mutant *CIC*^{KO} and *ATXN1L*^{KO} cell lines converged upon activation of the MAPK pathway which was also identified in the IDH wildtype cell lines (Figure 5.2D, Supplemental Table 21). Other gene sets that were also found to be convergently upregulated in both IDH contexts include activation of the TNFα, NF-κB, IL2/STAT5, Hypoxia, and epithelial to mesenchymal transition. The convergence of gene sets in both IDH contexts highly suggests that the presence of IDH mutation does not greatly affect the pathways dysregulated by loss of *CIC* or *ATXN1L*.

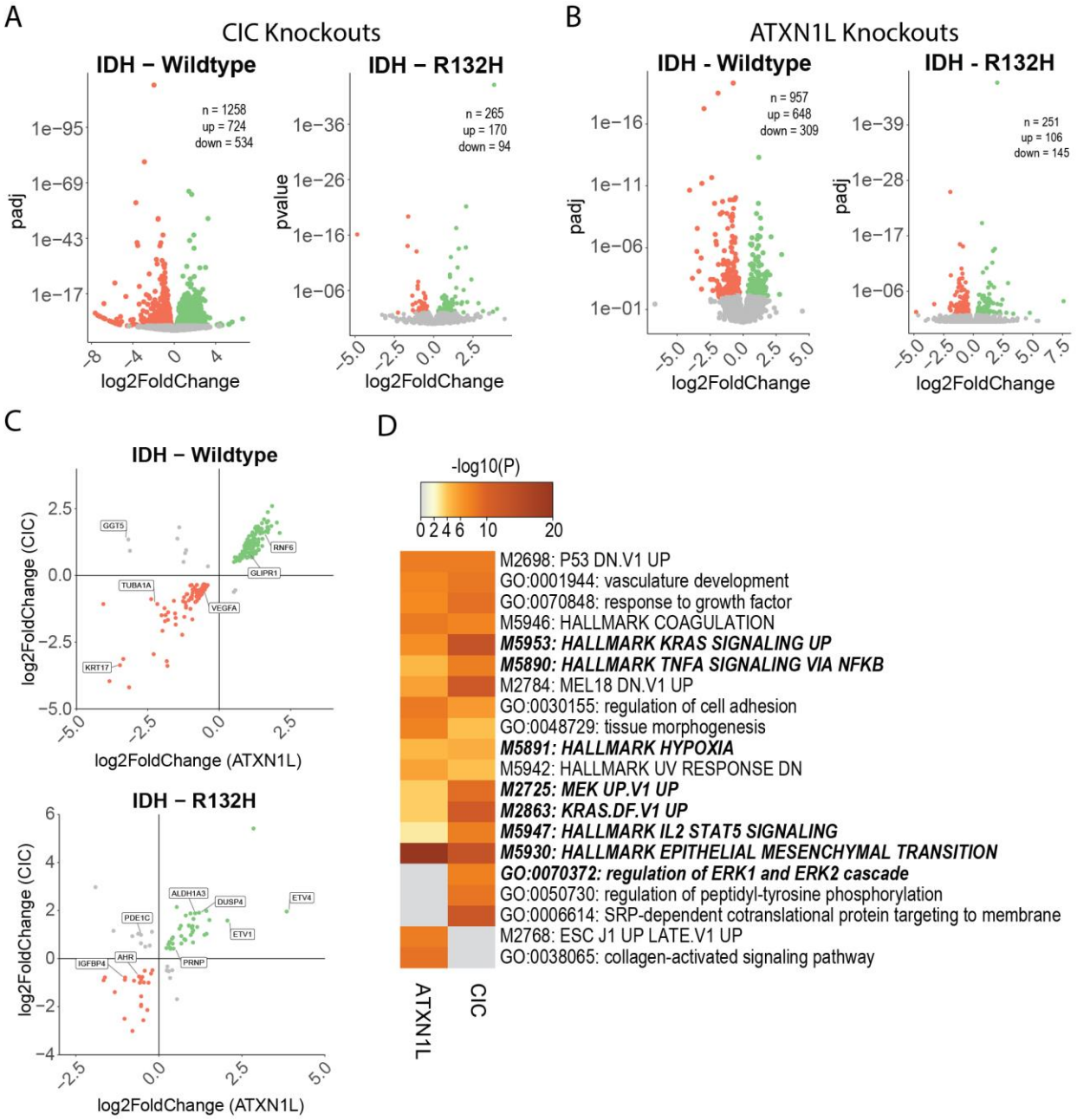

Figure 5.2 – Transcriptomic effects of IDH mutation on *CIC* and *ATXN1L* loss
(A) Volcano plot of differentially expressed genes identified in IDH wildtype and IDH-R132H mutant CICKO cell lines. (B) Volcano plot of differentially expressed genes identified in IDH wildtype and IDH-R132H mutant ATXN1LKO cell lines. (C) Scatter plot of genes which were found to be differentially expressed and shared between CICKO and ATXN1LKO cell lines in IDH wildtype cells (top) and IDH-R132H mutant cells (bottom). (D) Heatmap showing the top 20 enriched terms identified in IDH-R132H mutant CICKO and ATXN1LKO cell lines. Terms in bold italics were terms also identified in IDH wildtype CICKO and ATXN1LKO cell lines.

5.3 Discussion

In this chapter, we explore the effects of the neomorphic IDH mutations found in low grade gliomas on the transcriptomic changes we previously observed in *CIC*^{KO} and *ATXN1L*^{KO} NHA cell lines. Similar to in IDH wildtype NHA cells, siRNA knockdown of *ATXN1L* resulted in a more robust dysregulation of CIC target genes than *ATXN1* knockdown. These observations were consistent with IDH wildtype and R132H mutant *ATXN1L*^{KO} CRISPR cell lines suggesting that the presence of IDH mutation does not affect the transcriptomic relationship between CIC and ATXN1L. Upon further transcriptomic interrogation, a significant reduction in the number of DE genes in the IDH-R132H mutant backgrounds was observed, which supports the notion that the CIC-ATXN1L complex may partially regulate context dependent targets through interaction with the epigenome as the production of 2HG is known to greatly alter the epigenomic landscape in LGG and acute myeloid leukemia [18, 134]. Thus, the presence of IDH mutation may create a "dampening" effect of CIC-ATXN1L in relation to the epigenome and global transcriptome. One interesting thing to note is that while IDH mutation reduced the total number of DE genes, many of the canonical CIC target genes were still observed to be DE in IDH-R132H mutant cell lines suggesting that IDH mutation does not affect the binding of the CIC-ATXN1L to target genes that interact directly with the complex. Additionally, the pathways dysregulated in both IDH contexts were found to converge upon activation of oncogenic pathways such as MAPK, hypoxia, and epithelial to mesenchymal transition. Pathways that were highly enriched only in the IDH mutant contexts such as vasculature development, and downregulation of *TP53*/DNA damage response are also heavily implicated in glioma biology. In contrast, terms related to the epigenome identified in IDH wildtype cell lines, such as activation of EZH2 targets, were not observed to be highly enriched in IDH-R132H cell lines which may be due to the effects of 2HG on influencing the epigenomic landscape. In conclusion, IDH mutation "dampens" the breadth of CIC-ATXN1L's transcriptomic network but does not appear to greatly affect the functional relationship between CIC and ATXN1L nor the pathways it regulates.

Chapter 6: Conclusions

6.1 Summary of study and findings

The role of CIC function as a prognostic indicator has been highlighted by several biological and clinical studies in a multitude of cancer types through the dysregulation of several oncogenic pathways related to the cell cycle, metastasis, and treatment resistance. Most studies have investigated these phenotypes in relation to *ETV1/4/5*, which are the most widely studied and canonical CIC target genes, however, understanding of the mechanisms and interacting partners which govern CIC function are lacking. Additionally, as ectopic restoration of CIC function has been shown to be a powerful tumour suppressor *in vitro*, comprehension of the mechanisms pertinent to CIC activity and regulation may also reveal druggable targets in an effort to restore CIC function in patient tumours.

Dysregulation of CIC function has not only been found to lead to aberrant expression of oncogenic pathways in cancer, it has also been found to promote the pathology of SCA1, a neurodegenerative disease. The importance of normal CIC function in unrelated pathologies suggest that intact CIC is important for not only supressing oncogenic pathways, but also in maintaining normal cellular function. In SCA1, the dysregulation of CIC is strongly linked to a functional interaction with ATXN1 and ATXN1L, though this relationship had previously not been thoroughly explored in cancer. In this thesis, we explored the relationship between CIC and ATXN1L on both the transcriptomic and proteomic level in several cancer types and delve into the mechanisms of CIC regulation in relation to ATXN1L.

Utilising CRISPR/Cas9 generated knockout cell systems and TCGA patient cohorts; in Chapter 3, we reveal a reciprocal transcriptomic relationship between CIC and ATXN1/ATXN1L whereby loss or dysregulation of *CIC* or *ATXN1/ATXN1L* resulted in the dysregulation of highly overlapping gene sets and pathways related to the cell cycle. These pathways included activation of the MAPK, E2F, mTOR, and myc pathways and downregulation of Rb. In addition to cell cycle, dysregulation of the epigenome, particularly, gene sets related to the polycomb repressive complex were highly enriched in TCGA patient cohorts suggesting that the CIC-ATXN1/ATXN1L complex may also play a role in regulating the epigenome. *In vitro*, the dysregulation of CIC target genes, upon loss of ATXN1L, was found to be a result of both decreased CIC protein expression as well as decreased CIC binding to the DNA. While our *in*

vitro cell lines displayed a reliance of CIC on ATXN1L for expression and function, the reliance of CIC on ATXN1 and/or ATXN1L was found to be driven by the cellular context in the patient cohorts analysed (low grade glioma, prostate adenocarcinoma, and stomach adenocarcinoma).

As a downstream effector of the MAPK pathway, previous studies had established the role of ERK phosphorylation in regulating both CIC function and protein stability. However, much of these studies were performed in *Drosophila melanogaster* which lack an ATXN1L ortholog. In Chapter 4, we further delve into the mechanisms involved in the post-translational regulation of mammalian CIC following loss of ATXN1L *in vitro*. While the loss of ATXN1L was found to activate gene sets indicative of MAPK activation, the role of ERK in regulating CIC protein expression and function was found to be independent from ATXN1L. Compared to ERK signaling, which occurs on the scale of minutes, loss of ATXN1L was found to promote CIC ubiquitination and proteasomal degradation through an increased rate of passive degradation on the order of hours. This passive degradation of CIC was found to be mediated by TRIM25, a RING-finger E3-ligase previously implicated in anti-viral replication. Transcriptomic analyses of TCGA patient cohorts also showed that patients with high expression of TRIM25 had decreased overall survival in breast carcinoma, and increased expression of *ETV1/4/5* in liver hepatocellular carcinoma.

Lastly, recurrent CIC mutations were first identified in oligodendroglioma which are molecularly characterized by IDH mutation and 1p19q co-deletion. In Chapter 5, we utilised isogenic IDH1-R132H mutant, CRISPR-Cas9 generated cell lines to investigate the role of IDH mutation on the transcriptomic relationship between CIC and ATXN1/ATXN1L. Similar to IDH wildtype cell lines, loss of *ATXN1L* in IDH1-R132H cell lines resulted in the dysregulation of several CIC target genes. However, on a global transcriptomic scale, IDH1-R132H mutation was found to dramatically reduce the total number of dysregulated genes in both *CIC* knockout and *ATXN1L* knockout cell lines suggesting that IDH1-R132H mutation may "dampen" the effects of CIC/ATXN1L loss through interaction with the epigenome.

In summary, the main contributions of this thesis for the field of oncology research are:

1. It provides further support of the tumour suppressor potential of CIC in several cancer types.

2. It establishes a reciprocal relationship between CIC and ATXN1/ATXN1L on a global transcriptomic level in mammalian cells and the role of the CIC-ATXN1/ATXN1L complex in regulating cellular pathways involved in the cell cycle.
3. It led to the discovery of TRIM25 as a novel, ERK independent, post-translational regulator of CIC protein expression and function.
4. It demonstrates that the regulation of CIC function and post-translational stability in mammalian cells is more intricate and complex than previously appreciated.

6.2 Study strengths and limitations

Many of the experiments in this thesis utilised immortalized normal cell lines, such as HEK and NHA, to investigate the normal function of CIC as a regulator of the cell cycle; and while immortalized cell lines may not be fully transformed, many of the genomic alterations and adaptations required for the establishment of these cell lines are known to affect pathways related to senescence and cell cycle. Cell lines are also not able to recapitulate the inter and intra tumoural heterogeneity of patient tumours. Therefore, the use of TCGA patient cohorts was an important validation of our *in vitro* observations.

In the cell lines used for this study, the majority displayed a sole reliance on ATXN1L for CIC protein expression, while in patient cohorts, transcriptomic analyses revealed a differential reliance on *ATXN1* and/or *ATXN1L* on CIC function. Further experiments using cell lines from different cellular contexts such as prostate adenocarcinoma and stomach adenocarcinoma as well as patient derived primary cell lines would have strengthened our *in vitro* and *in silico* observations had they been available. Unfortunately, the only primary cell lines available for these studies were glioma derived neurosphere cell lines which are non-adherent and slow growing, making them experimentally challenging. Had patient FFPE with matched genomic and transcriptomic profiles been available, further validation of the reliance of CIC expression on *ATXN1/ATXN1L* could have been performed using CIC IHC. Given these limitations, this study is strengthened by the consistency of our observations in several different cancer types suggesting that the mechanisms uncovered apply generally to CIC biology.

6.3 Future directions

The discoveries made in this study have generated several additional research avenues which could be pursued in the future to further our understanding of CIC biology and the

intricacy of CIC regulation both in normal cells and in cancer. Below are some future directions, in relation to this thesis, which may further our understanding of CIC biology and regulation:

6.3.1 Investigate the role of ATXN1/ATXN1L in relation to CIC isoforms

In this study and others, ATXN1 and ATXN1L were found to interact with both the short (CIC-S) and long (CIC-L) isoforms of CIC. However, it is unclear to what extent the functions and molecular mechanisms of CIC-S-ATXN1/ATXN1L and CIC-L-ATXN1/ATXN1L complexes differ. Studies thus far have been unable to differentiate the two isoforms or focus solely on the short isoform due to a lack of reagents which uniquely target only one isoform. CIC-L and CIC-S isoforms only differ at the first exon of each isoform which compounds this issue. Loss of *ATXN1L* in our *in vitro* experiments was found to affect the stability of CIC-S much more profoundly than CIC-L suggesting that there is differential regulation of each isoform. The two CIC isoforms have also found to localize differentially with CIC-S localizing to the both the nucleus and cytoplasm and CIC-L primarily localizing to the nucleus.

6.3.2 Investigate the role of ATXN1/ATXN1L in different CIC complexes

It is unclear whether all CIC proteins in the cell exist in a complex with ATXN1/ATXN1L or if there are ATXN1/ATXN1L independent mechanisms for CIC stability. CIC has also been shown to interact with several different protein complexes with various cellular functions such as the SIN3-HDAC repressive complex, the SWI/SNF chromatin remodeling complex, and mitochondrial ACLY involved in metabolism. In our study, CIC was not found to interact with these complexes in *ATXN1L* knockout cell lines. However, it is unknown whether ATXN1L is an important mediator which facilitates the assembly of these CIC complexes. The role or presence of ATXN1/ATXN1L in these CIC complexes is unknown and may provide further insight into the mechanisms of CIC activity.

6.3.3 Determine the amino acid residues of CIC required for degradation

While our study was able to identify a novel E3-ligase involved in CIC regulation, it was not able to identify the exact residues which are necessary for ubiquitination. Several other studies have also not been able to identify ubiquitination residues on CIC. So far, the only domain that has been identified to be important for CIC protein regulation is the ERK binding domain. However, it is unclear whether this domain is also required for ERK independent regulation of CIC. It will be important for future studies to identify additional domains and

residues required for CIC degradation which will provide further insight into our understanding of CIC protein regulation.

6.3.4 Explore the use of small molecule inhibitors to re-establish CIC function

Loss of function CIC mutations have now been identified in several different cancer types as a means of promoting more aggressive behaviors. Interestingly, in other cancer subtypes CIC dysregulation, through several mechanisms involving ERK and ATXN1L, rather than loss of function mutations, have been identified as a means to circumvent CIC activity. In these tumours, in theory, it may be possible to restore CIC function through the use of small molecular inhibitors. ERK inhibitors have been shown to be effective in reducing CIC phosphorylation and increasing the repression of CIC target genes. However, this mechanism requires the presence of ATXN1L which protects CIC from TRIM25 degradation. While TRIM25 small molecular inhibitors are currently not available, inhibition of the TRIM25 degradation pathway in conjunction with ERK may be a means to restore CIC activity and stability. Future research should identify the binding pockets required for CIC-TRIM25 interaction in order to design competitive small molecule inhibitors. Conversely, protein-protein interactor stabilizers could also be employed to strengthen the CIC-ATXN1L interaction as the interfaces that facilitate this interaction have already been mapped.

References

1. Bailey, P. and H. Cushing, *A classification of the tumours of the glioma group on a histogenetic basis, with a correlated study of prognosis. By Percival Bailey and Harvey Cushing. Medium 8vo. Pp. 175, with 108 illustrations. 1926. Philadelphia, London, and Montreal: J. B. Lippincott Company. 21s. net.* British Journal of Surgery, 1927. **14**(55): p. 554-555.
2. H.J., S., *Structural Development in Gliomas.* The American Journal of Cancer, 1938. **34**(3): p. 333-351.
3. Ostrom, Q.T., et al., *CBTRUS statistical report: Primary brain and central nervous system tumors diagnosed in the United States in 2006-2010.* Neuro Oncol, 2013. **15 Suppl 2**: p. ii1-56.
4. Suzuki, H., et al., *Mutational landscape and clonal architecture in grade II and III gliomas.* Nat Genet, 2015. **47**(5): p. 458-68.
5. Louis, D.N., et al., *The 2016 World Health Organization Classification of Tumors of the Central Nervous System: a summary.* Acta Neuropathol, 2016. **131**(6): p. 803-20.
6. Weller, M., et al., *Molecular classification of diffuse cerebral WHO grade II/III gliomas using genome- and transcriptome-wide profiling improves stratification of prognostically distinct patient groups.* Acta Neuropathol, 2015. **129**(5): p. 679-93.
7. Bettegowda, C., et al., *Mutations in CIC and FUBP1 contribute to human oligodendroglioma.* Science, 2011. **333**(6048): p. 1453-5.
8. Yip, S., et al., *Concurrent CIC mutations, IDH mutations, and 1p/19q loss distinguish oligodendrogliomas from other cancers.* J Pathol, 2012. **226**(1): p. 7-16.
9. Jenkins, R.B., et al., *A t(1;19)(q10;p10) mediates the combined deletions of 1p and 19q and predicts a better prognosis of patients with oligodendroglioma.* Cancer Res, 2006. **66**(20): p. 9852-61.
10. Griffin, C.A., et al., *Identification of der(1;19)(q10;p10) in five oligodendrogliomas suggests mechanism of concurrent 1p and 19q loss.* J Neuropathol Exp Neurol, 2006. **65**(10): p. 988-94.
11. Cancer Genome Atlas Research, N., et al., *Comprehensive, Integrative Genomic Analysis of Diffuse Lower-Grade Gliomas.* N Engl J Med, 2015. **372**(26): p. 2481-98.
12. Parsons, D.W., et al., *An integrated genomic analysis of human glioblastoma multiforme.* Science, 2008. **321**(5897): p. 1807-12.
13. Ward, P.S., et al., *The potential for isocitrate dehydrogenase mutations to produce 2-hydroxyglutarate depends on allele specificity and subcellular compartmentalization.* J Biol Chem, 2013. **288**(6): p. 3804-15.
14. Lu, C., et al., *IDH mutation impairs histone demethylation and results in a block to cell differentiation.* Nature, 2012. **483**(7390): p. 474-8.
15. Xu, W., et al., *Oncometabolite 2-hydroxyglutarate is a competitive inhibitor of alpha-ketoglutarate-dependent dioxygenases.* Cancer Cell, 2011. **19**(1): p. 17-30.
16. Chowdhury, R., et al., *The oncometabolite 2-hydroxyglutarate inhibits histone lysine demethylases.* EMBO Rep, 2011. **12**(5): p. 463-9.
17. Turcan, S., et al., *IDH1 mutation is sufficient to establish the glioma hypermethylator phenotype.* Nature, 2012. **483**(7390): p. 479-83.
18. Noushmehr, H., et al., *Identification of a CpG island methylator phenotype that defines a distinct subgroup of glioma.* Cancer Cell, 2010. **17**(5): p. 510-22.

19. Zhao, S., et al., *Glioma-derived mutations in IDH1 dominantly inhibit IDH1 catalytic activity and induce HIF-1alpha.* Science, 2009. **324**(5924): p. 261-5.
20. Lee, C.-J., et al., *CIC, a member of a novel subfamily of the HMG-box superfamily, is transiently expressed in developing granule neurons.* Mol Brain Res, 2002. **106**(1-2): p. 151-6.
21. Jin, Y., et al., *EGFR/Ras Signaling Controls Drosophila Intestinal Stem Cell Proliferation via Capicua-Regulated Genes.* PLoS Genet, 2015. **11**(12): p. e1005634.
22. Yang, L., et al., *Minibrain and Wings apart control organ growth and tissue patterning through down-regulation of Capicua.* Proc Natl Acad Sci U S A, 2016. **113**(38): p. 10583-8.
23. Jimenez, G., S.Y. Shvartsman, and Z. Paroush, *The Capicua repressor--a general sensor of RTK signaling in development and disease.* J Cell Sci, 2012. **125**(Pt 6): p. 1383-91.
24. Roch, F., G. Jiménez, and J. Casanova, *EGFR signalling inhibits Capicua-dependent repression during specification of Drosophila wing veins.* Development, 2002. **129**: p. 992-1002.
25. Jime´nez, G., et al., *Relief of gene repression by Torso RTK signaling: role of capicua in Drosophila terminal and dorsoventral patterning.* Genes & Development, 2000. **14**: p. 224-231.
26. Astigarraga, S., et al., *A MAPK docking site is critical for downregulation of Capicua by Torso and EGFR RTK signaling.* EMBO J, 2007. **26**(3): p. 668-77.
27. Tseng, A.S., et al., *Capicua regulates cell proliferation downstream of the receptor tyrosine kinase/ras signaling pathway.* Curr Biol, 2007. **17**(8): p. 728-33.
28. LeBlanc, V.G., et al., *Comparative transcriptome analysis of isogenic cell line models and primary cancers links capicua (CIC) loss to activation of the MAPK signalling cascade.* J Pathol, 2017.
29. Wang, B., et al., *ATXN1L, CIC, and ETS Transcription Factors Modulate Sensitivity to MAPK Pathway Inhibition.* Cell Rep, 2017. **18**(6): p. 1543-1557.
30. Padul, V., et al., *ETV/Pea3 family transcription factor-encoding genes are overexpressed in CIC-mutant oligodendrogliomas.* Genes Chromosomes Cancer, 2015. **54**(12): p. 725-33.
31. Okimoto, R.A., et al., *Inactivation of Capicua drives cancer metastasis.* Nat Genet, 2016.
32. Specht, K., et al., *Distinct transcriptional signature and immunoprofile of CIC-DUX4 fusion-positive round cell tumors compared to EWSR1-rearranged Ewing sarcomas: further evidence toward distinct pathologic entities.* Genes Chromosomes Cancer, 2014. **53**(7): p. 622-33.
33. Kim, E., et al., *Capicua suppresses hepatocellular carcinoma progression by controlling ETV4-MMP1 axis.* Hepatology, 2017.
34. Gleize, V., et al., *CIC inactivating mutations identify aggressive subset of 1p19q codeleted gliomas.* Ann Neurol, 2015. **78**(3): p. 355-74.
35. Liao, S., et al., *A genetic interaction analysis identifies cancer drivers that modify EGFR dependency.* Genes Dev, 2017.
36. Kawamura-Saito, M., et al., *Fusion between CIC and DUX4 up-regulates PEA3 family genes in Ewing-like sarcomas with t(4;19)(q35;q13) translocation.* Hum Mol Genet, 2006. **15**(13): p. 2125-37.
37. Brohl, A.S., et al., *The genomic landscape of the Ewing Sarcoma family of tumors reveals recurrent STAG2 mutation.* PLoS Genet, 2014. **10**(7): p. e1004475.

38. Sugita, S., et al., *A novel CIC-FOXO4 gene fusion in undifferentiated small round cell sarcoma: a genetically distinct variant of Ewing-like sarcoma.* Am J Surg Pathol, 2014. **38**(11): p. 1571-6.
39. Sturm, D., et al., *New Brain Tumor Entities Emerge from Molecular Classification of CNS-PNETs.* Cell, 2016. **164**(5): p. 1060-1072.
40. Le Loarer, F., et al., *Clinicopathologic Features of CIC-NUTM1 Sarcomas, a New Molecular Variant of the Family of CIC-Fused Sarcomas.* Am J Surg Pathol, 2019. **43**(2): p. 268-276.
41. Huang, S.-C., et al., *Recurrent CIC Gene Abnormalities in Angiosarcomas A Molecular Study of 120 Cases With Concurrent Investigation of PLCG1, KDR, MYC, and FLT4 Gene Alterations.* Am J Surg Pathol, 2016. **40**: p. 645-655.
42. Siegfried, A., et al., *Brain tumor with an ATXN1-NUTM1 fusion gene expands the histologic spectrum of NUTM1-rearranged neoplasia.* Acta Neuropathol Commun, 2019. **7**(1): p. 220.
43. Italiano, A., et al., *High prevalence of CIC fusion with double-homeobox (DUX4) transcription factors in EWSR1-negative undifferentiated small blue round cell sarcomas.* Genes Chromosomes Cancer, 2012. **51**(3): p. 207-18.
44. Sjoblom, T., et al., *The consensus coding sequences of human breast and colorectal cancers.* Science, 2006. **314**(5797): p. 268-74.
45. Oliveira, D.M., et al., *Identification of different mutational profiles in cancers arising in specific colon segments by next generation sequencing.* Oncotarget, 2018. **9**(35): p. 23960-23974.
46. Van Allen, E.M., et al., *The genetic landscape of clinical resistance to RAF inhibition in metastatic melanoma.* Cancer Discov, 2014. **4**(1): p. 94-109.
47. Da Via, M.C., et al., *CIC Mutation as a Molecular Mechanism of Acquired Resistance to Combined BRAF-MEK Inhibition in Extramedullary Multiple Myeloma with Central Nervous System Involvement.* Oncologist, 2019.
48. Barthel, F.P., et al., *Longitudinal molecular trajectories of diffuse glioma in adults.* Nature, 2019. **576**(7785): p. 112-120.
49. Sahm, F., et al., *CIC and FUBP1 mutations in oligodendrogliomas, oligoastrocytomas and astrocytomas.* Acta Neuropathol, 2012. **123**(6): p. 853-60.
50. Chan, A.K., et al., *Loss of CIC and FUBP1 expressions are potential markers of shorter time to recurrence in oligodendroglial tumors.* Mod Pathol, 2014. **27**(3): p. 332-42.
51. Han, F., et al., *Altered capicua transcriptional repressor gene expression exhibits distinct prognostic value for isocitrate dehydrogenase-mutant oligodendroglial tumors.* Oncology Letters, 2017.
52. Simon-Carrasco, L., et al., *Inactivation of Capicua in adult mice causes T-cell lymphoblastic lymphoma.* Genes Dev, 2017. **31**(14): p. 1456-1468.
53. Chittaranjan, S., et al., *Mutations in CIC and IDH1 Cooperatively Regulate 2-hydroxyglutarate levels and cell clonogenicity.* Oncotarget, 2014. **5**(17).
54. Wong, D., et al., *Transcriptomic analysis of CIC and ATXN1L reveal a functional relationship exploited by cancer.* Oncogene, 2018.
55. Fransson, S., et al., *Estimation of copy number aberrations: Comparison of exome sequencing data with SNP microarrays identifies homozygous deletions of 19q13.2 and CIC in neuroblastoma.* Int J Oncol, 2016. **48**(3): p. 1103-16.
56. Choi, N., et al., *miR-93/miR-106b/miR-375-CIC-CRABP1: a novel regulatory axis in prostate cancer progression.* Oncotarget, 2015. **6**(27): p. 23533-47.

57. Bunda, S., et al., *CIC protein instability contributes to tumorigenesis in glioblastoma.* Nat Commun, 2019. **10**(1): p. 661.
58. Tanaka, M., T. Yoshimoto, and T. Nakamura, *A double-edged sword: The world according to Capicua in cancer.* Cancer Sci, 2017. **108**(12): p. 2319-2325.
59. Lu, H.C., et al., *Disruption of the ATXN1-CIC complex causes a spectrum of neurobehavioral phenotypes in mice and humans.* Nat Genet, 2017.
60. Ahmad, S.T., et al., *Capicua regulates neural stem cell proliferation and lineage specification through control of Ets factors.* Nat Commun, 2019. **10**(1): p. 2000.
61. Hwang, I., et al., *CIC is a Critical Regulator of Neuronal Differentiation.* 2019.
62. Yang, R., et al., *Cic Loss Promotes Gliomagenesis via Aberrant Neural Stem Cell Proliferation and Differentiation.* Cancer Res, 2017. **77**(22): p. 6097-6108.
63. Watanabe, T., et al., *IDH1 mutations are early events in the development of astrocytomas and oligodendrogliomas.* Am J Pathol, 2009. **174**(4): p. 1149-53.
64. Tirosh, I., et al., *Single-cell RNA-seq supports a developmental hierarchy in human oligodendroglioma.* Nature, 2016.
65. Lee, Y., et al., *ATXN1 protein family and CIC regulate extracellular matrix remodeling and lung alveolarization.* Dev Cell, 2011. **21**(4): p. 746-57.
66. Kim, E., et al., *Deficiency of Capicua disrupts bile acid homeostasis.* Sci Rep, 2015. **5**: p. 8272.
67. Park, S., et al., *The Capicua/ETS Translocation Variant 5 Axis Regulates Liver-Resident Memory CD8(+) T-Cell Development and the Pathogenesis of Liver Injury.* Hepatology, 2019. **70**(1): p. 358-371.
68. Tan, Q., et al., *Loss of Capicua alters early T cell development and predisposes mice to T cell lymphoblastic leukemia/lymphoma.* Proc Natl Acad Sci U S A, 2018.
69. Lam, Y.C., et al., *ATAXIN-1 interacts with the repressor Capicua in its native complex to cause SCA1 neuropathology.* Cell, 2006. **127**(7): p. 1335-47.
70. Crespo-Barreto, J., et al., *Partial loss of ataxin-1 function contributes to transcriptional dysregulation in spinocerebellar ataxia type 1 pathogenesis.* PLoS Genet, 2010. **6**(7): p. e1001021.
71. Rousseaux, M.W.C., et al., *ATXN1-CIC Complex Is the Primary Driver of Cerebellar Pathology in Spinocerebellar Ataxia Type 1 through a Gain-of-Function Mechanism.* Neuron, 2018. **97**(6): p. 1235-1243 e5.
72. Bowman, A.B., et al., *Duplication of Atxn1l suppresses SCA1 neuropathology by decreasing incorporation of polyglutamine-expanded ataxin-1 into native complexes.* Nat Genet, 2007. **39**(3): p. 373-9.
73. A, M., et al., *Boat, an AXH domain protein, suppresses the cytotoxicity of mutant ataxin-1.* EMBO J, 2005. **24**(18).
74. de Chiara, C., et al., *The AXH module: an independently folded domain common to ataxin-1 and HBP1.* FEBS Letters, 2003. **551**(1-3): p. 107-112.
75. Tong, X., et al., *Ataxin-1 and Brother of ataxin-1 are components of the Notch signalling pathway.* EMBO Rep, 2011. **12**(5): p. 428-35.
76. Kahle, J.J., et al., *Ataxin1L is a regulator of HSC function highlighting the utility of cross-tissue comparisons for gene discovery.* PLoS Genet, 2013. **9**(3): p. e1003359.
77. Sonoda, Y., et al., *Formation of intracranial tumors by genetically modified human astrocytes defines four pathways critical in the development of human anaplastic astrocytoma.* Cancer Res, 2001. **61**(13): p. 4956-60.
78. Oyama, R., et al., *Generation of novel patient-derived CIC- DUX4 sarcoma xenografts and cell lines.* Sci Rep, 2017. **7**(1): p. 4712.

79. Wakimoto, H., et al., *Targetable signaling pathway mutations are associated with malignant phenotype in IDH-mutant gliomas.* Clin Cancer Res, 2014. **20**(11): p. 2898-909.
80. Luchman, H.A., et al., *An in vivo patient-derived model of endogenous IDH1-mutant glioma.* Neuro Oncol, 2012. **14**(2): p. 184-91.
81. Dalman, M.R., et al., *Fold change and p-value cutoffs significantly alter microarray interpretations.* BMC Bioinformatics, 2012. **13**.
82. Cerami, E., et al., *The cBio cancer genomics portal: an open platform for exploring multidimensional cancer genomics data.* Cancer Discov, 2012. **2**(5): p. 401-4.
83. Gao, J.J., et al., *Integrative Analysis of Complex Cancer Genomics and Clinical Profiles Using the cBioPortal.* Science Signaling, 2013. **6**(269).
84. Love, M.I., W. Huber, and S. Anders, *Moderated estimation of fold change and dispersion for RNA-seq data with DESeq2.* Genome Biol, 2014. **15**(12): p. 550.
85. Eisenreich, S., et al., *Novel CIC point mutations and an exon-spanning, homozygous deletion identified in oligodendroglial tumors by a comprehensive genomic approach including transcriptome sequencing.* PLoS One, 2013. **8**(9): p. e76623.
86. Tripathi, S., et al., *Meta- and Orthogonal Integration of Influenza "OMICs" Data Defines a Role for UBR4 in Virus Budding.* Cell Host Microbe, 2015. **18**(6): p. 723-35.
87. Kosugi, S., et al., *Systematic identification of cell cycle-dependent yeast nucleocytoplasmic shuttling proteins by prediction of composite motifs.* Proc Natl Acad Sci U S A, 2009. **106**(25): p. 10171-6.
88. Chen, Z., et al., *hCKSAAP_UbSite: improved prediction of human ubiquitination sites by exploiting amino acid pattern and properties.* Biochim Biophys Acta, 2013. **1834**(8): p. 1461-7.
89. Dobin, A., et al., *STAR: ultrafast universal RNA-seq aligner.* Bioinformatics, 2013. **29**(1): p. 15-21.
90. Trapnell, C., et al., *Transcript assembly and quantification by RNA-Seq reveals unannotated transcripts and isoform switching during cell differentiation.* Nat Biotechnol, 2010. **28**(5): p. 511-5.
91. Hughes, C.S., et al., *Ultrasensitive proteome analysis using paramagnetic bead technology.* Mol Syst Biol, 2014. **10**: p. 757.
92. Tabb, D.L., *The SEQUEST family tree.* J Am Soc Mass Spectrom, 2015. **26**(11): p. 1814-9.
93. The, M., et al., *Fast and Accurate Protein False Discovery Rates on Large-Scale Proteomics Data Sets with Percolator 3.0.* J Am Soc Mass Spectrom, 2016. **27**(11): p. 1719-1727.
94. Tyanova, S. and J. Cox, *Perseus: A Bioinformatics Platform for Integrative Analysis of Proteomics Data in Cancer Research.* Methods Mol Biol, 2018. **1711**: p. 133-148.
95. Walsh, L.A., et al., *An Integrated Systems Biology Approach Identifies TRIM25 as a Key Determinant of Breast Cancer Metastasis.* Cell Rep, 2017. **20**(7): p. 1623-1640.
96. Seim, I., et al., *Whole-Genome Sequence of the Metastatic PC3 and LNCaP Human Prostate Cancer Cell Lines.* G3 (Bethesda), 2017.
97. Post, G.R. and G. Dawson, *Characterization of a cell line derived from a human oligodendroglioma.* Mol Chem Neuropathol, 1992. **16**(3): p. 303-17.
98. Cong, L., et al., *Multiplex genome engineering using CRISPR/Cas systems.* Science, 2013. **339**(6121): p. 819-23.
99. Mali, P., et al., *RNA-guided human genome engineering via Cas9.* Science, 2013. **339**(6121): p. 823-6.

100. N, C., et al., *miR-93_miR-106b_miR-375-CIC-CRABP1 a novel regulatory axis in prostate cancer progression.* oncotarget, 2015. **6**(27).
101. Cancer Genome Atlas Research, N., *Comprehensive molecular characterization of gastric adenocarcinoma.* Nature, 2014. **513**(7517): p. 202-9.
102. Kim, E., et al., *Structural basis of protein complex formation and reconfiguration by polyglutamine disease protein Ataxin-1 and Capicua.* Genes Dev, 2013. **27**(6): p. 590-5.
103. Iglesias-Ara, A., et al., *E2F1 and E2F2 prevent replicative stress and subsequent p53-dependent organ involution.* Cell Death Differ, 2015. **22**(10): p. 1577-89.
104. Huang, L., et al., *DEPDC1 promotes cell proliferation and tumor growth via activation of E2F signaling in prostate cancer.* Biochem Biophys Res Commun, 2017.
105. Crosby, M.E. and A. Almasan, *Opposing Roles of E2Fs in Cell Proliferation and Death.* Cancer Biol Ther, 2004. **3**(12).
106. Chen, H.Z., S.Y. Tsai, and G. Leone, *Emerging roles of E2Fs in cancer: an exit from cell cycle control.* Nat Rev Cancer, 2009. **9**(11): p. 785-97.
107. Alonso, M.M., et al., *E2F1 in gliomas: a paradigm of oncogene addiction.* Cancer Lett, 2008. **263**(2): p. 157-63.
108. Muller, M., et al., *The role of pluripotency factors to drive stemness in gastrointestinal cancer.* Stem Cell Res, 2016. **16**(2): p. 349-57.
109. Dalerba, P., et al., *Single-cell dissection of transcriptional heterogeneity in human colon tumors.* Nat Biotechnol, 2011. **29**(12): p. 1120-7.
110. Goukassian, D., et al., *Inhibition of the cyclin D1/E2F pathway by PCA-4230, a potent repressor of cellular proliferation.* Br J Pharmacol, 2001. **132**(7): p. 1597-605.
111. Johnson, J., et al., *Targeting the RB-E2F pathway in breast cancer.* Oncogene, 2016. **35**(37): p. 4829-35.
112. Valk-Lingbeek, M.E., S.W. Bruggeman, and M. van Lohuizen, *Stem cells and cancer; the polycomb connection.* Cell, 2004. **118**(4): p. 409-18.
113. Pasini, D., A.P. Bracken, and K. Helin, *Polycomb Group Proteins in Cell Cycle Progression and Cancer.* Cell Cycle, 2014. **3**(4): p. 394-398.
114. Bracken, A.P., et al., *Genome-wide mapping of Polycomb target genes unravels their roles in cell fate transitions.* Genes Dev, 2006. **20**(9): p. 1123-36.
115. Barford, D., A.K. Das, and M.P. Egloff, *The structure and mechanism of protein phosphatases: Insights into catalysis and regulation.* Annual Review of Biophysics and Biomolecular Structure, 1998. **27**: p. 133-164.
116. Dissanayake, K., et al., *ERK/p90(RSK)/14-3-3 signalling has an impact on expression of PEA3 Ets transcription factors via the transcriptional repressor capicua.* Biochem J, 2011. **433**(3): p. 515-25.
117. Chittaranjan, S., et al., *Loss of CIC promotes mitotic dysregulation and chromosome segregation defects.* 2019.
118. Weissmann, S., et al., *The tumor suppressor CIC directly regulates MAPK pathway genes via histone deacetylation.* Cancer Res, 2018.
119. Hwang, I., et al., *CIC is a critical regulator of neuronal differentiation.* JCI Insight, 2020. **5**(9).
120. Hashiba, T., et al., *Inactivation of Transcriptional Repressor Capicua Confers Sorafenib Resistance in Human Hepatocellular Carcinoma.* Cell Mol Gastroenterol Hepatol, 2020.
121. Unni, A.M., et al., *Hyperactivation of ERK by multiple mechanisms is toxic to RTK-RAS mutation-driven lung adenocarcinoma cells.* Elife, 2018. **7**.
122. Gack, M.U., et al., *TRIM25 RING-finger E3 ubiquitin ligase is essential for RIG-I-mediated antiviral activity.* Nature, 2007. **446**(7138): p. 916-920.

123. Hage, A. and R. Rajsbaum, *To TRIM or not to TRIM: the balance of host-virus interactions mediated by the ubiquitin system.* J Gen Virol, 2019.
124. Yoe, J., et al., *Capicua restricts cancer stem cell-like properties in breast cancer cells.* Oncogene, 2020.
125. Zhang, Q., et al., *The MAP3K13-TRIM25-FBXW7alpha axis affects c-Myc protein stability and tumor development.* Cell Death Differ, 2019.
126. Qin, Y., H. Cui, and H. Zhang, *Overexpression of TRIM25 in Lung Cancer Regulates Tumor Cell Progression.* Technol Cancer Res Treat, 2016. **15**(5): p. 707-15.
127. Takayama, K.I., et al., *TRIM25 enhances cell growth and cell survival by modulating p53 signals via interaction with G3BP2 in prostate cancer.* Oncogene, 2018. **37**(16): p. 2165-2180.
128. Wang, Z., et al., *Blockade of miR-3614 maturation by IGF2BP3 increases TRIM25 expression and promotes breast cancer cell proliferation.* EBioMedicine, 2019. **41**: p. 357-369.
129. Han, J., et al., *Genome-wide CRISPR/Cas9 Screen Identifies Host Factors Essential for Influenza Virus Replication.* Cell Rep, 2018. **23**(2): p. 596-607.
130. Yan, H., et al., *IDH1 and IDH2 mutations in gliomas.* N Engl J Med, 2009. **360**(8): p. 765-73.
131. Dang, L., et al., *Cancer-associated IDH1 mutations produce 2-hydroxyglutarate.* Nature, 2009. **462**(7274): p. 739-44.
132. Aihara, K., et al., *Genetic and epigenetic stability of oligodendrogliomas at recurrence.* Acta Neuropathol Commun, 2017. **5**(1): p. 18.
133. Mazor, T., et al., *Clonal expansion and epigenetic reprogramming following deletion or amplification of mutant IDH1.* Proc Natl Acad Sci U S A, 2017. **114**(40): p. 10743-10748.
134. Sasaki, M., et al., *IDH1(R132H) mutation increases murine haematopoietic progenitors and alters epigenetics.* Nature, 2012. **488**(7413): p. 656-9.

Appendices

Appendix A

This appendix lists all of the publications I contributed to during my PhD studies. First or co-first authorships are underlined

1. **Derek Wong**, Samantha S Lee, Lisa Sogerer, Victor Wong, Amy Lum, Marco A Marra, Stephen Yip. (2020) Loss of ATXN1L promotes ERK independent proteasomal degradation of Capicua through TRIM25 in cancer. *BMC Biology*. 18 (154)
2. Adrian B. Levine, **Derek Wong**, Mostafa Fatehi, Stephen Yip. (2020) Ependymoma and Chordoma. *Neurosurgery*. doi:10.1093/neuros/nyaa329
3. **Derek Wong**, Stephen Yip (2020) Making heads or tails – The emergence of *Capicua* in cancer. *The Journal of Pathology*. 250 (5), 532-540
4. **Derek Wong**, Stephen Yip (2019) Finding a four-leaf clover—identifying long-term survivors in IDH-wildtype glioblastoma. *Neuro-oncology*. 21 (11), 1352-1353
5. Nisreen Mohammad, **Derek Wong**, Amy Lum, Jonah Lin, Julie Ho, Cheng-han Lee, Tony Ng, Stephen Yip. (2019) Characterization of IDH1/IDH2 Mutations and D-2-Hydroxyglutarate Oncometabolite Level in Dedifferentiated Chondrosarcoma. *American Journal of Surgical Pathology*. doi:10.1111/his.14018
6. **Derek Wong**, Stephen Yip, and Poul Sorensen. (2019) Methods for identifying patients with tropomyosin receptor kinase (TRK) fusion cancer. *Pathology and Oncology Research*. doi:10.1007/s12253-019-00685-2
7. **Derek Wong**, Yaoqing Shen, Erin Pleasance, Adrian Levine, Martin Jones, Brian Thiessen, Brian Toyota, Janessa Laskins, Steve Jones, Marco Marra, Stephen Yip. The Pivotal Role of Sampling Recurrent Tumors in the Precision Care of Patients with Tumors of the Central Nervous System. (2019) *Molecular Case Studies*. **5**: a004143
8. **Derek Wong,** Stephen Yip (2019) Chapter 6 - Pathology of Primary Brain Tumors – Gliomas. In Kaisorn Chaichana and Alfredo Quiñones-Hinojosa, Comprehensive Overview of Modern Surgical Approaches to Intrinsic Brain Tumors. Pages 121-137
9. Patel N, Wang J, Shiozawa K, Jones KB, Zhang Y, Prokop JW, Davenport GG, Nihira NT, Hao Z, **Wong D**, Brandsmeier L, Meadows SK, Sampaio AV, Werff RV, Endo M, Capecchi MR, McNagny KM, Mak TW, Nielsen TO, Underhill TM, Myers RM, Kondo T, Su L

(2019) HDAC2 regulates site-specific acetylation of MDM2 and its ubiquitination signaling in tumor suppression. *iScience*. 13, 43-54.

10. **Derek Wong**, Kohl Lounsbury, Amy Lum, Jungeun Song, Susanna Chan, Veronique LeBlanc, Suganthi Chittaranjan, Marco Marra, Stephen Yip (2018) Transcriptomic analysis of CIC and ATXN1L reveal a functional relationship exploited by cancer. *Oncogene*. 38(2):273-290.
11. **Derek Wong** and Stephen Yip (2018) Machine learning classifies cancer. *Nature*. 555, 446-447.

Appendix B

Supplemental Figure 1 – CIC-ATXN1L interaction

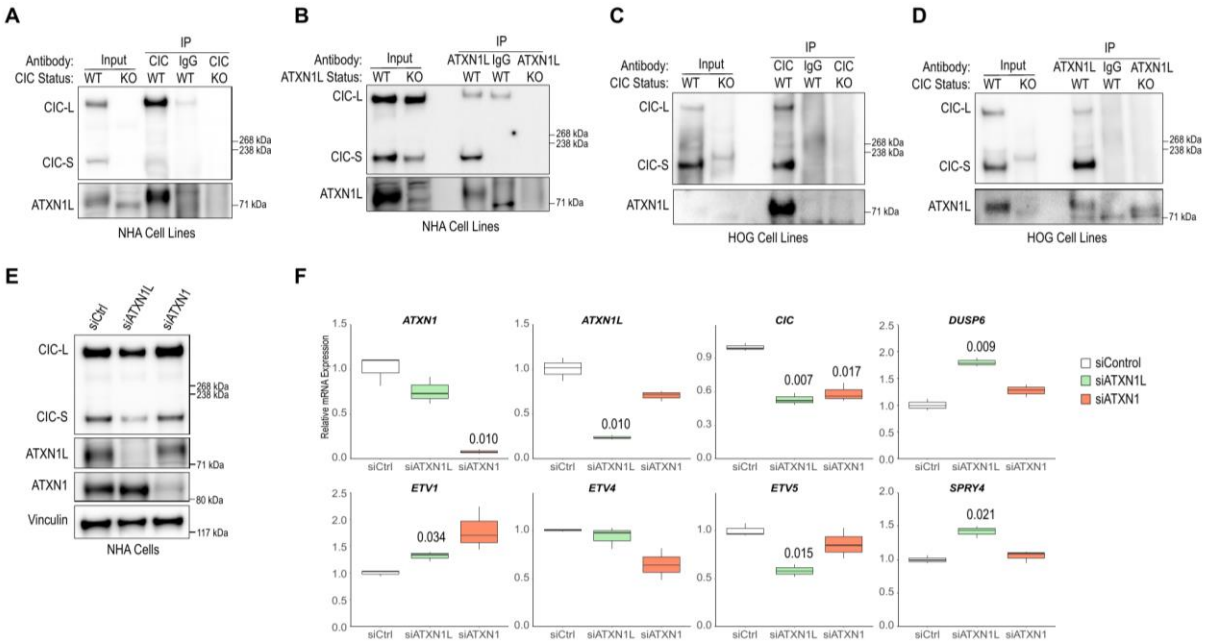

(A) Representative western blot of endogenous CIC IP showing co-IP of ATXN1L in NHA cells. A CIC IP in a *CIC*^{KO} cell line (A2) and an IgG IP in the parental NHA were performed as negative controls. (B) Representative western blot of endogenous ATXN1L IP showing co-IP of CIC in NHA cells. An ATXN1L IP in our *ATXN1L*^{KO} cell line (B82) and IgG IP in the parental NHA were performed as negative controls. (C) Representative western blot of endogenous CIC IP showing co-IP of ATXN1L in HOG cells. A CIC IP in a *CIC*^{KO} cell line (F11) and an IgG IP in the parental HOG were performed as negative controls. (D) Representative western blot of endogenous ATXN1L IP showing co-IP of CIC in HOG cells. An ATXN1L IP in our *CIC*^{KO} cell line (F11) and IgG IP in the parental HOG were performed as negative controls. (E) Representative western blot of *ATXN1L* and *ATXN1* knockdown using targeted siRNA in NHA cells. A scrambled siRNA (siCtrl) was used as a negative control and vinculin was used as a loading control. (F) Tukey boxplots showing relative mRNA transcript levels of *ATXN1L*, *ATXN1*, *CIC*, and CIC target genes *ETV1/4/5*, *DUSP6* and *SPRY4* measured by RT-qPCR following independent siRNA knockdown of *ATXN1L* or *ATXN1* for 48 hours. Data were collected from 3 independent experiments and p-values were calculated using the two-tailed independent Student's t-test comparing siATXN1L and siATXN1 to siCtrl.

Supplemental Figure 2 – ATXN1 function only partially compensates for ATXN1L loss.

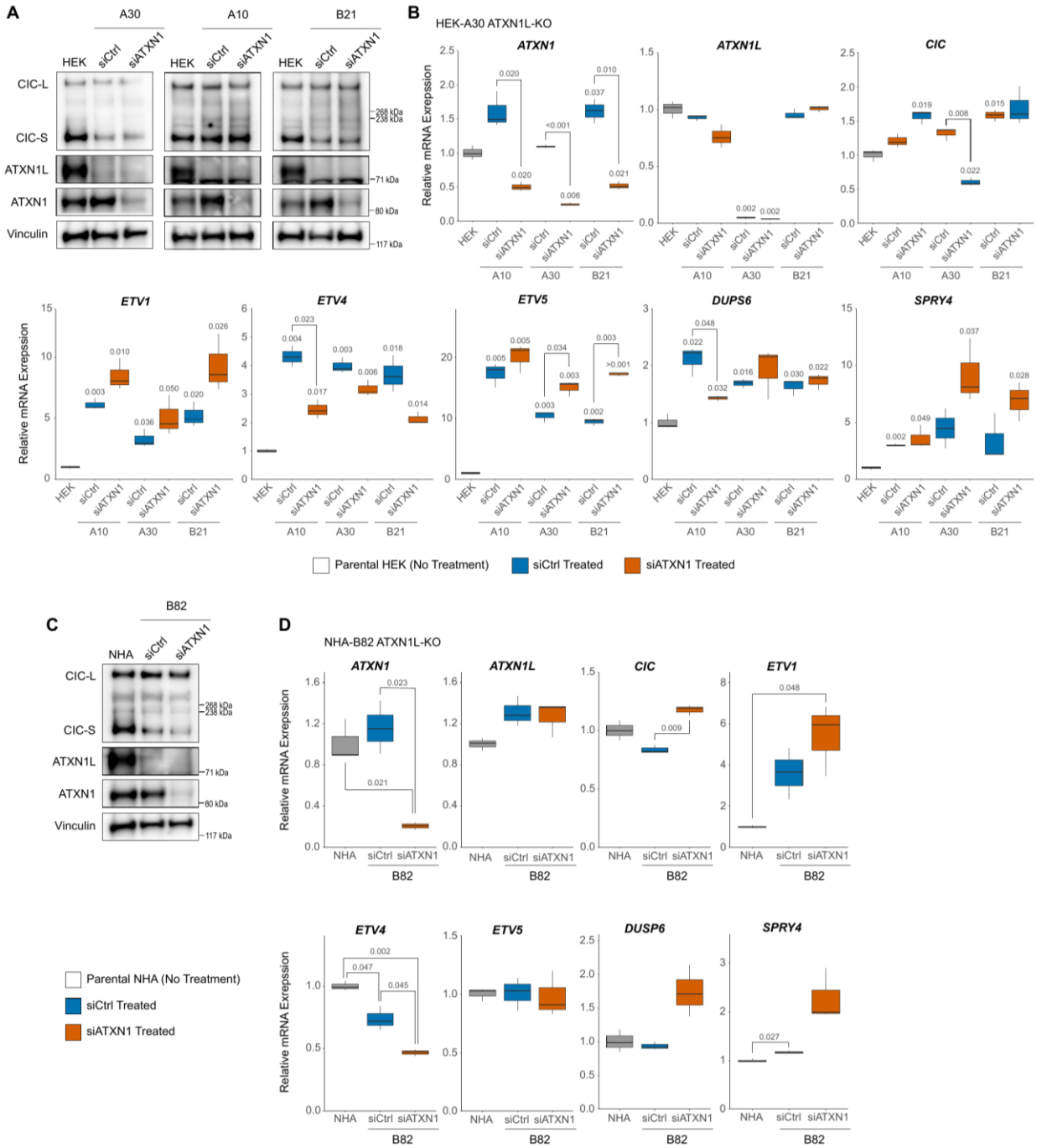

(A) Representative western blot of *ATXN1* knockdown using targeted siRNA in *ATXN1L*^{KO} HEK-A30, A10, and B21 cells. A scrambled siRNA (siCtrl) was used as a negative control and vinculin was used as a loading control. (B) Tukey boxplots showing relative mRNA transcript levels of *ATXN1L*, *ATXN1*, *CIC*, and CIC target genes *ETV1/4/5*, *DUSP6* and *SPRY4* measured by RT-qPCR following siRNA knockdown of *ATXN1* for 48 hours in *ATXN1L*^{KO} HEK-A10, A30, and B21 cells. Data were collected from 3 independent experiments and p-values were calculated using the two-tailed independent Student's t-test. p-values directly above each boxplot are referenced to the no treatment parental cell line. All other p-values represent t-tests compared to siCtrl. (C) Representative western blot of *ATXN1* knockdown using targeted siRNA in *ATXN1L*^{KO} NHA-B82 cells. A scrambled siRNA (siCtrl) was used as a negative control and vinculin was used as a loading control. (D) Tukey boxplots showing relative mRNA transcript levels of *ATXN1L*, *ATXN1*, *CIC*, and CIC target genes *ETV1/4/5*, *DUSP6* and *SPRY4* measured by RT-

qPCR following siRNA knockdown of ATXN1 for 48 hours in *ATXN1L*^{KO} NHA-B82 cells. Data were collected from 3 independent experiments and p-values were calculated using the two-tailed independent Student's t-test.

Supplemental Figure 3 – ATXN1L loss leads to decreased CIC protein expression

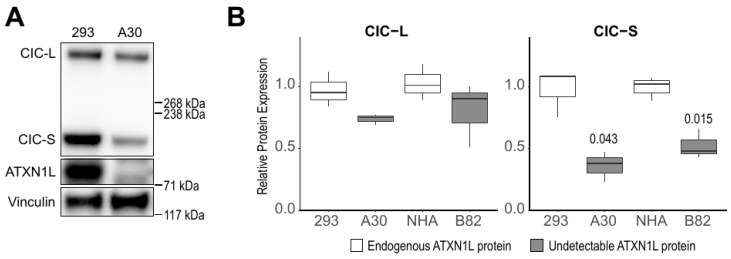

(A) Representative western blot showing decreased CIC protein expression in *ATXN1L*^{KO} cell line HEK-A30. Vinculin was blotted as a loading control. (B) Protein quantification of CIC-S and CIC-L protein expression in the parental HEK and NHA, and *ATXN1L*^{KO} cell lines HEK-A30 and NHA-B82. Values were normalized to the loading control Vinculin and their respective parental *ATXN1L*^{WT} cell lines. Data were collected from 3 independent experiments (passages) and p-values were calculated using the two tailed independent Student's t-test comparing *ATXN1L*^{KO} cell lines to their respective parental cell line.

Supplemental Figure 4 – Reintroduction of ATXN1L

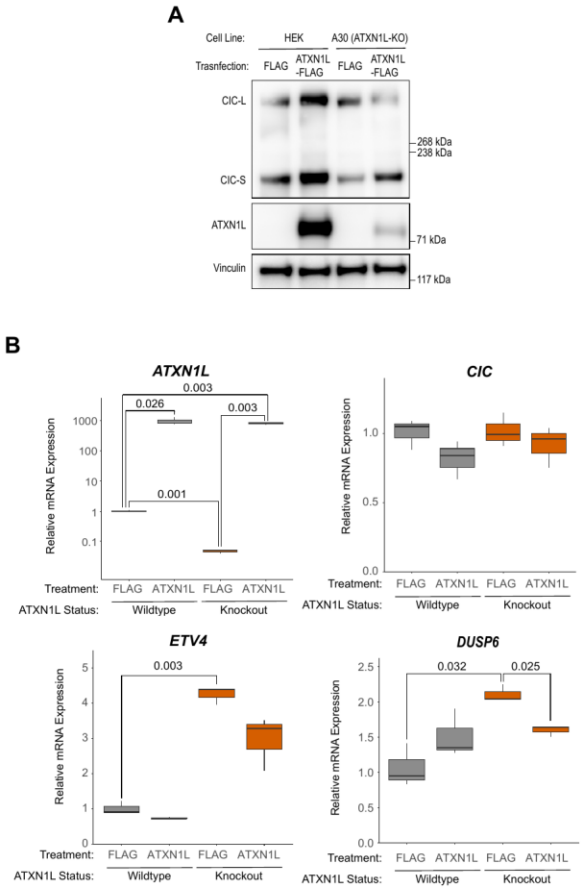

(A) Representative western blots showing introduction of ATXN1L-FLAG into the parental HEK and *ATXN1L*^{KO} HEK-A30 cell line. Vinculin was used as a loading control. (B) Tukey boxplots showing relative mRNA transcript levels of *ATXN1L*, *CIC*, and CIC target genes *ETV4* and *DUSP6* following introduction of FLAG or ATXN1L-FLAG constructs into the parental HEK and *ATXN1L*^{KO} HEK-A30 cell lines for 48 hours. Data were collected from 3 independent experiments and p-values were calculated using the two-tailed independent Student's t-test. Note: the y-axis on the ATXN1L plot is shown as log-scale.

Supplemental Figure 5 - *ATXN1L*^{KO} cell lines show derepression of the MAPK pathway.

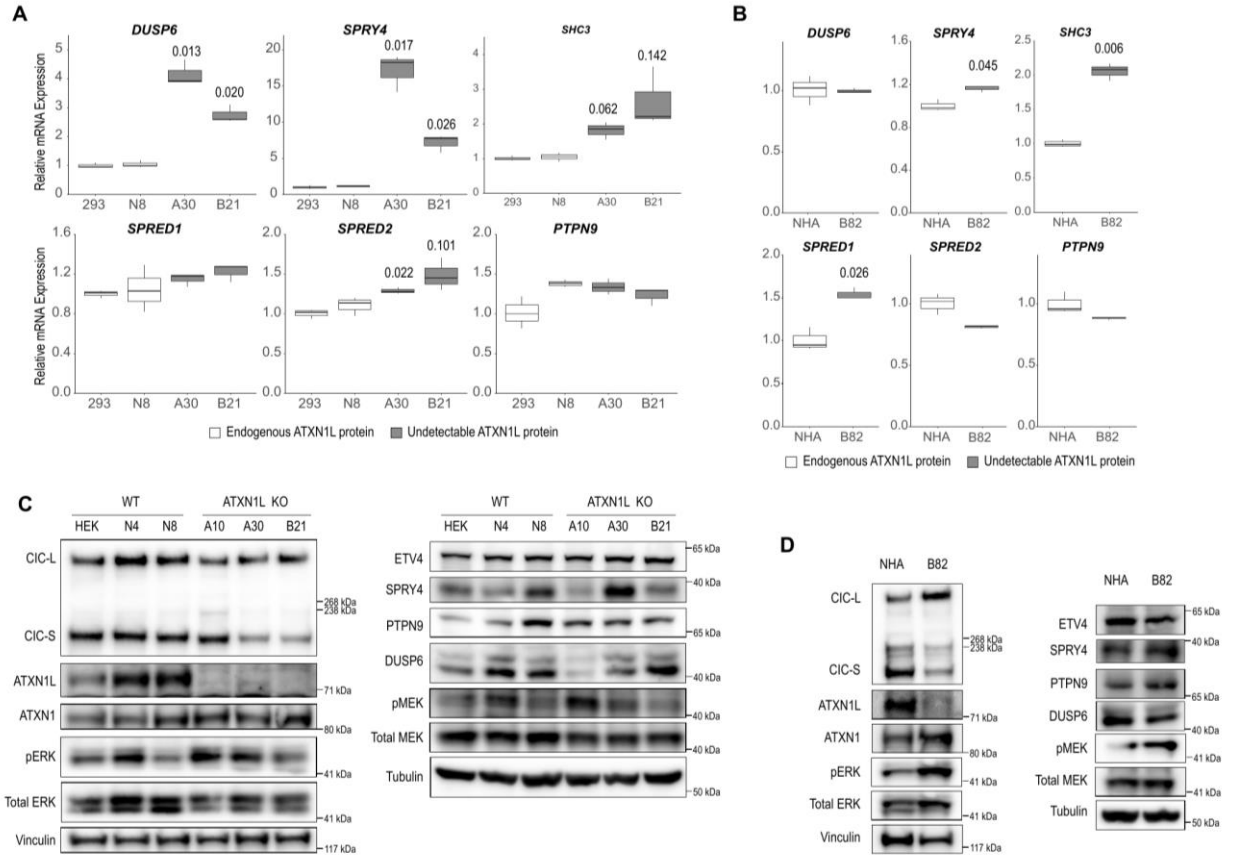

(A) Tukey boxplots showing relative mRNA transcript levels of genes downstream of MAPK activation (*DUSP6, SPRY4, SHC3, SPRED1, SPRED2, PTPN9*) measured by RT-qPCR in *ATXN1L*^{WT} (HEK, N8) and *ATXN1L*^{KO} (A30, B21) cell lines. Data were collected from 3 independent experiments and p-values were calculated using the two-tailed independent Student's t-test comparing isogenic cell lines (N8, A30, B21) to the parental HEK cell line. (B) Tukey boxplots showing relative mRNA transcript levels of genes downstream of MAPK activation (*DUSP6, SPRY4, SHC3, SPRED1, SPRED2, PTPN9*) measured by RT-qPCR in *ATXN1L*^{WT} (NHA) and *ATXN1L*^{KO} (B82) cell lines. Data were collected from 3 independent experiments and p-values were calculated using the two-tailed independent Student's t-test comparing isogenic cell lines (N8, A30, B21) to the parental HEK cell line. (C) Representative western blots showing protein expression of ATXN1, ETV4, and genes downstream of MAPK activation (PTPN9, DUSP6, SPRY4, pMEK, MEK, pERK, ERK) in *ATXN1L*^{WT} (HEK, N4, N8) and *ATXN1L*^{KO} (A10, A30, B21) cell lines. Tubulin and Vinculin were used as loading controls. (D) Representative western blots showing protein expression of ATXN1, ETV4, and genes downstream of MAPK activation (PTPN9, DUSP6, SPRY4, pMEK, MEK, pERK, ERK) in ATXN1LWT (NHA) and ATXN1LKO (B82) cell lines. Tubulin and Vinculin were used as loading controls.

Supplemental Figure 6 – TCGA Pathway Analyses

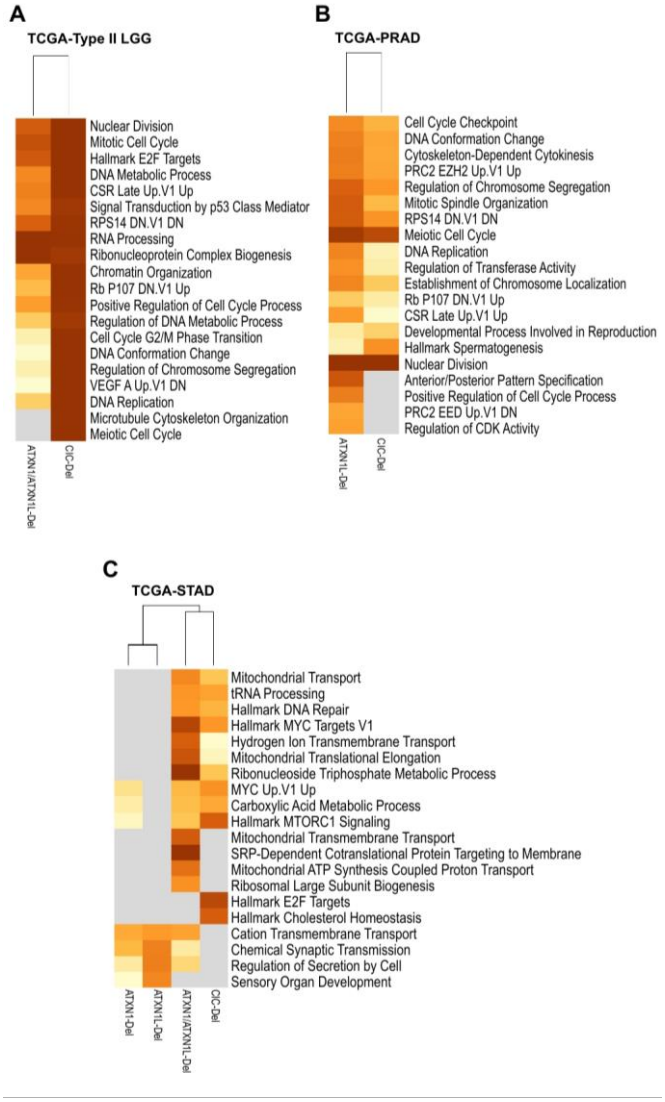

(A) Heat map showing the top 20 enriched terms for upregulated DE genes identified in Type II-LGG$^{ATXN1/ATXN1L\text{-}Del}$ and Type II-LGG$^{CIC\text{-}Del}$. (B) Heat map showing the top 20 enriched terms for upregulated DE genes identified in PRAD$^{ATXN1L\text{-}Del}$ and PRAD$^{CIC\text{-}Del}$. (C) Heat map showing the top 20 enriched terms for upregulated DE genes identified in STAD$^{ATXN1L\text{-}Del}$, STAD$^{ATXN1\text{-}Del}$, STAD$^{ATXN1/ATXN1L\text{-}Del}$ and STAD$^{CIC\text{-}Del}$.
*Gene set enrichment analyses were performed using gene ontology biological processes, hallmark gene sets, and oncogenic signatures.

Supplemental Figure 7 – *ATXN1L*^{KO} cells exhibit decreased CIC-DNA binding

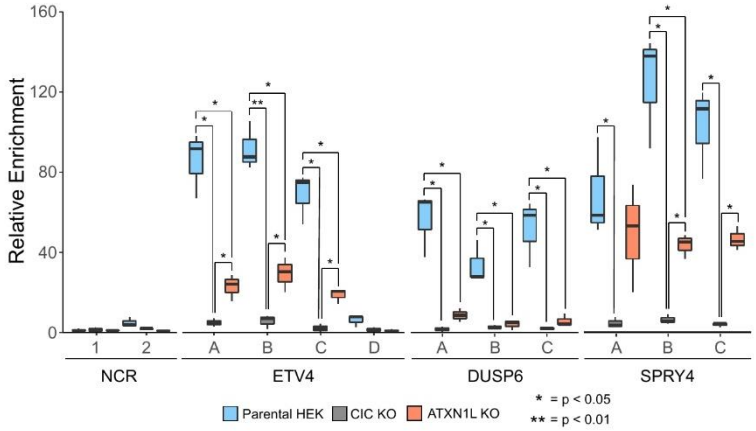

Tukey boxplots showing enrichment of CIC binding to promoter regions of CIC target genes (ETV4, DUSP6, SPRY4) relative to a negative control region (NCR1) following CIC ChIP-qPCR in CICWT (HEK), CICKO (D10) and ATXN1LKO (A30) cell lines. Data were collected over 3 independent experiments and p-values were calculated using the two-tailed independent Student's t-test.

Supplemental Figure 8 – Loss of *ATXN1L* leads to CIC instability

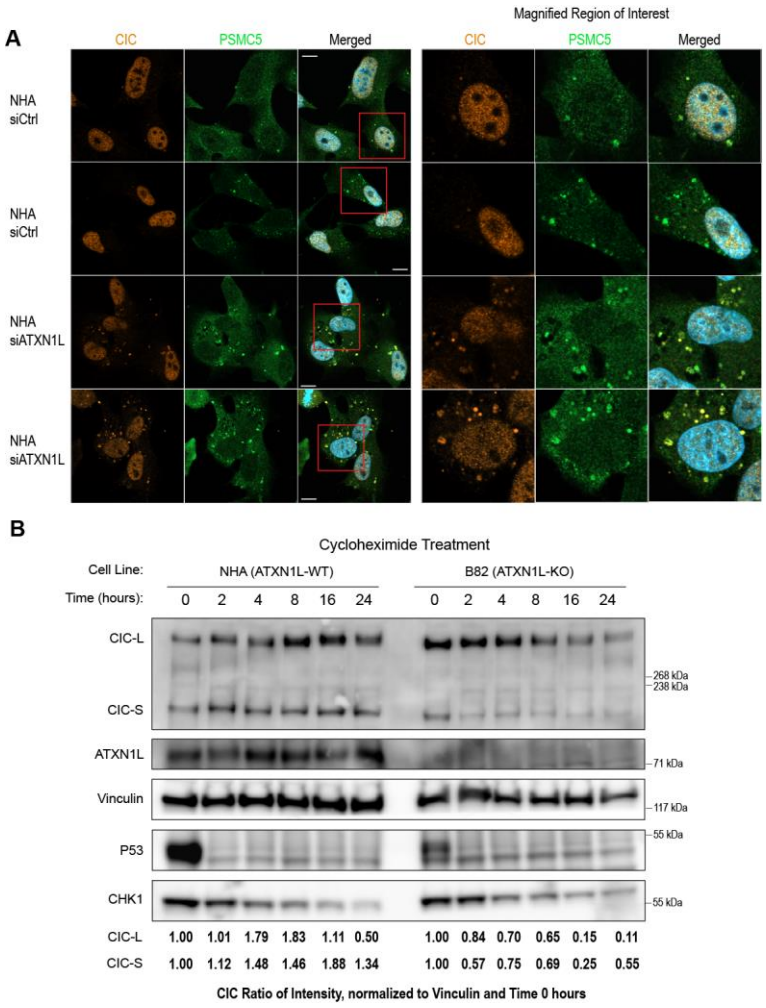

(A) Immunofluorescent visualization of endogenous CIC (orange) and the proteasomal subunit PSMC5 (green) localization following siRNA knockdown of *ATXN1L* in NHA cells. Scrambled siRNA was used as a control and DAPI (blue) was used to stain cell nuclei. White bars seen on the merged image denote 10µm. (B) Representative western blots of *ATXN1L*^{WT} (NHA) and *ATXN1L*^{KO} (B82) cells treated with 100µM of cycloheximide over a 24 hour timecourse showing CIC stability in the presence and absence of ATXN1L. Vinculin was blotted as a loading control and P53 and CHK1 were blotted as protein synthesis inhibition controls.

Supplemental Figure 9 – Loss of ATXN1L leads to CIC ubiquitination and degradation

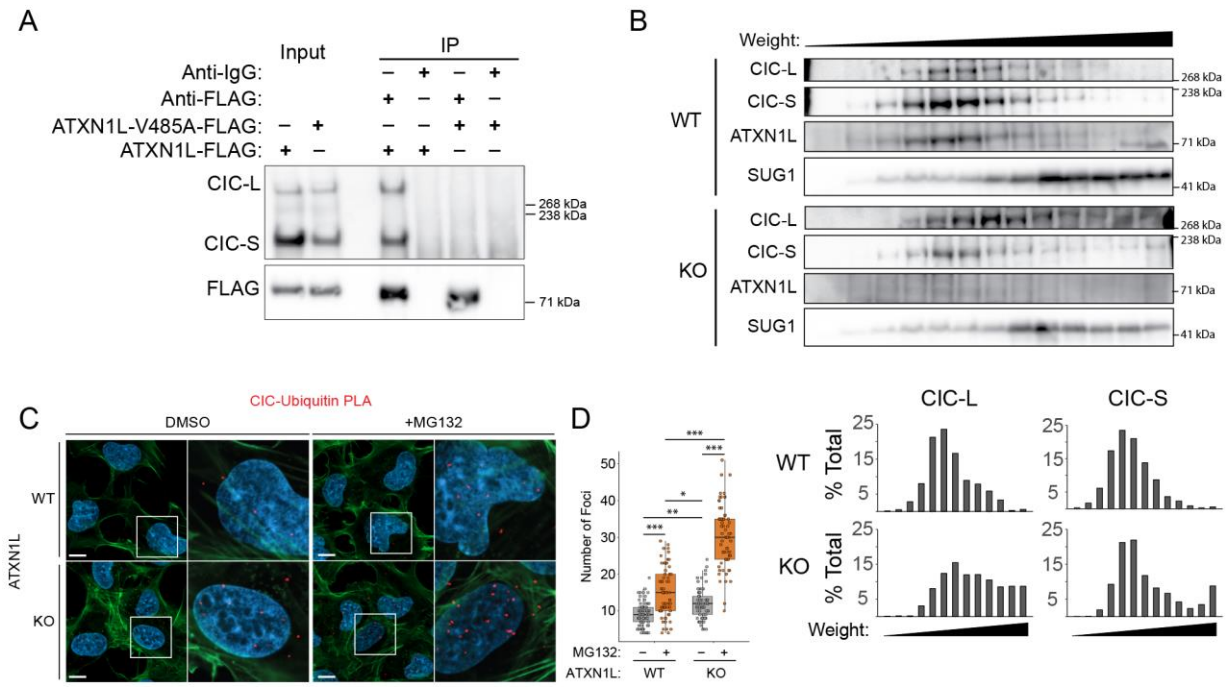

(A) Representative Western blot of FLAG immunoprecipitation of wildtype ATXN1L-FLAG and mutant ATXN1L-V485A-FLAG in HEK cells. (B) Representative Western blot of cellular fractionation across a sucrose gradient of 20-40% showing localization of CIC. SUG1 was used as a proteasome marker. Quantification of CIC protein/fraction are displayed below. Values were normalized to the cumulative total of CIC in all fractions. (C) Immunoflourescence images of proximity ligation assay showing CIC-Ubiquitin interaction in *ATXN1L*^{WT} (NHA) cell lines treated with *ATXN1L* siRNA. Scrambled siRNA used as negative control. White bars denote 10µm. (D) Tukey boxplots showing quantification of number of foci/cell.

Supplemental Figure 10 – in Silico protein analysis of CIC and ATXN1L

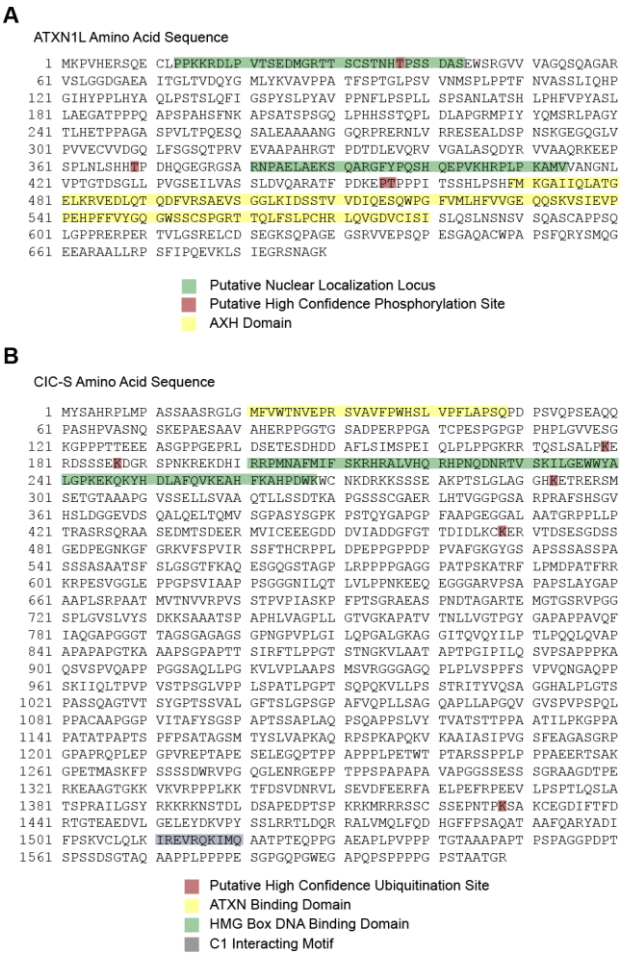

(A) Protein analysis of ATXN1L showing high confidence putative nuclear localization motifs (green) and high confidence putative phosphorylation residues (red). The AXH domain required for CIC interaction is highlighted in yellow.
(B) Protein analysis of CIC-S showing high confidence putative ubiquitination residues (red). The ATXN binding domain required for ATXN1L interaction is highlighted in yellow, the HMG box DNA binding motif is highlighted in green, and the C1 protein interacting motif is highlighted in grey.

Supplemental Figure 11 – Loss of *CIC* leads to ATXN1L dysregulation

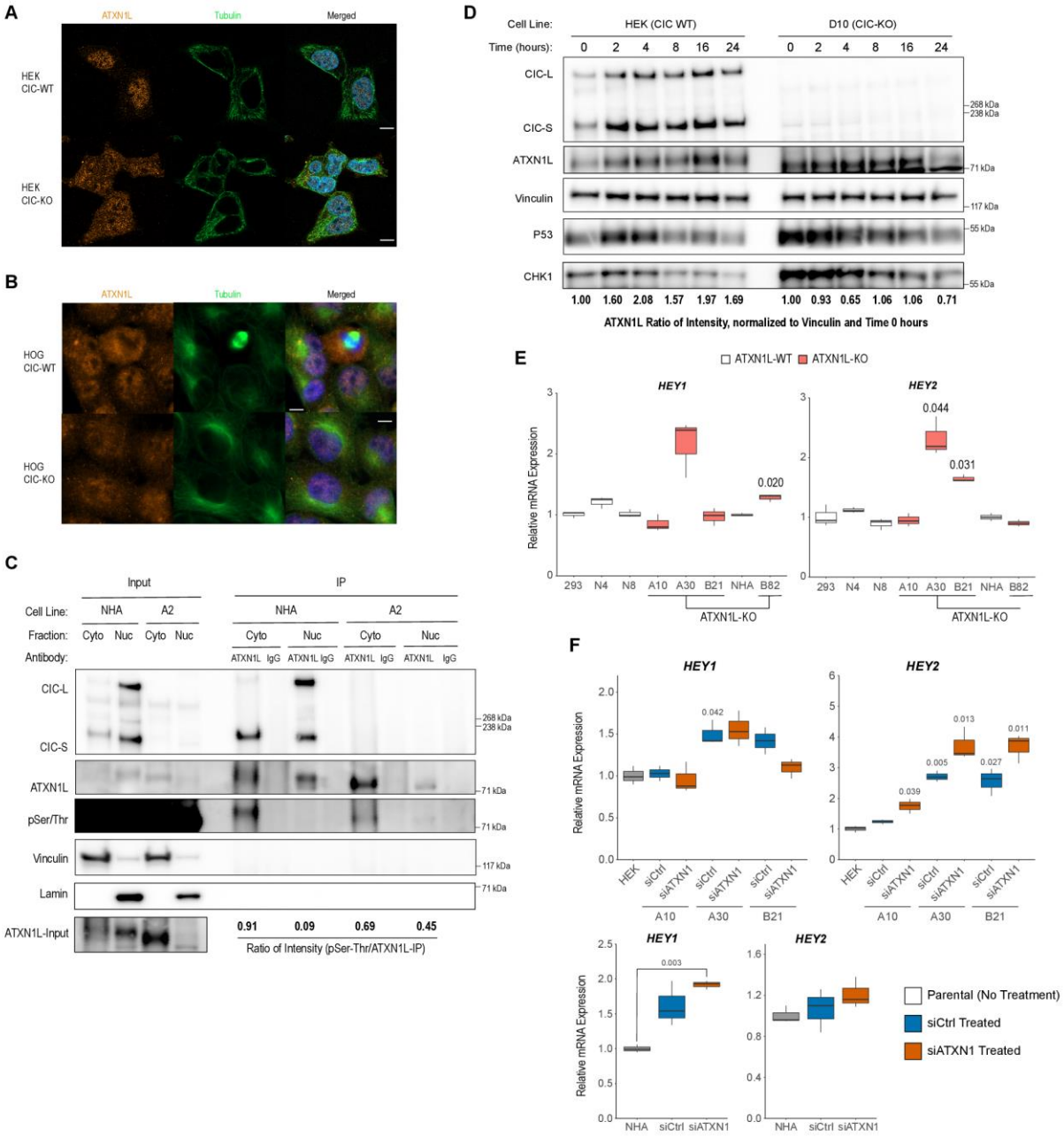

(A) Immunofluorescent imaging of endogenous ATXN1L (orange) in *CIC*^{WT} (HEK) and *CIC*^{KO} (HEK-D10) cell lines showing ATXN1L localization. Tubulin (green) was stained to show cell morphology and nuclei were stained with DAPI (blue). White bars seen on the merged image represent 10µm. (B) Immunofluorescent imaging of endogenous ATXN1L (orange) in *CIC*^{WT} (HOG) and *CIC*^{KO} (HOG-F11) cell lines showing ATXN1L localization. Tubulin (green) was stained to show cell morphology and nuclei were stained with DAPI (blue). White bars seen on the merged image represent 10µm. (C) Western blot of endogenous ATXN1L IP following cellular fractionation (Cytoplasm and Nuclear) of *CIC*^{WT} (NHA) and *CIC*^{KO} (A2) cells. Phosphorylated Serine/Threonine (pSer/Thr) was blotted to show the localization of phosphorylated ATXN1L in the presence or absence of CIC. An IgG IP was performed as a negative control. Vinculin was blotted as a cytoplasmic control and Lamin-B1 was blotted as a nuclear control. (D) Representative Western blot of *CIC*^{WT} (HEK) and *CIC*^{KO} (D10) cells treated with 25µM of cycloheximide over a 24 hour timecourse showing ATXN1L stability in the presence and absence of CIC. Vinculin was blotted as a loading control and P53 and CHK1 were blotted as protein synthesis inhibition controls. (E) Tukey

boxplots showing relative mRNA transcript levels of *HEY1* and *HEY2* in parental HEK and NHA, and *ATXN1L*^{KO} HEK (A10, A30, B21) and NHA (B82) cell lines. Data were collected from 3 independent experiments (passages) and p-values were calculated using the two tailed independent Student's t-test comparing *ATXN1L*^{KO} cell lines to their respective parental cell line. (F) Tukey boxplots showing relative mRNA transcript levels of *HEY1* and *HEY2* in no treatment parental HEK and NHA, and *ATXN1L*^{KO} HEK (A10, A30, B21) and NHA (B82) cell lines treated with either siCtrl (Blue) or siATXN1 (Red). Data were collected from 3 independent experiments and p-values were calculated using the two tailed independent Student's t-test. p-values directly above each boxplot are referenced to the no treatment parental cell line. All other p-values represent t-tests compared to siCtrl.

Supplemental Figure 12 – ERK mediates CIC function

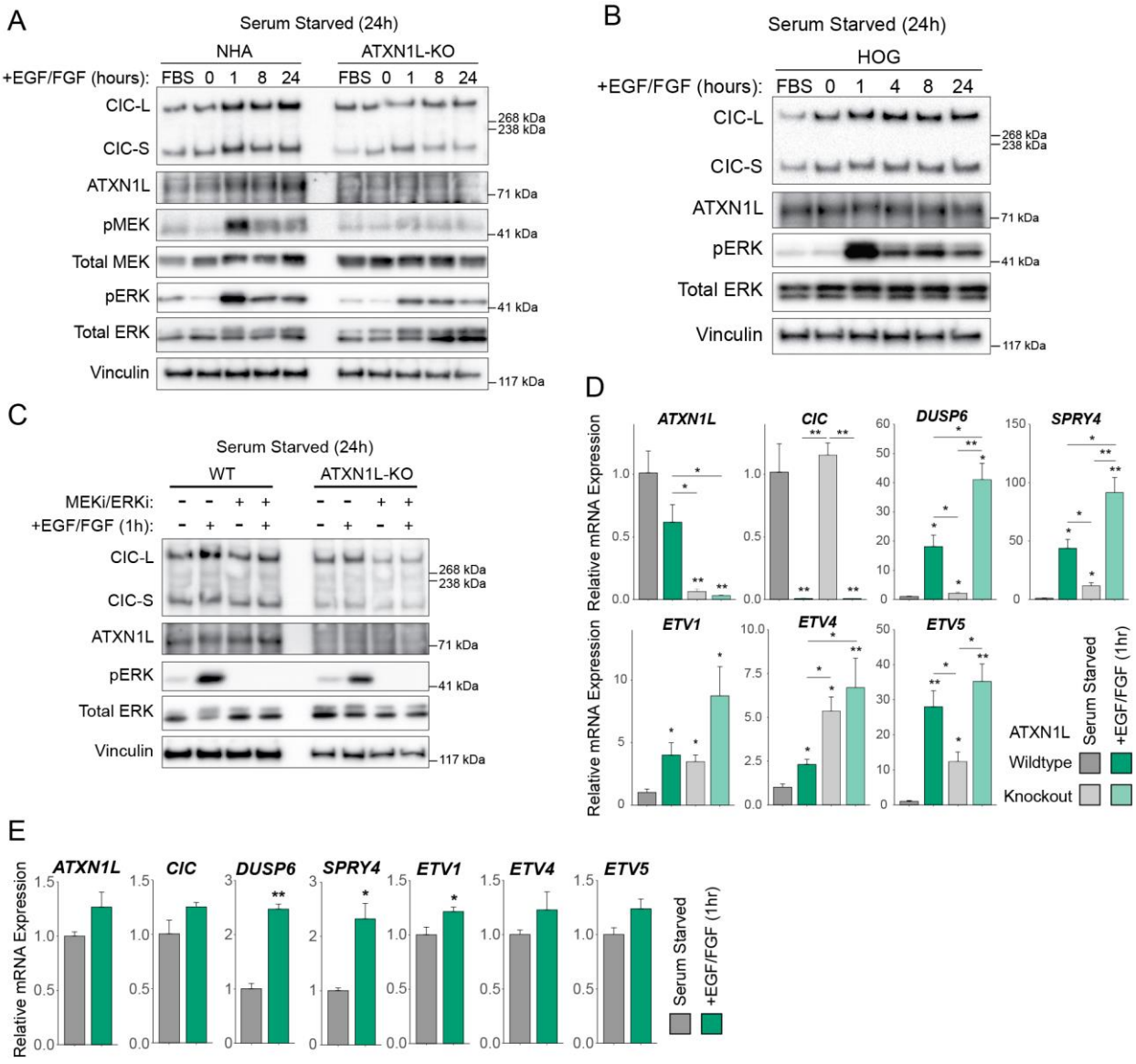

(A) Representative Western blot of *ATXN1L*^{WT} (NHA) and *ATXN1L*^{KO} (B82) cell lines treated with FGF/EGF over 0-24 hours following serum starvation. FBS control was cultured in FBS for the duration of the timecourse. (B) Relative mRNA expression of *ATXN1L*, *CIC*, and CIC target genes *DUSP6*, *SPRY4*, and *ETV1/4/5* in *ATXN1L*^{WT} (HEK) and *ATXN1L*^{KO} (A30) cell lines treated with FGF/EGF for 8 hours following serum starvation. Gene expression was normalized to TBP and serum starved parental *ATXN1L*^{WT} (HEK) cell line was used as a relative

control. (C) Representative Western blot of *ATXN1L*^{WT} (NHA) and *ATXN1L*^{KO} (B82) cell lines treated with FGF/EGF and MEK/ERK inhibitors trametinib/LY3214996. *RT-qPCR quantifications were collected from three independent experiments. Error bars represent one standard deviation. p-values were calculated using the two-tailed independent Student's t-test. Statistically significant values are denoted (* = $p < 0.05$, ** = $p < 0.01$).

Supplemental Figure 13 – EGF/FGF treatment results in increased CIC expression

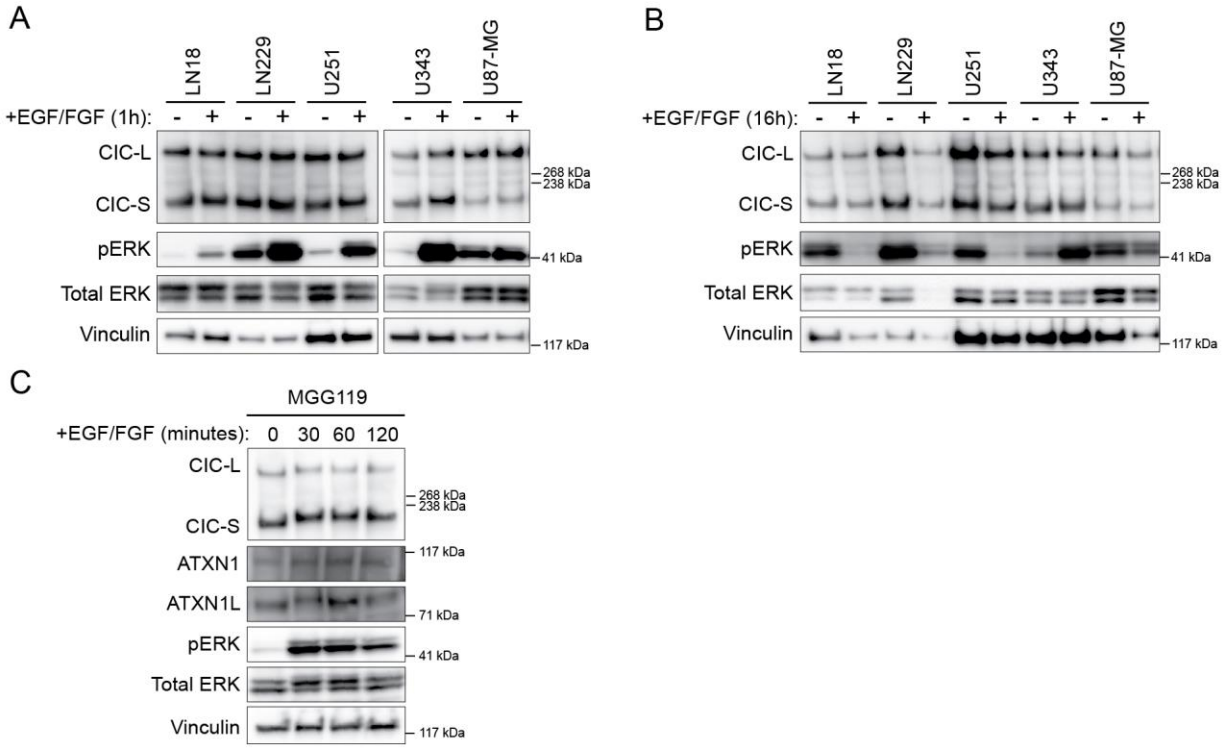

(A) Representative Western blot of GBM cells following serum starvation and EGF/FGF treatment (1 hour). (B) Representative Western blot of GBM cells following serum starvation and EGF/FGF treatment (16 hours). (C) Representative Western blot of BTIC MGG119 following EGF/FGF starvation (16 hours) and EGF/FGF treatment over 120 minutes.

Supplemental Figure 14 – CIC interactors in the absence of ATXN1L

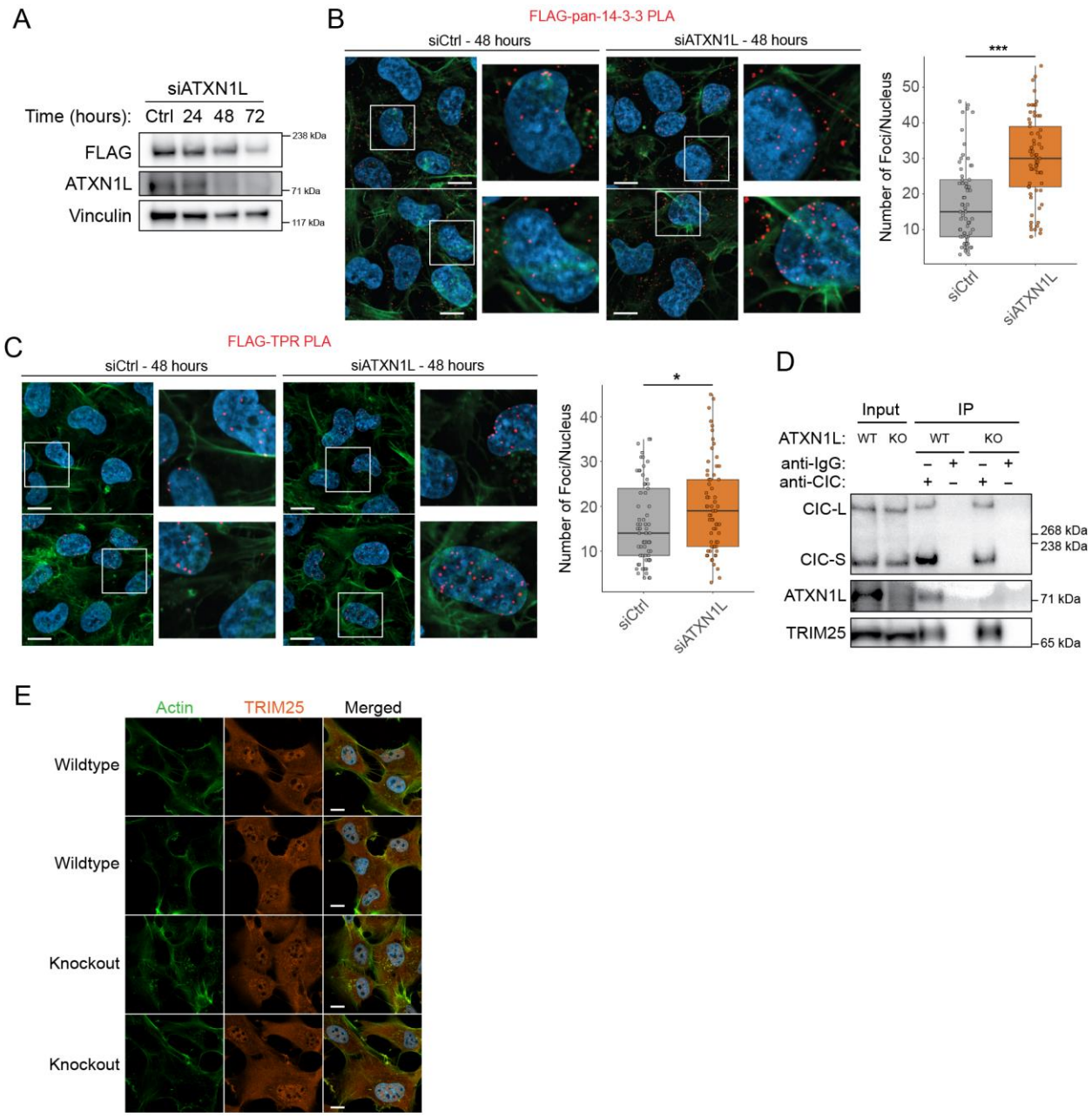

(A) Representative Western blot of *CIC*^{KO} cells with FLAG tagged CIC-S (NHA-S) reintroduced treated with *ATXN1L* siRNA over 72 hours. Scrambled siRNA was used as a negative control. (B) Immunofluorescence images of proximity ligation assay showing CIC-S-FLAG-14-3-3 interaction in NHA-S cells treated with *ATXN1L* siRNA. Scrambled siRNA was used as a negative control. White bars denote 10µm. Right: Tukey boxplots showing quantification of number of foci/cell. (C) Immunofluorescence images of proximity ligation assay showing CIC-S-FLAG-TPR interaction in NHA-S cells treated with *ATXN1L* siRNA. Scrambled siRNA was used as a negative control. White bars denote 10µm. Right: Tukey boxplots showing quantification of number of foci/cell. (D) Representative Western blot of CIC immunoprecipitation showing interaction with TRIM25 in *ATXN1L*^{WT} (HEK) and *ATXN1L*^{KO} (A30) cell lines. (E) Immunofluorescence images showing localization of TRIM25 in NHA cells. White bars denote 10µm. (*) PLA quantifications were collected from 65 individual cells. Error bars represent one standard deviation. p-values were calculated using the two-tailed independent Student's t-test. Statistically significant values are denoted (* = $p < 0.05$, ** = $p < 0.01$, *** = $p < 0.001$).

Supplemental Figure 15 – Characterization of glioma cell lines

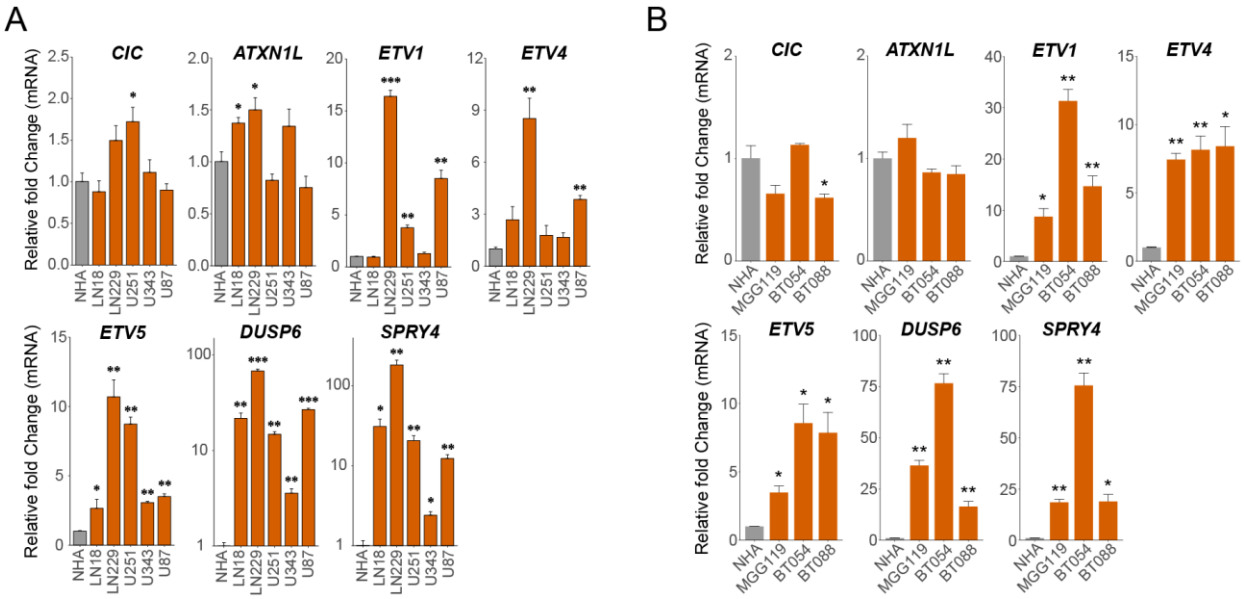

(A) Relative mRNA expression of CIC target genes *ETV1/4/5*, *DUSP6*, and *SPRY4* in GBM cell lines. Expression was normalized to TBP and NHA was used as a relative control.
(B) Relative mRNA expression of CIC target genes *ETV1/4/5*, *DUSP6*, and *SPRY4* in BTIC lines. Expression was normalized to TBP and NHA was used as a relative control.

Supplemental Figure 16 – Validation of CIC-ATXN1L-TRIM25 in glioma cells

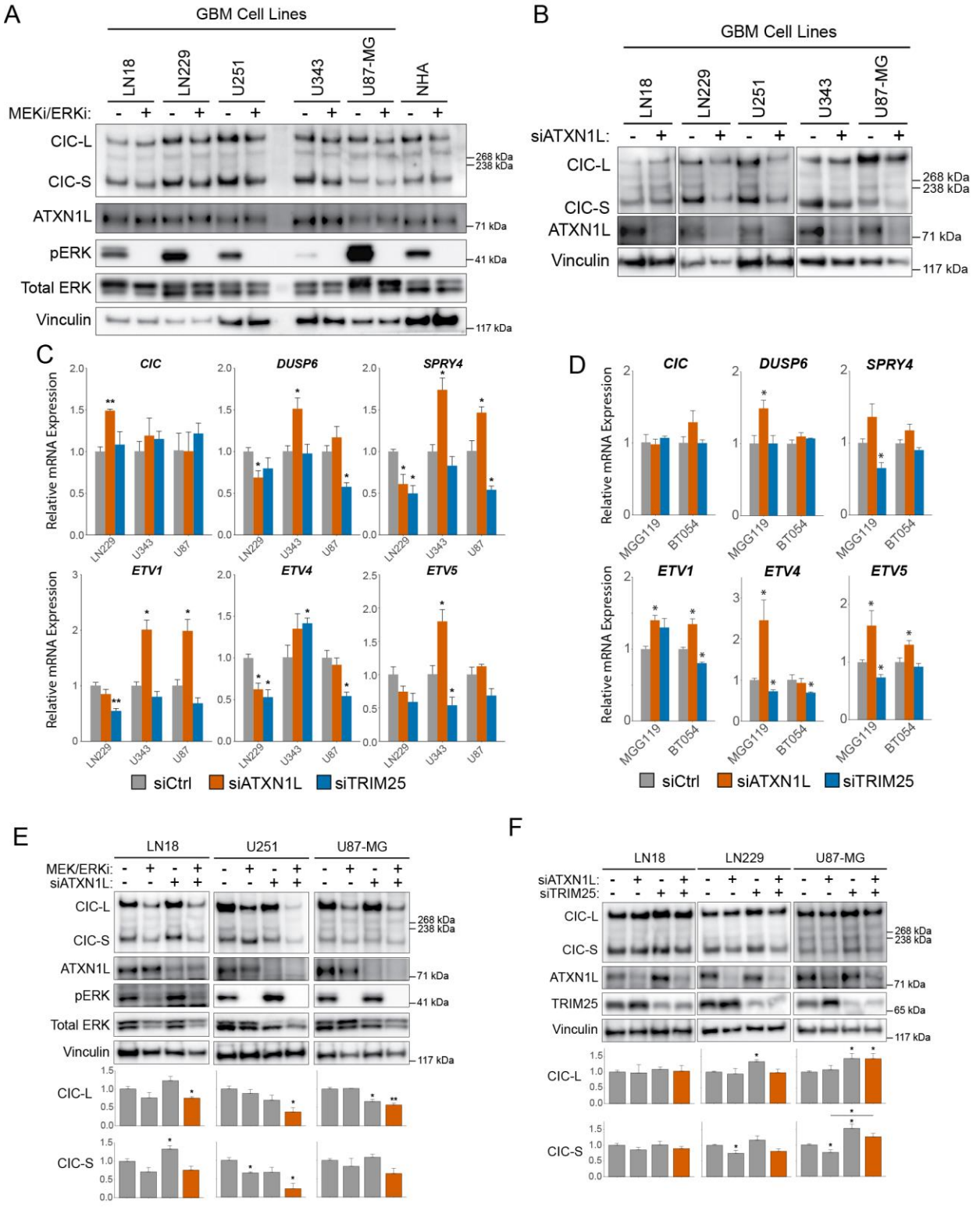

(A) Representative Western blot of GBM cell lines treated with MEK/ERK inhibitors trametinib/LY3214996. DMSO was used as a negative control. (B) Representative Western blot of GBM cell lines treated with *ATXN1L* siRNA for 48 hours. Scrambled siRNA was used as negative control. (C) Relative mRNA expression of *CIC* and CIC target genes *ETV1/4/5*, *DUSP6*, and *SPRY4* in GBM cell lines following siRNA knockdown of *ATXN1L* or

TRIM25 for 48 hours. Expression was normalized to TBP and scrambled siRNA was used as a negative control. (D) Relative mRNA expression of *CIC* and CIC target genes *ETV1/4/5*, *DUSP6*, and *SPRY4* in BTIC cell lines following siRNA knockdown of *ATXN1L* or *TRIM25* for 48 hours. Expression was normalized to TBP and fluorescent RNA was used as a negative control. (E) Representative Western blot of GBM cell lines treated with MEK/ERK inhibitors trametinib/LY3214996 and *ATXN1L* siRNA. DMSO and scrambled siRNA were used as negative control. Below: barplot quantifications of CIC expression. (F) Representative Western blot of GBM cell lines treated with *ATXN1L* and *TRIM25* siRNA. Scrambled siRNA were used as negative control. Below: barplot quantifications of CIC expression. (*) RT-qPCR quantifications were collected from three independent experiments. Error bars represent one standard deviation. p-values were calculated using the two-tailed independent Student's t-test. Statistically significant values are denoted (* = $p < 0.05$, ** = $p < 0.01$).

Supplemental Figure 17 – TRIM25 pathways in cell lines

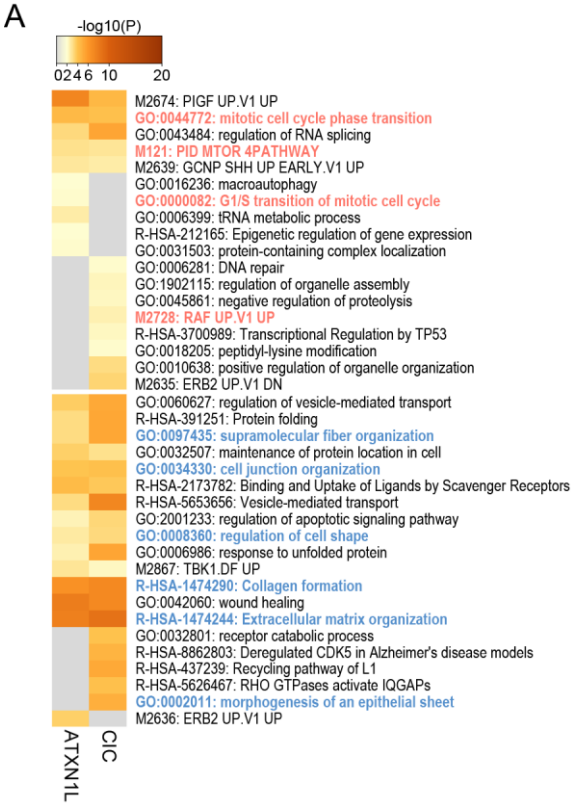

(A) Heatmap showing the top 20 enriched gene sets for directionally discordant differentially expressed genes shared between TRIM25 siRNA in BT549 and MDA-MB-231 breast cancer cell lines and CIC/ATXN1L knockout in NHA cell lines.

Appendix C (Tables are hyperlinked)

Supplemental Table 1 – TCGA samples

TCGA Patient Samples

Supplemental Table 2 – HEK Differential Expression Analysis

HEK *CIC*^{KO} and *ATXN1L*^{KO} DEA

Supplemental Table 3 – NHA Differential Expression Analysis

NHA *CIC*^{KO} and *ATXN1L*^{KO} DEA

Supplemental Table 4 – Type I LGG Differential Expression Analysis

Type I LGG DEA

Supplemental Table 5 – HEK and NHA vs Type I LGG Functional Enrichment

In vitro GSEA

Supplemental Table 6 – Prostate Adenocarcinoma Differential Expression Analysis

PRAD DE Genes

Supplemental Table 7 – Type II LGG Differential Expression Analysis

Type II LGG DE Genes

Supplemental Table 8 – Stomach Adenocarcinoma Differential Expression Analysis

STAD DE Genes

Supplemental Table 9 – TCGA Functional Enrichment

TCGA GSEA

Supplemental Table 10 – TCGA Shared Genes and Functional Enrichment

TCGA Shared GSEA

Supplemental Table 11 – CIC IP-MS results in *ATXN1L*^{KO} NHA

CIC IP MS results

Supplemental Table 12 – TRIM25 knockdown differentially expressed genes

TRIM25 DE Genes

Supplemental Table 13 – Differentially expressed *ATXN1L*^{KO} NHA genes

NHA *ATXN1L*^{KO} DE Genes (RNA-seq)

Supplemental Table 14 – TRIM25 knockdown vs *CIC-ATXN1L* knockout DE genes

TRIM25 knockdown vs CIC-ATXN1L knockout

Supplemental Table 15 – *In vitro TRIM25-CIC-ATXN1L* Functional Enrichment

CIC-ATXN1L-TRIM25 in vitro GSEA

Supplemental Table 16 – TCGA BRCA *TRIM25* Differential Expression Analysis

BRCA DE Genes

Supplemental Table 17 – TCGA BRCA vs LGG/PRAD/STAD Functional Enrichment

TCGA Shared GSEA

Supplemental Table 18 – IDH-WT and IDH-R132H Mutant *CIC*^{KO} Differential Expression Analysis

IDH-WT/Mut CIC DE

Supplemental Table 19 - IDH-WT and IDH-R132H Mutant *ATXN1L*^{KO} Differential Expression Analysis

IDH-WT/Mut ATXN1L DE

Supplemental Table 20 – Shared Differentially Expressed Genes in IDH-WT and IDH-R132H Mutant *CIC*^{KO} and *ATXN1L*^{KO} cell lines

CIC vs ATXN1L shared

Supplemental Table 21 –IDH-R132H mutant *CIC*^{KO} and *ATXN1L*^{KO} Functional Enrichment

CIC vs ATXN1L GSEA

Appendix D

Supplemental Materials 1 – Antibodies

Target	Company	Catalogue #	Western	IF	IP	IHC
Alpha Tubulin	Abcam	ab7291	1:5000	1:500		
ATXN1	NeuroMab	75-122	1:1000			
ATXN1L	ProSci	Custom	1:500	1:100	Yes	
CHK1	Santa Cruz	sc-8408	1:1000			
CIC	Sigma	HPA044341	1:500	1:200	Yes	1:200
CIC	Bethyl Labs	A301-203A			Yes	
DUSP6	Novus	NB100-79998	1:1000			
ETV1	Sigma	SAB5300473-100UL	1:1000			
ETV4	Novus	NBP1-28856	1:1000			
ETV5	Sigma	WH0002119M2	1:1000			
FLAG	Santa Cruz	F3165	1:5000		Yes	
Goat anti-mouse IgG-488	ThermoFisher	A-11029		1:500		
Goat anti-mouse IgG-HRP	Santa Cruz	SC-2005	1:5000			
Goat anti-rabbit IgG-546	ThermoFisher	A-11035		1:500		
Goat anti-rabbit IgG-HRP	Santa Cruz	SC-2004	1:5000			
HDAC1	Abcam	ab7028	1:1000			
IDH1-R132H	Dianova	DIA-H09	1:1000			
Lamin B1	Abcam	ab133741	1:1000			
Mouse IgG	Santa Cruz	sc-2025			Yes	
P53	Santa Cruz	sc-126	1:1000			
Pan 14-3-3	Millipore	AB9748-I		1:100		
Phospho – (Ser/Thr)	Abcam	ab17464	1:1000			
Phospho ERK	Cell Signaling	9101	1:1000			
Phospho MEK	Cell Signaling	9121	1:1000			
PJA1	SantaCruz	Sc-517068	1:1000			
PSMC5 (SUG1)	Invitrogen	MA3-087		1:500		
Rabbit IgG	Cell Signaling	2729			Yes	
SPRY4	Pierce	PA5-31401	1:1000			
Total ERK	Cell Signaling	4695	1:1000			
Total MEK	Cell Signaling	9122	1:1000			
TPR	Abcam	ab84516		1:100		
TRIM25	Abcam	ab167154	1:2000	1:100		
Ubiquitin	Abcam	ab7254	1:1000			
Vinculin	Abcam	ab129002	1:5000			

Supplemental Materials 2 – RT-qPCR Primers

Gene	Forward primer sequence (5’ to 3’)	Reverse primer sequence (5’ to 3’)
CIC	GCGTCTCCAAATGACACA	CCGACTTCTTGTCCGAATAC
ATXN1L	TGACCAGCGAGGATATGG	GGACCATTCAGAAGCAC
ATXN1	CGTGGCCGTGATACAGTTCG	GGAACACGGCAAATCAAAGAGC
DUSP6	CCAGTGGAGATCTTGCCCTTC	TGTACTTGATGCCGAATTCCTCC
ETV1	ACTGCTGAAGACAGACATGGAAC	CATGTAGGCCATGCTCTCATCAA
ETV4	AGGCGGAGGTTGAAGAAAGG	GGGCAGAAGAAAGGCAAAGG
ETV5	AGGGAAATCTCGATCTGAGGAATG	GCTAACCAAGCCTCTTGAAGTTGA
SPRY4	CAACGGCTCTTAGACCACATGG	GATGCACACTCCTTGCATTTACAC
HEY1	CCTCCGCCTCCAAACTGT	TATAGGGCTTGCCAAGGTTTGC
HEY2	GCGTCGGGATCGGATAAATAAC	CTGTTAGGCACTCTCGGAATCC
SPRED1	GTCAGGATGCTCCAGACCCT	CTCCCTCTGAGTCTGACATACAATGA
SPRED2	CTCATCCATGGTGAACGACAGAA	GTCAAAGGCTCGGGCATC
PTPN9	TGGTACTTCAGGCTCTGTTTTACTTG	CCCTTCAGCAGGTTTAGGACTTTC

Supplemental Materials 3 – siRNA sequences

Target	Company	siRNA ID#/Catalogue#	siRNA Sequence
ATXN1L	Life Technologies	s230554	CGAGAGCGAAAUUUAGUAAtt
ATXN1L	Life Technologies	s230553	CCAUCUGUGGUGAAUAUGAtt
ATXN1L	Life Technologies	ATXN1LHSS155872	GCCUUCCCUAUGCUGUGCCACCUAA
ATXN1	Life Technologies	n294053	AUAAGCAGAUACAAAAAAtt
ATXN1	Life Technologies	ATXN1HSS109491	UUUGGAACACGGCAAAUCAAAGAGC
TRIM25	Life Technologies	118751	CCUCGACAAGGAAGAUAAAtt
TRIM25	Life Technologies	s15204	CCAUAGACCUCAAAACGAtt
TRIM25	Life Technologies	s15205	CAACACCGCCCACAACAAAtt

Supplemental Materials 4 – CRISPR derived Cell Lines and Genetic Backgrounds

Name	Parental	*CIC*	*ATXN1L*	*IDH1*
HEK	-	-	-	-
D10	HEK	KO	-	-
A10	HEK	-	KO	-
A30	HEK	-	KO	-
B21	HEK	-	KO	-
HOG	-	-	-	-
F11	HOG	KO	-	-
NHA	-	-	-	WT OE
A2	NHA	KO	-	WT OE
H9	NHA	KO	-	WT OE
B82	NHA	-	KO	WT OE
B16	NHA	-	KO	WT OE
B21	NHA	-	KO	WT OE

F8	NHA	-	-	R132H
C5	F8	KO	-	R132H
E10	F8	KO	-	R132H
B18	F8	-	KO	R132H
C22	F8	-	KO	R132H
A2-WT	A2	CIC-S OE	-	-

Supplemental Materials 5 – Other Cell Lines

Name	Tissue Derived
U87-MG	Glioblastoma
U251	Glioblastoma
U343	Glioblastoma
LN18	Glioblastoma
LN229	Glioblastoma
MGG119	Glioblastoma
BT054	Oligodendroglioma
BT088	Oligodendroglioma

Supplemental Materials 6 – ChIP-PCR Primers

Gene	Forward primer sequence (5' to 3')	Reverse primer sequence (5' to 3')
NCR1	TGGTCTCCATGACAACGAAGAAGAG	GTCCCATCCTACTGAAGTGCCC
NCR2	TGGGAATGGTCGCAGAGGTT	GGTCTCATCGGTGAACCCCC
ETV4 Site A	GCGGGGGCCAATCAGAATGTA	AACTCCAGCCGCGAGTTTTA
ETV4 Site B	GCTTCATTCAGTGCTCCGGCT	CGTGGCGAGACGGTGAAGA
ETV4 Site C	CGGGAGGGTGGGCTCATTCA	ATGCCCTTGAACTCCTGCCC
ETV4 Site D	AGAACTAGCAAGAACCATGAGCCT	TGTGTCTGGTCCCTATCCCCAC
DUSP6 Site A	TCTTGGACTCAGCCTCGCAC	TTCCGCAGCACGCTCATTGG
DUSP6 Site B	CGAGGCAGCTCCTCAATGGAT	CTCATTGGCTGGCCCGGAGA
DUSP6 Site C	CCGGCTGGAACAGGTTGTGTT	GGGCTTATCCGGAGCGGAAAT
SPRY4 Site A	GCTGTCAGCTCAGCTCGCTA	CGCGCTCAGGGTCTGTTGT
SPRY4 Site B	CGTGCCGTTCGCGATTCTAT	GCCAGTCCCAGCAATCACG
SPRY4 Site C	GGCACAACAGACCCTGAGCG	AGCCAGTCCCAGCAATCACG